Università degli Studi di Roma
"Tor Vergata"

Facoltà di Scienze Matematiche, Fisiche e Naturali

The GEM detectors for the innermost region of the forward muon station of the LHCb experiment

Dottorato di Ricerca in Fisica - XX Ciclo

Matteo Alfonsi

Tutor
Dott. G. Bencivenni

Coordinator
Prof. P. Picozza

Contents

Abstract

The LHCb experiment will take place at the LHC accelerator at CERN and will start in 2008. It is dedicated to precision measurements of $\mathcal{CP}$ violation and rare decays in the b quark sector.
The apparatus is a single arm spectrometer and it is designed with a robust and flexible trigger in order to extensively gain access to a wide spread of different physical processes involving *beauty* particles. This will allow to over-constrain the Standard Model predictions about $\mathcal{CP}$ violation, and to discover any possible inconsistency, which would reveal the presence of "New Physics" beyond the Standard Model.

This thesis reports the work performed on two aspects of the LHCb experiment: the main contribution is the development and the construction of a detector based on Gas Electron Multiplier (GEM) technology for the instrumentation of the high irradiated region around the beam pipe of the forward Muon Station; in the second part the possibility of the search of the rare $D^0 \rightarrow \mu^+\mu^-$ decay at the LHCb experiment is investigated, demonstrating that the experiment can found application also in the charm sector physics.

The triple-GEM detectors equipping the inner region (R1) of the first muon station (M1) of the LHCb experiment was proposed, developed and realized by our group at the Laboratori Nazionali di Frascati (LNF) of Istituto Nazionale di Fisica Nucleare (INFN) in collaboration with the INFN section of Cagliari (Ca-INFN).
The main task of such a detector is the muon p_T measurement for the LHCb trigger, which requires high time performance. The use of a triple-GEM detector as a triggering device is certainly a novelty in the field of high energy physics. The first application of GEM detectors was in the COMPASS experiment, where they are currently used as a trackers, while a little interest was devoted so far to the optimization of the time response of GEM detectors. In the

Abstract

LHCb trigger logic a critical issue is the high efficiency in the bunch-crossing identification, so a high detector time resolution is the main constraint.
Since the time resolution of a triple-GEM detector operated with an Ar/CO_2 (70/30) gas mixture is about 10 ns (r.m.s.), an intense R&D activity on GEM detectors was required. The use of fast CF_4 and isobutane based gas mixtures, together with an optimization of the geometry and the electric fields of the detector, has allowed to improve the time resolution of the single detector down to 5 ns (r.m.s.), largely fulfilling the requirements of the experiment ($\sigma_t \leq 3$ ns is achieved by two logically OR-ed detector layers, as required in the LHCb muon stations).
The final design of the detector has taken into account the tight space constraints around the beam pipe. We defined detailed construction procedures as well as severe quality controls for the production of 12 fully instrumented detectors required to cover the ~ 1 m^2 area of M1R1, plus 6 additional spare detectors.
The performance of one of such detectors, fully integrated with front-end electronics and all the other components, has been measured in a recent test at the SPS beam at CERN, where the LHCb running condition has been simulated by means of a similar bunch crossing time structure and the adoption of the official LHCb DAQ chain. The results largely fulfilled the experiment requirements and gave us useful informations for the future commissioning phase.
In addition we have demonstrated that the detector is robust from the point of view of discharges as well as ageing processes, and can tolerate the radiation dose foreseen in 10 years of operation in the region M1R1 of the LHCb experiment.
All the detectors are now at CERN, ready for the installation on the M1 station, foreseen for the first months of 2008.

The charm production at the LHCb experiment is even greater than the beauty production, thanks to the about seven times higher expected cross section (3.5 mb) with respect to the *beauty* cross section (0.5 mb). Recent works demonstrated some interest for rare decays in the charm sector, that can gives complementary information with respect to the K or B–mesons physics and constrain the parameters of several extension of the Standard Model.
In this framework, the results of a preliminary study of the rare $D^0 \to \mu^+\mu^-$ decay at LHCb experiment is presented in the second part of the thesis. Using the simulation and the analysis software realized for the experiment, a selection algorithm has been written, obtaining a first

estimation of the upper limit on the branching ratio achievable at LHCb that is about two order of magnitude lower than the current one.

Abstract

Chapter 1

The LHCb experiment in the actual physics scenario

LHCb [1] is the experiment at the Large Hadron Collider [2] dedicated to physics studies in the *B*-mesons system.
Although the Standard Model well describes the observed *CP-violation* processes in particle physics with the Cabibbo-Kobayashi-Maskawa mechanism, contributions from new physics beyond the Standard Model can change the expectations of *CP-violation* phases and rare decay branching fractions; cosmological problems such as the dominance of matter with respect to antimatter in the universe are still open and the level of *CP-violation* that can be generated by the Standard Model weak interaction is not enough to explain that.
LHCb has been designed for high precision measurements of *CP-violation* phenomena that will extend the results obtained at the B factories and Tevatron, over-constraining the unitary triangle. Moreover the search of rare or even Standard Model forbidden decays can address the physics community in the definition of New Physics models.
In this chapter, after an introductory section on the Large Hadron Collider project, the LHCb experiment will be described in its general layout, detectors, physics programme and expected performance.

1.1 The LHC project

The installation of the Large Hadron Collider (LHC) at CERN has been completed and the first proton-proton collisions will take place in 2008. The collider will gradually reach the center of mass energy of 14 TeV and the design luminosity of 10^{34} cm^{-2}s^{-1}, allowing to probe the TeV-scale physics with a high statistics of events.
The project benefits from the existing LEP infrastructure, namely the 27 km long circular underground tunnel and its versatile and well-know accelerator injection complex.
The proton beams are accelerated in a linear accelerator (Linac) up to 50 MeV. Then two circular accelerators boost them to 1.4 GeV, in the Proton Synchrotron Booster (PSB), and to 25 GeV, in the Proton Synchrotron (PS), before entering in the Super Proton Synchrotron (SPS). There they reach the energy of 450 GeV and enter the LHC through two tunnels (Fig. 1.1). The main design parameters of the LHC machine is reported in Tab. 1.1 [2].

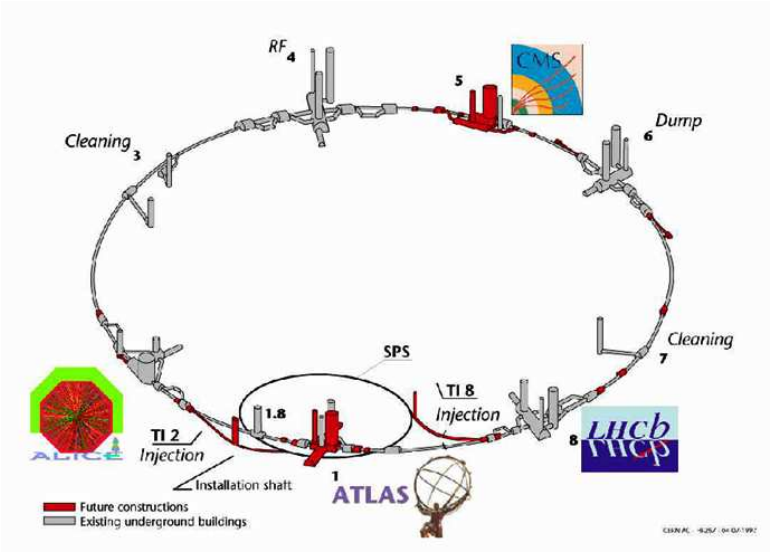

Figure 1.1: The LHC complex.

The basic layout of the machine is similar to the LEP, with eight straight sections approximately 538 m long, available for experimental insertions or utilities. Four of these sections have the beam crossing from one ring to the other and are therefore dedicated to experimental sites, with two of them also hosting the injection system. Two insertions contain collimation systems using only classical robust magnets (betatron and momentum cleaning). One inser-

Machine circumference	26659 m
Beam energy	7 TeV
Luminosity	10^{34} cm^{-2}s^{-1}
Luminosity lifetime	10 h
Number of bunches	2835
Particle per bunch	10^{11}
Bunch spacing	25 ns
Energy loss per turn	6.7 keV
Crossing angle	300 μrad
r.m.s. IP beam radius	16 μm
r.m.s. IP beam length	5.3 cm
Dipole field	8.4 T

Table 1.1: The LHC machine parameters [2].

tion contain the RF system and the last straight section contain the beam dump insertion to remove the beam safely from the collider at the end of a physics run, when the luminosity has degraded.

The choice for a proton accelerator was driven by the fact that the losses by synchrotron radiation for electrons of the same energy are prohibitive, as illustrated by LEP run II. Indeed, the beam energy was forced to the limit of $\simeq$ 104 GeV (intermittent) despite of a full use of superconducting technology. The huge RF power was then consumed just to compensate for the losses.

Two identical proton beams have been chosen to satisfy the high luminosity requirement. An antiproton beam as Tevatron collider would have simplified the technical conception but the low efficiency in antiproton production wouldn't allow to achieve the required luminosity.

As a consequence and in order to manage with the room in the existing tunnel, the magnet configuration is unusual as shown in Fig. 1.2. Two coil assemblies, surrounding the two beam pipes, are enclosed in the same iron yoke and cryostat. Given the radius of curvature of the orbit, the required huge operation field of 8.4 Tesla can only be obtained at acceptable cost by cooling the magnets to 1.9 Kelvin. There will be about 1200 of such 14 m long dipole magnets in the main arcs (Fig. 1.3).

The synchrotron energy loss per turn amounts to 6.7 keV is negligible in terms of RF power load, but the emitted power of 3.7 kW has to be absorbed by the beam pipe, that works at

cryogenic temperature, thus affecting the power required by the refrigeration system. An additional issue is the release of absorbed gas molecules, when the synchrotron light impinges on the beam pipe (hard UV photons), which increases the residual gas pressure. This shows how has been demanding the design of this new machine.

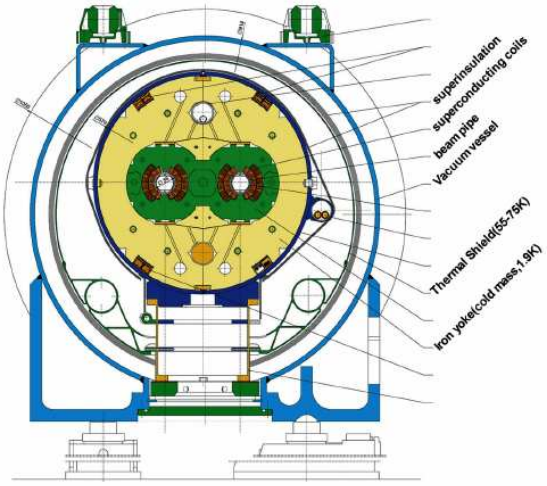

Figure 1.2: Cross section of a LHC dipole magnet. The inner coil keeps the two separated beams in orbit by using a 8.4 TeV T field. The coil is encapsulated in a cryogenic system, keeping the magnet at temperature of 1.9 K.

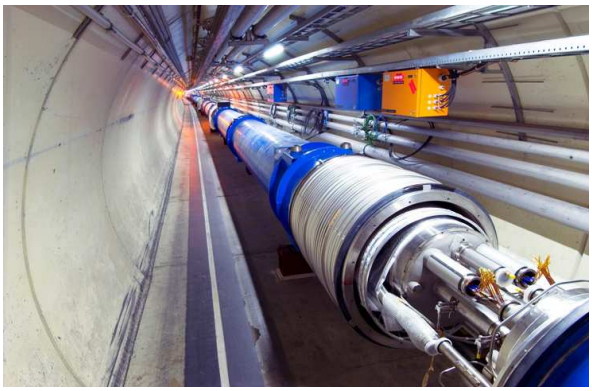

Figure 1.3: Picture of the LHC dipole magnet during the machine assembly.

Five experiments will make use of LHC. The ATLAS and CMS experiments located in new caverns built at IP1 and IP5 are multi-purpose central detectors. Their main (but not unique task) is to find the Higgs boson, using the full LHC potential by running at the very high design luminosity $\mathcal{L} = 10^{34}$ cm^{-2}s^{-1}. The ALICE experiment at IP2 will study the quark-gluon plasma in dedicated runs for heavy ions (*Pb-Pb*) collisions. TOTEM is a very small detector studying very forward QCD processes at IP5. It will measure the total cross section at LHC, which is very important for the other experiments, for instance to measure absolute luminosity. Finally, the LHCb experiment in IP8, dedicated to *b-quark* physics, will be described in detail in the next sections.

1.2 The proton-proton interaction setup at LHCb

Since its startup LHC will be a high-rate charm, beauty and top quark factory, as shown in Tab. 1.2. Cross sections are extrapolated from UA1, CDF and D0 [3] data, but they are affected by large uncertainties.

Total	σ_{tot} = 100 mb
Inelastic	σ_{in} = 80 mb
$c\overline{c}$	$\sigma_{c\overline{c}}$ = 3.5 mb
$b\overline{b}$	$\sigma_{b\overline{b}}$ = 500 μb
$t\overline{t}$	$\sigma_{t\overline{t}}$ = 0.8 nb

Table 1.2: Cross sections at LHC.

The total inelastic cross section defines the average number of inelastic pp-interactions per bunch crossing:

$$< N_{pp} >= \frac{\mathcal{L} \cdot \sigma_{in}}{f_{LHC} \cdot f_{ne}}$$

where $\mathcal{L}$ is the integrated luminosity, f_{LHC} is the 40 MHz bunch crossing frequency of the LHC machine and f_{ne} = 0.744 is the fraction of non-empty bunches crossing [1].
This number is $\sim$ 23 at the maximal LHC luminosity ($\mathcal{L}$ = 10^{34} cm^{-2}s^{-1}), but LHCb plans to operate at a lower average luminosity of 2×10^{32} cm^{-2}s^{-1}, in order to obtain $\sim$ 0.37 average interactions per bunch-crossing (Fig. 1.4). The advantages of this precise strategy are events dominated by single pp-interactions easy to analyse and a reduced radiation damage of the detectors. Moreover this luminosity should be achieved since the first physics run of LHC operation and can be kept constant while the luminosity at the other interaction points will be progressively increased to their design values, allowing the experiment to collect data under constant conditions.
The $\sigma_{b\overline{b}}$ cross-section at 14 TeV is extrapolated to be in the range 175 – 950 μb, depending on the value of badly known parameters. It will be known more precisely after the start of LHC, and the value of 500 μb is a mean assumed as reference by all LHC experiments. The dominant $b\overline{b}$ production mechanism in pp collisions is the fusion of two or more gluons radiated from the constituent quarks of the protons. This leads to an approximately flat distribution in rapidity and hence an angular distribution peaked at low polar angles. The directions of

[1] Empty bunches arise due to a no-integer ratio of the PS, SPS and LHC revolution frequency.

the two b hadrons are very correlated as shown in Fig. 1.5. The two peaks correspond to $b\bar{b}$ pair flying together in the same direction of the beam axis. Thus for a dedicated b-physics experiment the coverage of low polar angles is one of the primary task.

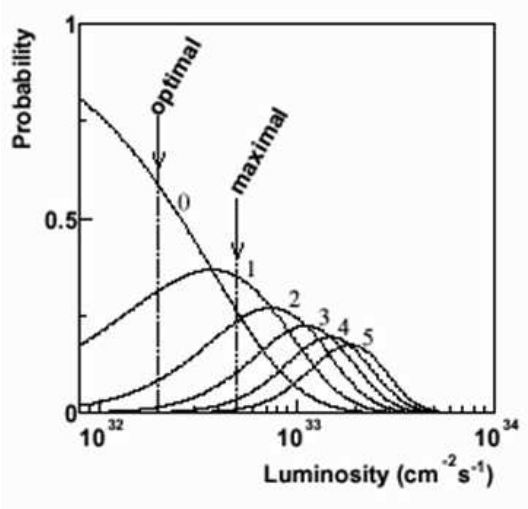

Figure 1.4: Probability distribution of the number of interaction per bunch crossing as a function of the luminosity.

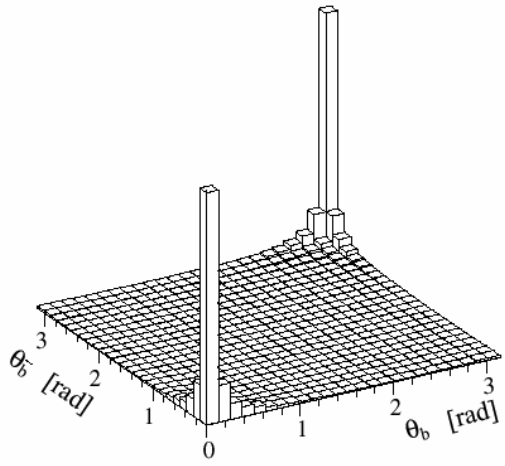

Figure 1.5: Polar angle θ of b and $\bar{b}$ hadron directions.

1.3 The LHCb apparatus

The LHCb detector [1], [4] is a single-arm spectrometer. Its similarity with a fixed target experiment (e.g. HERA-B) is explained by the very forward peaked b-quark distribution at LHC, as discussed in previous section.
Its main features are:

- a precise particle identification to access a wide range of multi-particle final states;
- a high resolution vertex detector to identify secondary vertices and to precisely measure the proper-time;
- a fast and versatile trigger system to select the interesting events among the huge number of *minimum bias* events ($\sigma_{b\overline{b}}/\sigma_{in}$ = 0.6%).

It will be located at IP8 in the pit that housed the Delphi experiment during the LEP era. To avoid any civil engineering the detector had to fit in the pre-existent cavern, which constraints the total length of the detector to 20 m and require for a displacement of the interaction point by 11 m.
The geometrical acceptance of the detector, as defined by the dimensions of the magnet, is 300 mrad in the horizontal plane (*bending plane*) and 250 mrad in the vertical plane.
With this acceptance and the expected performance, the LHCb could detect the decay of both b hadron for about 20% of the whole $b\overline{b}$ events produced in 4π. The B-hadrons have an average momentum of 80 GeV/c, which corresponds to a mean decay length of about 7 mm, and are characterized by a decay vertex separated from the primary vertex, resulting in higher impact parameters of the decay products tracks.

The experimental apparatus is shown in Fig. 1.6 and consists of five main sub-detectors:

- the vertex system;
- the tracking system;
- the ring cherenkov detectors;
- the electromagnetic and hadronic calorimeters;
- the muon system.

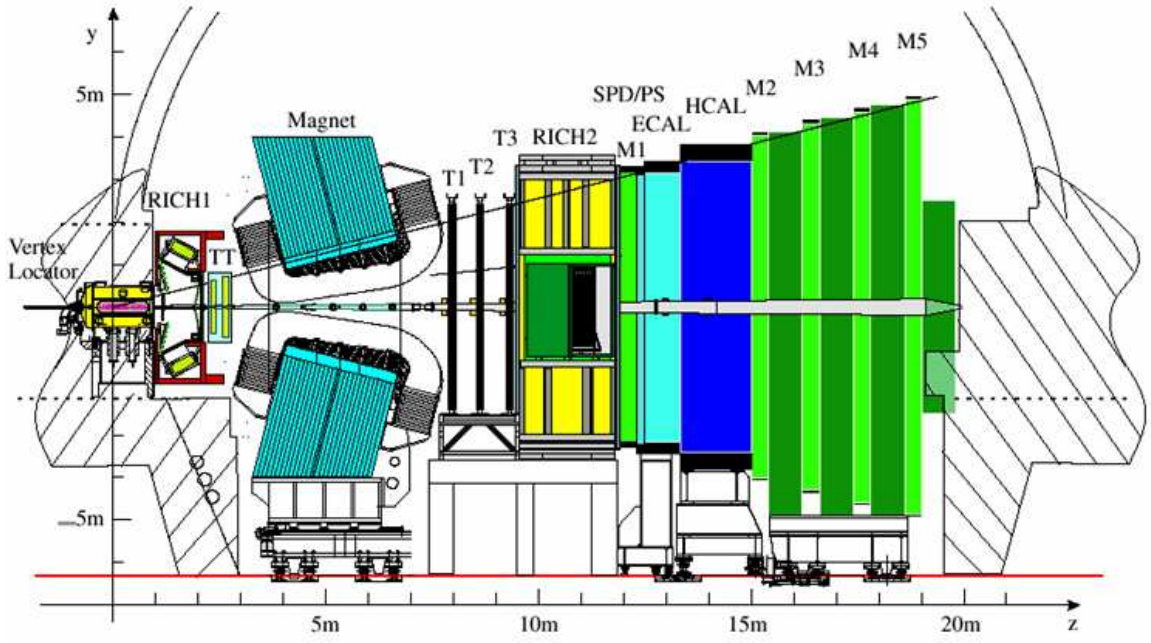

Figure 1.6: Cross section of the LHCb spectrometer.

1.3.1 The vertex detector system

The Vertex Locator (VELO) [5] provides precise informations about charged particles close to the interaction point. Its fine segmentation allows for a precise primary vertex reconstruction and search for separated secondary vertices.

The detector is composed of 21 disk-shaped 300 μm silicon sensors, divided in two halves, with a $r - \phi$ segmentation geometry, and distributed over 1 m along the beam axis around the interaction point. They will be mounted perpendicular to that axis on Roman pots inside a vacuum tank and will be retracted from the beams during injection (Fig. 1.7).

As it surrounds the interaction region it also allows some knowledge about the backward side of the event, which helps disentangling multiple primary vertices. Two additional stations, only r-segmented, in the backward region act as veto for multiple pp-interaction events (*pile-up veto*).

The position resolution on the primary vertex is 40 μm in z and 8 μm in x and y. For secondary vertices it varies from 150 to 300 μm (in z) depending on the number of tracks. This corresponds to less than 40 fs resolution on the B proper time of flight.

The VELO is used in the High Level Trigger which enriches the B event content by finding

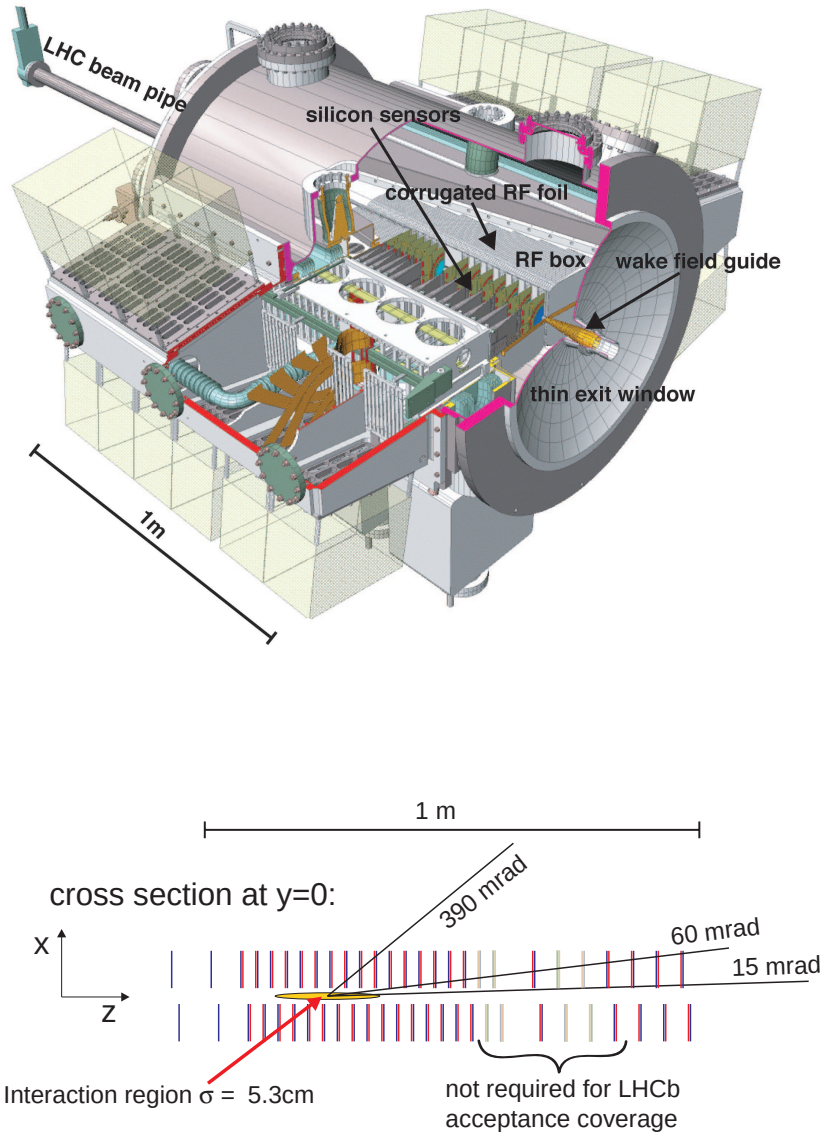

Figure 1.7: Up: The VELO vacuum vessel with the silicon sensor, RF box, and wakefield guides and exit window; Bottom: The station set-up. Grayed layers have been removed after the reoptimization of the detector [4]

high impact parameter tracks and secondary vertices.

1.3.2 The RICH detectors

The two Ring-Imaging Cherenkov detectors [6] have the main task of an efficient separation of kaons from pions over the full momentum range accessible from LHCb.
For the K-π separation the benchmark is the distinction between the $B \to K\pi$, $B \to \pi\pi$ and $B \to KK$ channels. The RICH achieves a K-π separation above 3σ for tracks in the range 1-150 GeV/c with an efficiency of $\sim$ 90%. It also crucial to tag the flavor of the reconstructed B hadron using the kaon from the $b \to c \to s$ decay chain of the other b-hadron.
The RICHs detect the ring images formed by Cherenkov photons around the particle traversing the detector. The photons are detected by cylindrical pixelated Hybrid photodiode (HPD) tubes. These detectors are sensitive to magnetic fields, which impose that RICH detectors must be designed studying the fringe field of the magnet and a shielding solution of the HPD. Because of this requirement and the request to cover a wide momentum range, a system consisting of two Ring Imaging Cherenkov has been designed.
The first RICH (RICH-1) is placed upstream the magnet and uses the silica aerogel (refractive index *n*=1.03) and C_4F_{10} (*n*=1.0014) as radiators. It is designed for low momentum (1-70 GeV/c) and high angle (30-300 mrad) tracks. A great effort has been done during the LHCb re-optimization [4] to obtain a compromise between a magnetic field slightly involving also the region between VELO and TT stations and the shielding of RICH-1 photon detectors.
The second RICH (RICH-2) is located downstream the magnet and the T1-T3 trackers, and uses only the CF_4 (*n*=1.0005) as radiator. The RICH-2 covers high momentum (12-150 GeV/c) and low angle (15-120 mrad) tracks.
Fig. 1.8 shows the Cherenkov angle as a function of particle momentum for the radiators adopted in the the RICH system.

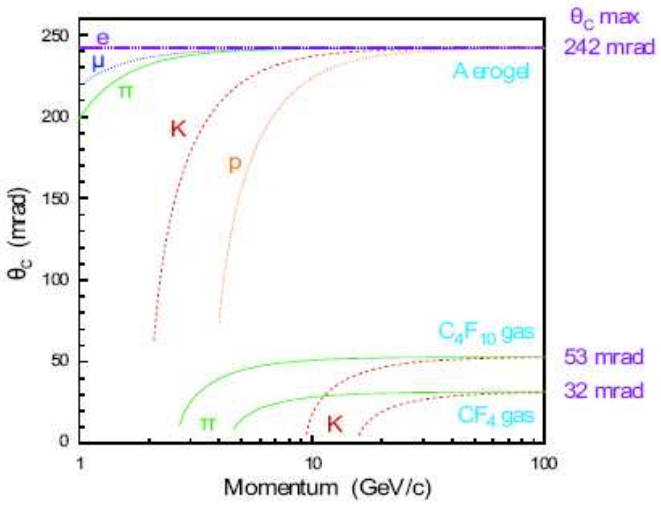

Figure 1.8: Cherenkov angle versus the particle momentum for the RICH radiators.

1.3.3 The magnet

The dipole magnet [7] is located close to the interaction point in order to keep it small, between the trigger tracker (TT) station and the remaining tracker stations (T1-T3) The field is oriented vertically which makes the track to bend in the horizontal $x - z$ plane. It has a maximum intensity of 1.1 T and a total integrated magnetic field of 4 Tm for 10 m long tracks. Charged particle passing through the magnet will receive a p_T kick of ~ 1 GeV/c.
Its aperture is 300 mrad in the bending plane and 250 mrad in the vertical one. The magnet is made of 50 tons of aluminum conducting wires and of 120 kt steel plate yoke. It dissipates about 4.2 MW.
To compensate a possible left-right asymmetries in the detector, the polarity of the magnet field can be reverse. This requirement and a detailed cost analysis have lead to the choice of a warm magnet rather than a superconducting magnet.

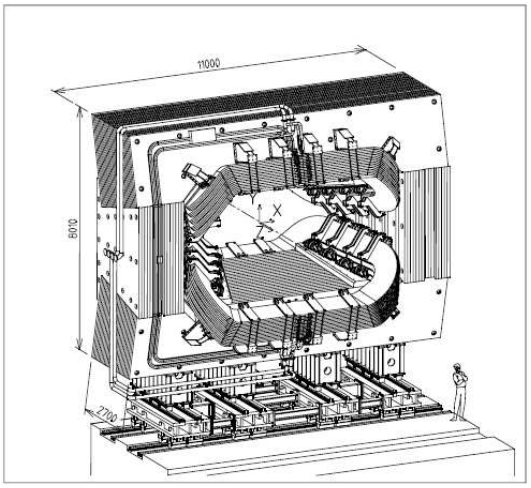

Figure 1.9: Perspective view of the LHCb dipole magnet,

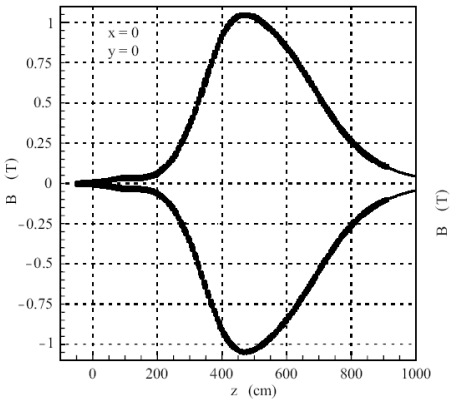

Figure 1.10: Magnetic field along the *z* axis.

1.3.4 The tracking system

The tracking system consists of four stations: the Trigger Tracker (TT), located downstream the RICH1 and in front of the entrance of the magnet, and the three stations (T1,T2, and T3), located between the magnet and the RICH2.

The Trigger Tracker [4] (TT) purpose is twofold.
In the High Lever Trigger, a first rough transverse momentum (20%–40%) estimation without using the other T stations is obtained by matching the tracks reconstructed in VELO with TT clusters, exploiting the fringe magnetic field present in the region (see Sec. 1.4).
In the off-line analysis it will be used to reconstruct the trajectories of long lived neutral particles, which decay outside the VELO, and of low momentum particle, which are bent out of the acceptance of the experiment before reaching the tracking stations T1-T3.
The station is composed of four layers, two of them giving redundantly the x coordinate, and the other two giving u and v stereo coordinates, rotated $\pm$ 5 ^{o} with respect to x one.
The layers are covered entirely by 300 μm thick silicon microstrip detectors with strip pitch of 200 μm and strip lengths of up to 33 cm. This allows to reach a spatial resolution of about 70 μm.

The T1-T3 stations provide the momentum measurement of charged particles and link the

tracks founded in the VELO to the hits in the TT station, in the calorimeters and in the muon detector. They also provide the seeding information for the RICH counters.
A mass resolution requirement of 10 MeV in high-multiplicity decays such as $B_s^0 \rightarrow D_s K$ translate to a momentum resolution requirement of δp/p $\leq$ 0.4%.
To reduce particle occupancy, the T1-T3 stations are segmented in a Inner Tracker, located close to the beam pipe, and a Outer Tracker, which covers the remaining 98% of the area. Four detector layers are present in both region, with the same x and stereo coordinates layout of TT.
The Inner Tracker [8] shares also the same technology of the Trigger Tracker, while the Outer Tracker [9] is made of straw tubes. These drift tubes have a 5 mm diameter and 75 μm thick walls. The Ar/CO_2 (70/30) drift gas mixture optimizes the spatial resolution ($\sim$ 200 μm) and the drift velocity, as well as the radiation hardness.
The total drift time, convolution of amplification and transmission time, is kept slightly below 50 ns. Requiring more computational time, the T1-T3 tracker information is used only in a later stage of High Level Trigger.

1.3.5 The Calorimeters system

The calorimeter system [10] identifies hadrons, electrons and photons and measures their energy and position. The information is used in the Level-0 trigger decision.
The detector design is a compromise between a small number of read-out channels and low occupancy, that results in a reasonable energy and position resolution.
It is placed downstream the RICH-2 and the first muon station (M1) and consists of an electromagnetic and a hadronic calorimeter (Fig. 1.11).
The electromagnetic calorimeter (ECAL) detects electrons and photons. It is a sampling calorimeter with lead as absorber material (25 X_0 total radiation length). It is segmented in three different granularity zones in order to optimize for the π^0 reconstruction.
A Preshower is present in front of ECAL, consisting of 15 mm of lead sandwiched between two almost identical plane of rectangular scintillator pads (SPD and PS, each 15 mm thick, i.e. $\sim$ 2.5 X_0). It allows the separation of photons and electrons showers induced in the ECAL on the basis of the different topology and it is used as a trigger veto in case of events with a too high charged tracks multiplicity.

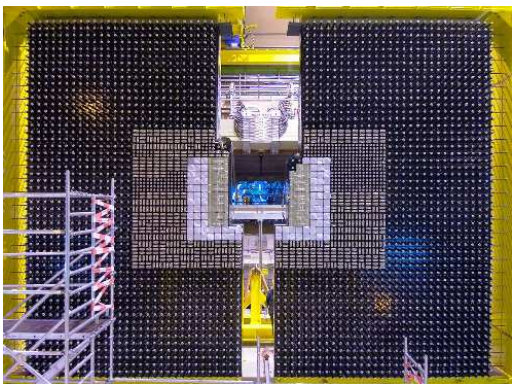
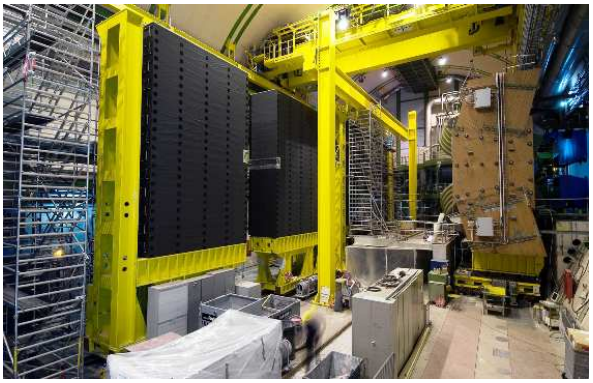

Figure 1.11: Pictures of electromagnetic (left) and hadronic (right) calorimeter during the installation.

The energy resolution of the ECAL is:

$$\frac{\sigma(E)}{E} = \frac{10\%}{\sqrt{E/GeV}} \oplus 1.5\%$$

The hadronic calorimeter (HCAL), allowing hadrons ($\pi^{\pm}$, $K^{\pm}$, K^0_L, p, n, Λ) detection via inelastic interactions with its passive material, is made of 16 mm thick iron and 4 mm thick scintillating tiles, parallel to the beam. The light is collected at the end of the tile by wavelength shifting fibers (WLS).
The energy resolution of the HCAL is:

$$\frac{\sigma(E)}{E} = \frac{80\%}{\sqrt{E/GeV}} \oplus 5\%$$

1.3.6 The Muon system

The Muon system [11] identifies muons as the only penetrating charged particle able to pass through the whole calorimeters system. As high p_T muons are mainly produced in B decays, the muon detector is an essential component of the Level-0 trigger. It also used in the muon identification which is a basic ingredient of the search for rare semileptonic decays.
The muon apparatus will be discussed in more details in the next chapter.

1.4 The LHCb trigger

The trigger is a crucial component of the LHCb experiment and most sub-detectors features are motivated by trigger considerations. The high interaction rate, the low b cross-section compared to the total cross-section and the high multiplicity of the events make the efficient selection of interesting B-decays the major challenge.

At the LHCb nominal luminosity of $\mathcal{L}$ =2$\times 10^{32}$cm^{-2}s^{-1} a 10 MHz effective visible collisions rate is expected, with a 25 ns bunch-crossing time structure. Given the ratio between total inelastic and $b\bar{b}$ cross-section, the $b\bar{b}$ pairs production rate can be around 100kHz, but the B-mesons decays relevant for physics analysis have very small branching ratio (10^{-3}–10^{-9}), so that the useful rate for physics analysis is only few tens of Hz. Taking into account also calibration and control channels, the trigger must efficiently select events up to fill the maximum 2 kHz bandwidth capacity of the disk.

The trigger scheme has been revised since the Trigger TDR [12] and the new layout is shown in Fig. 1.12. The Level-0 Trigger is mostly unchanged in the logic as well as in the implementation on hardware custom electronics; on the other hand the Level-1 Trigger is not longer required thanks to the great effort on all sub-detectors for a 1 MHz complete readout [13], and its logic is now part of the High Level Trigger, which has been largely reviewed [14].

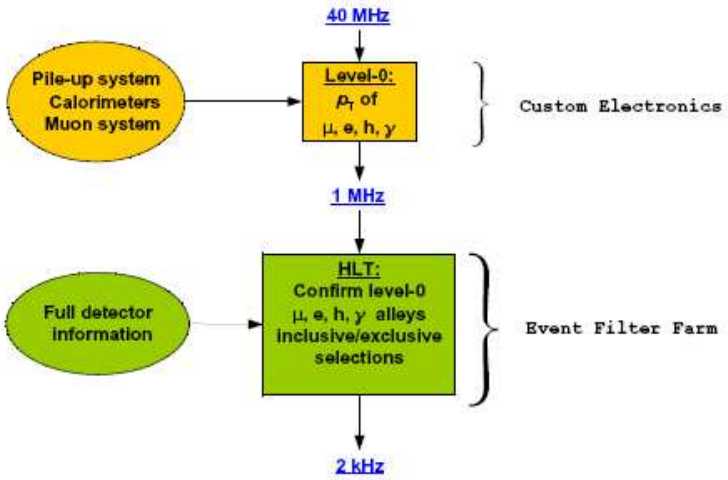

Figure 1.12: The LHCb trigger scheme. The Level-0 trigger uses information from muon detectors, calorimeters and pile-up VETO to reduce the event rate to 1 MHz. The HLT uses the information from all sub-detectors to write on disk only 2 kHz of events.

1.4.1 The Level-0 trigger

The main task of L0 trigger is to reduce the event rate to 1 MHz, at which the complete LHCb readout is possible.
It has accomplished by looking for high transverse momentum muons, or high transverse energy deposits in calorimeters for photons, electrons and hadrons, exploiting the large B mass with respect to the other charmed or lighter mesons.
The Pile-Up system, consisting of two VELO disks in the region backward of the interaction point, identifies multiple interactions and it is used to suppress events with multiple vertices hard to analyse. For the same reason, events are discarded in the case of a high charged tracks multiplicity detected in the SPD Preshower.
The Pile-Up and SPD Vetoes information, together with the highest p_T photons, electrons, hadrons and the two highest p_T muons, are passed to the L0 decision unit, which forms the final decision.
The fully synchronous L0 trigger has a fixed latency of 4 μs and is implemented on custom boards. Even if it is a hardware trigger, a tuning of the cuts is possible and efficiencies of 60%, 50% and 90% are expected for events with hadrons, electrons and muons respectively. The optimization of the cuts for the precise measurements of $\mathcal{CP}$-violating parameters leads a bandwidth of 70% for the hadron trigger, 28% for the electron and photon trigger, 16% for the muon trigger.

1.4.2 The High Level Trigger

If a L0 Decision is issued, the full detector data is read out and sent to an about 1800 CPU node Event Filter Farm (EFF), which implements the High Level Trigger (HLT) algorithm. Even with the full detector data accessible, the HLT aims to first reject the bulk of the events using only part of the available information.
It is composed by the so called *alleys* 1.13, where each *alley* address one the L0 trigger type (muonic, hadronic, and electromagnetic calorimeter) and enriches the b content of the events by refining momentum measurement and adding impact parameter information.
Most of the L0 triggers are of only one type, and only 15% of the triggers traverse more than one alley.
Events selected by at least one alley are processed by the inclusive selections, where specific

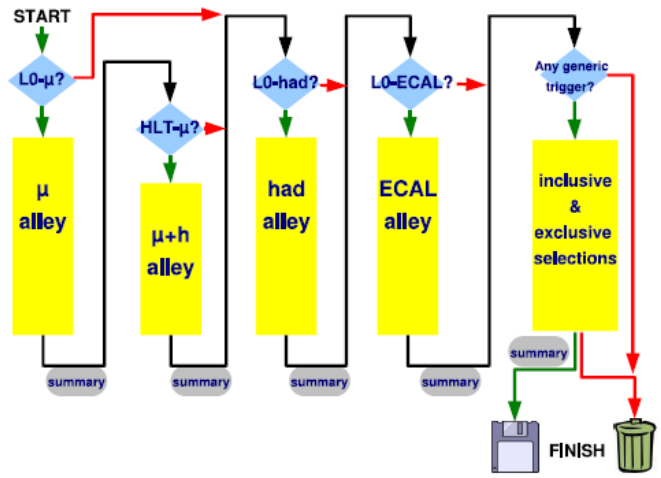

Figure 1.13: The HLT *alleys* structure. Only events passing at least one of the alleys are processed by inclusive and exclusive selections.

resonances are reconstructed, and the exclusive selections, which will reproduce the offline selections using looser cuts. An event is finally written on disk if it pass at least one of the inclusive or the exclusive selections.

The HLT is still evolving so the cuts and the bandwidth of each stream is not yet well defined, but Table 1.3 can give an idea of the proposed bandwidth share and the purpose of each stream.

Dimuon	600 Hz	Time unbiased dimuons with a mass above 2.5 GeV. These events are used to measure the uncertainty on lifetime measurements.
Inclusive B	900 Hz	Events with one high PT and IP muon, or a moderate PT and high-IP muon making a vertex with a high PT and IP hadron. Used for systematic studies of the trigger efficiency and for data mining. Because of the muon, this sample is highly tagging-enriched.
Exclusive B	200 Hz	The core physics stream with exclusively reconstructed decays. It also includes sidebands and control channels.
Inclusive	300 Hz	PID-blind D* events with D0->hh and no D0 mass cut. Allows to measure the PID efficiency and mis-ID rate. Can also be used for CP measurements in D decays.

Table 1.3: Proposed bandwidth of HLT streams

1.5 B-physics performances and sensitivity at LHC experiments

In comparison with the other accelerators that are in operation, LHC will be the most copious source of B mesons due to the high $b\overline{b}$ cross section as well as the high luminosity. Tab. 1.4 summarizes the features of the different colliders together with the B production.

	PEP-II	Tevatron	LHC
beam	e^+e^-	$p\overline{p}$	pp
center of mass energy $\sqrt{s}$	10.6 GeV	2 TeV	14 TeV
$\mathcal{L}$ [cm^{-2}s^{-1}]	3×10^{33}	2×10^{32}	10^{32}-10^{34}
$b\overline{b}$ pairs/years	3×10^{7}	2×10^{11}	10^{12}-10^{13}
σ_b	1.1 nb	100 μb	500 μb
σ_{in}	0.24 nb	50 mb	80 mb
ratio σ_b/σ_{in}	0.22	2×10^{-3}	6×10^{-3}
$B^+/B^0/B_s^0/B_c, \Lambda_b$ mixture	50/50/0/0	40/40/12/8	40/40/12/8

Table 1.4: Features of the different colliders compared to the LHC machine. The B physics is also reported.

In general, the advantage of the experiments on e^+e^- machine is the better signal to background ratio ($\sim$ 0.22), but the statistics is limited (10^7 $b\overline{b}$/years) with respect to a hadron machine. Furthermore at $\Upsilon(4s)$ center of mass energy only the two lightest B-mesons, B_u and B_d in equal proportion, are produced, while at LHC a variety of b-hadrons will be produced: B_u (40%), B_d (10%), B_s (10%) and B_c/b baryons (10%).
Physical observables related to $\mathcal{CP}$ violation [15] in the B_d^0 system has been measured with a very high accuracy in the asymmetric e^+e^- B factories (BABAR experiment at SLAC and BELLE experiment at KEK). From the decay $B^0 \to ()K^0$, BaBar and Belle have measured the angle β, sin2β = 0.678 $\pm$ 0.026 [16], with a high precision and in excellent agreement with the indirect measurement of V_{ub}/V_{cb} and Δm_d from semi-leptonic B^0 decays, and $B-\overline{B}$ oscillation.
On the other hand, the measurements of the angles α, coming from $B^0 \to \pi\pi$, $B^0 \to \pi\rho$ and $B^0 \to \rho\rho$ decays, and γ, coming from $B^+ \to D^0K^+$, are limited by the low statistics. Actually the measurements of these angle from the UTFit [17] are: sin2α = -0.047 $\pm$ 0.152 and γ = (66.7 $\pm$ 6.4)^o.
In Tab. 1.5 the current experimental results on the B physics are summarized as reported in the UTFit collaboration homepage [17], while in Fig. 1.14 the status on the Unitary Triangle.

Channel	Physical observable	Measurement (@95% C.L.)	Experiment
$B \to J/\psi K_s^0$	sin2β	0.690 ± 0.023	BaBar/Belle
$B \to \pi^+\pi^-$	sin2α	-0.047 ± 0.152	BaBar/Belle
$B \to DK$	γ	$(66.7 \pm 6.4)^o$	BaBar/Belle
$B^0 \to D^0\pi, D\rho$	$2\beta + \gamma$	$(111 \pm 13)^o$	BaBar/Belle
$B_s^0 - \overline{B}_s^0$ oscillation	Δm_s	17.7 ± 0.1 ps^{-1}	CDF/D0/LEP/SLD

Table 1.5: Current results on the B physics taken from the UTFIT homepage [17].

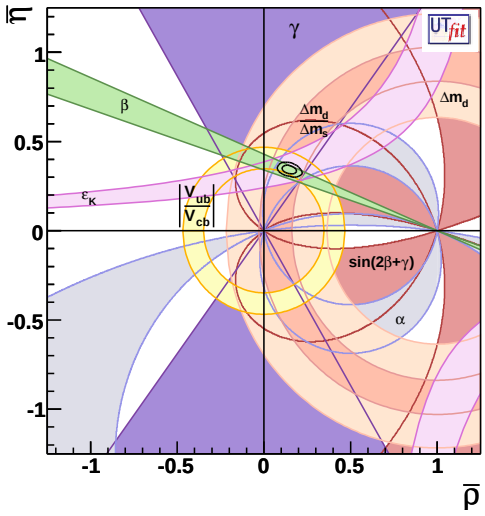

Figure 1.14: Allowed regions for ($\overline{\rho}$-$\overline{\eta}$). The closed contours at 95% probability are shown. The full lines correspond to 95% probability regions for the constraints, given by the measurements of $|V_{ub}|/|V_{cb}|$, ϵ_K, Δm_d, $\Delta m_d/\Delta m_s$, α, β, γ, $\Delta\Gamma_d/\Gamma_d$, $\Delta\Gamma_s/\Gamma_s$, A_{SL}^d and the dimuon asymmetry from D0 [17].

At the LHC energy, the high number of B_s-$\overline{B_s}$ pairs per years ($\sim 10^{11}$) will enable to measure the γ and $\delta\gamma$ angles and the triangle side opposite to γ angle (corresponding to $|V_{td}/V_{cb}|$) with a very high accuracy. Moreover, the physics potential of B_s^0 and the relative rare decays, which are absent at the tree level in the Standard Model (SM), will provide, in addition to the fulfillment of the studies of $\mathcal{CP}$ violation, a very fertile testing ground for the SM picture of flavour physics as well as interesting probes for new physics.

1.5.1 B-physics at LHCb, ATLAS and CMS experiments

At the LHC, B-physics will be studied with two general purpose ATLAS [18] and CMS [19] detectors, and the dedicated LHCb experiment (Tab. 1.6). ATLAS and CMS are designed for high luminosity running and provide hermetic coverage, which is essential for Higgs and SUSY discover, while LHCb have a detector geometry optimized for the requirements of the B-physics: as explained in Sec. 1.2, at the LHC energy, the $b - \overline{b}$ pairs are preferentially emitted under a small angle relative to the beam direction.

	LHCb	ATLAS/CMS
Detector configuration	Single-arm forward	Central detector
Running luminosity [$cm^{-2}s^{-1}$]	2×10^{32}	3×10^{34}
pseudo-rapidity range (η)	1.9 ÷ 4.9	-2.5 ÷ 2.5
$<$ interactions/crossing $>$	$\sim$0.4 ($\sim$ 30% single int.)	$\sim$ 23
$b\overline{b}$ pairs/years (integrated in the η range)	10^{12}	5×10^{13}

Table 1.6: Comparison of the LHC experiment parameters.

Fig. 1.15 shows the pseudo-rapidity as well as the transverse momentum coverage of the detectors. LHCb can measure p_T below 2 GeV/c and thereby, despite its small angular coverage $1.9 < \eta < 4.9$, has access to a visible b-cross section of about 230 μb. On the contrary, ATLAS and CMS, covering the central range $|\eta| < 2.5$ and operating at higher luminosity, have to raise the p_T-threshold to values around 10 GeV/c in order to achieve sufficient background rejection.

In addition, the presence of RICH detectors in LHCb allows to study with an high efficiency pure hadronic decays due to the high K-π separation (3σ) in a wide momentum range (1-150 GeV/c). On the contrary, ATLAS and CMS have no a dedicated hadronic particle identification detectors. For example, the Transition Radiation Detector (TRD) of ATLAS provides a dE/dx measurement giving a K/π separation of about 0.8σ, precluding most of the hadronic B decays.

Among the rare B decays, the $B_s^0 \rightarrow \mu^+\mu^-$ is the most interesting, since the current limit (5.8×10^{-8}, measured by CDF [20]) is approaching the foreseen SM branching ratio (about 3.5×10^{-9} [21]).

With its excellent muon detection capability, CMS can observe an estimated 26 signal events with 6.4 events background for 100 fb^{-1} of running, i.e. the first year of full luminosity

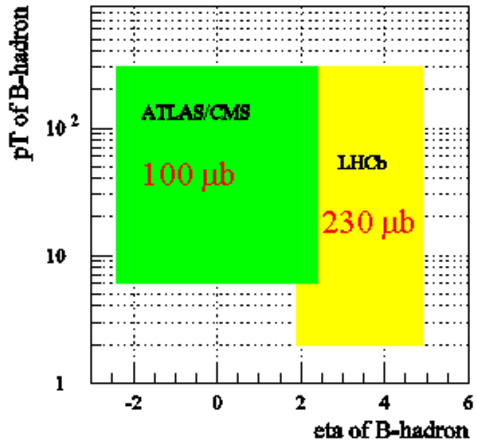

Figure 1.15: Phase space coverage of the LHC experiments for B-physics.

operation. On the other hand, also LHCb can arrive as well to the observation of this channel in the scenario of the SM, using its lower design luminosity, that will be reached since the first year of operation.

In Tab. 1.7 the sensitivity of LHCb and ATLAS/CMS are summarized for a selection of benchmark channels for one years of running, corresponding to an integrated luminosity of 2 fb^{-1} and 100 fb^{-1} respectively.

Channel	Physics Observable	LHCb	ATLAS	CMS
$B_d^0 \to J/\psi K_s^0$	β	0.3÷0.5 ^{o}	0.6 ^{o}	0.7 ^{o}
$B_d^0 \to \pi\pi$	α	2÷10 ^{o}	3 ^{o}	5 ^{o}
$B_d^0 \to \rho\pi$	α	5÷15 ^{o}	-	-
$B_d^0 \to D^0 K$	γ	4÷18 ^{o}	-	-
$B_d^0 \to D^*\pi$,3π	2β+γ	$< 7^o$	-	-
$B_s^0 \to J/\psi\Phi$	$\delta\gamma$	0.6^o	0.9 ^{o}	-
$B_s^0 \to D_s K$	$\gamma - 2\delta\gamma$	3÷16 ^{o}	-	-
$B_s^0 \to \mu^+\mu^-$	Rare decay	4.4σ S.M.	4.3σ S.M.	10σ S.M.

Table 1.7: Performance of the LHC experiments in a selection of benchmark channels for one year of operation at the relative luminosity. The quoted numbers are the errors on parameter in question. A dash for an entry means that no significant measurement can be made [22].

In chapter 5, where the possibility of the search of the rare $D^0 \to \mu^+\mu^-$ decay is investigated, an example of the potentiality of LHCb also in the charm sector is presented.

Chapter 2

The Muon System

Muon triggering and off-line muon identification are fundamental requirements of the LHCb experiment. Muons are present in the final states of many $\mathcal{CP}$-sensitive B decays, in particular the two "gold-plated" decays, $B_d^0 \rightarrow$J/$\psi(\mu^+\mu^-)$K$_s^0$ and $B_s^0 \rightarrow$J/$\psi(\mu^+\mu^-)\Phi$. Moreover, muons from semi-leptonic b decays provide a tag of the initial state flavour of neutral B mesons. In addition, the study of rare B decays such as the Flavour Changing Neutral Current decay, B$_s^0 \rightarrow \mu^+\mu^-$ may reveal new physics beyond the Standard Model.
The LHCb muon detector uses the penetrative power of muons to provide a robust muon trigger. The heavy-flavour content of triggered events is enhanced by requiring the candidate muons to have high transverse momentum, p_T. The same unique properties are utilized off-line, to accurately identify muons reconstructed in the tracking system and to provide a powerful B-meson flavour tag.

2.1 Physics requirements

The main requirement for the muon detector is to provide a high-p_T muon trigger at the earliest trigger level (Level-0). The effective LHCb Level-0 input rate is about 10 MHz on average at $\mathcal{L}$ = 2$\times$10^{32} cm^{-2} s^{-1}, assuming an inelastic pp cross-section of 80 mb. This input rate must be reduced to 1 MHz within a latency of 4.0μs, while retaining good efficiency for events containing interesting B decays.
The muon trigger must provide for about 20% of the total bandwidth. It is based on a fast muon track reconstruction and p_T measurement with a resolution of $\sim$ 20%. To unambigu-

ously identify the bunch crossing, the choice of detector technology must be driven by a high time resolution as well as a high detection efficiency.
The muon system must also provide offline muon identification. Muons reconstructed in the high precision tracking detectors with momenta down to 3 GeV/c must be correctly identified with an efficiency of above 90%, while keeping the pion misidentification probability below 1%. Efficient muon identification with low contamination is required both for tagging and for the clean reconstruction of muonic final state B decays.

2.2 General detector structure

The muon detector consists of five muon tracking stations placed along the beam axis.
The first station (M1) is placed in front of the calorimeter Preshower, at 12.1 m from the interaction point, and is important for the trigger transverse-momentum measurement because the hit in this station is not affected by the multiple scattering of calorimetric system material. On the other hand, the M1 station has as additional requirement a radiation length of the detector materials below 10% of X_0 on average, in order to not degrade the calorimeters measurements.
The remaining four stations, with an iron shield between them, are at mean positions of 15.2 m (M2), 16.4 m (M3), 17.6 m (M4) and 18.8 m (M5). The three iron filters and the electromagnetic and hadronic calorimeters correspond to 20 nuclear interaction lengths, and to traverse the 5 stations a muon must have a minimum momentum of 8 GeV/c.
The positions of the muon stations can be seen in Fig. 2.1, which shows a side view.
The chambers within the filter are allocated in about 40 cm of space and are separated by three shields of 80 cm thickness. The angular acceptances of the muon system is from 20 to 306 mrad in the bending plane and from 16 to 256 mrad in the non-bending plane, similar to the one of the tracking system. This provides a geometrical acceptance of about 20 % of muons from b decays with respect to the full solid angle. The total detector area is about 435 m^2.

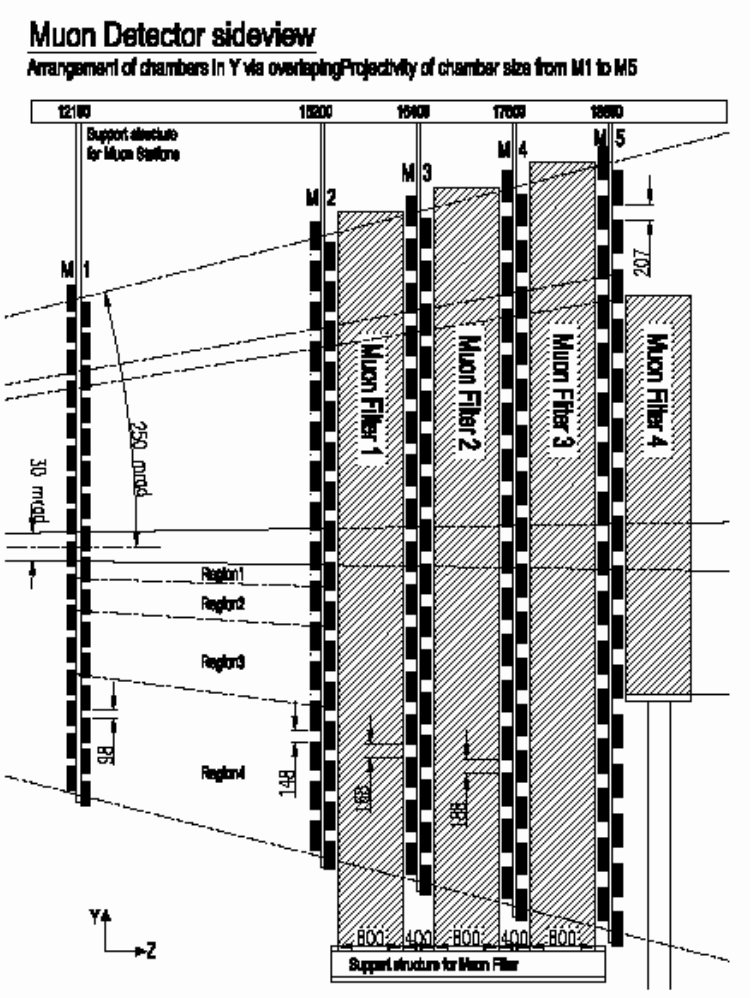

Figure 2.1: Side view of the muon system.

2.3 The station layout

The Muon system provides a digital information about the $x - y$ spatial coordinates of the muon tracks. The spatial resolution is given by the dimension of a logical pad, whose structure across the detector represents the logical layout. The logical layout describes the x and y granularity in each region of each muon station, as seen by the muon trigger and off-line reconstruction.

Since the polar angle and momentum of particles are correlated, high momentum tracks tend to be closer to the beam axis. Therefore multiple scattering in the absorber increases with the distance from the beam axis, limiting the spatial resolution of the detector. The granularity of the logical pads varies accordingly and have been chosen such that its contribution to resolution the trigger p_T measurements is approximately equal to the multiple-scattering contribution. The various contributions to the p_T resolution are shown in Fig. 2.2.

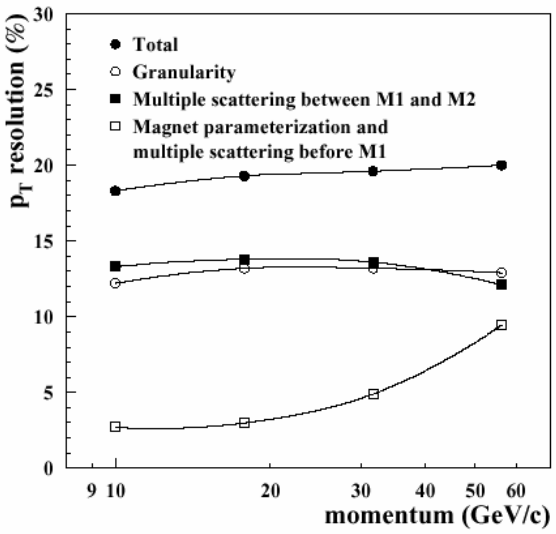

Figure 2.2: Contributions to the muon trigger resolution of transverse momentum measurement as a function of the muon momentum, averaged over the full acceptance. The p_T resolution is defined as $|p_{\mathrm{T}}^{rec} - p_{\mathrm{T}}^{true}|/p_{\mathrm{T}}^{true}$, and is shown for muons from semi-leptonic b decay having a reconstructed p_T close to the trigger threshold, between 1 and 2 GeV/c.

Given the different granularity and the large variation in particle flux from the central part, close to the beam axis, to the detector border, each station is subdivided into four regions

with different logical pad dimensions. Regions and pad sizes scale by a factor two from one region to the next.

In the y plane all the tracks appear to straight lines, as they are not bent by the magnet, thus the required granularity is broader, and the logical pads are wide, as appear in Fig. 2.3. The y dimension is determined principally by the rejection of background events which do not point to the interaction region.

Otherwise the x dimensions of the logical pads are determined primarily by the required precision to obtain a good muon p_T resolution for the Level-0 trigger.

The resulting y/x aspect ratios are 2.5 in station M1 and 5 for stations M2 and M3. Stations M4 and M5, which are used to confirm the presence of penetrating muons, have aspect ratios of 1.25. The total number of logical pads in the muon system is about 55 thousand.

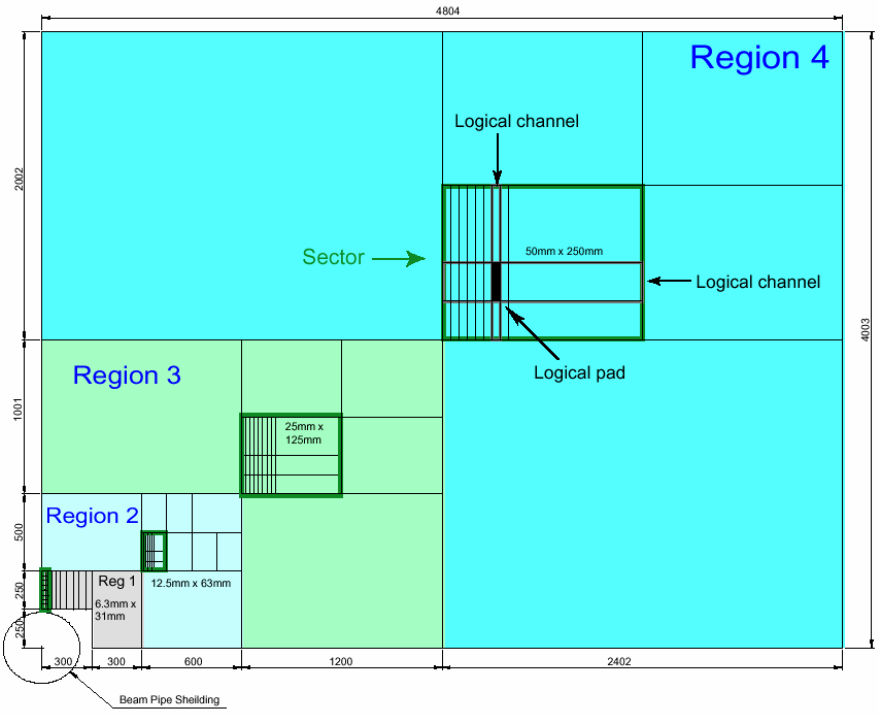

Figure 2.3: Front view of one quadrant of muon station 2, showing the dimensions of the regions. Inside each region is shown a sector, defined by the size of the horizontal and vertical strips. The intersection of the horizontal and vertical strips, corresponding to the logical channels, are logical pads. The region and channel dimensions scale by a factor two from one region to the next.

Each logical pad may group one or more physical pads, whose dimension are limited by

occupancy and capacitance considerations, according to the detector technology. The Muon system has been designed in a flexible way, such that the required logical layout can be achieved in several ways and is independent from the type of detector used (Fig. 2.4).

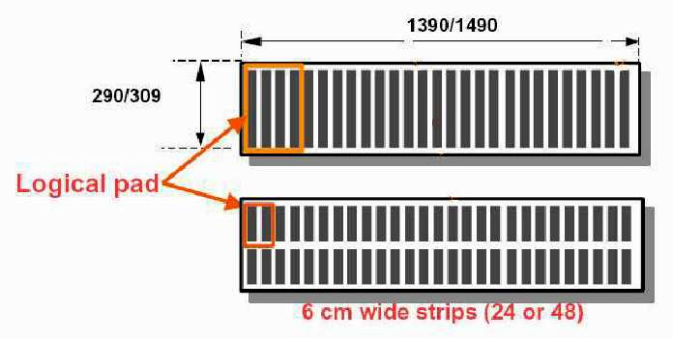

Figure 2.4: Logical pads and physical pads in Region 4 (top) and Region 2 (bottom) for Stations M4 and M5. In the former case the x dimension is that of 4 chamber strips and the y dimension is the same of the chamber itself. In the latter case more granularity is required and both x and y have half dimensions.

2.4 The level-0 muon trigger

The muon level-0 trigger (L0) looks for muon tracks with a large transverse momentum, requiring information from all five muon stations. The track finding is performed on the logical pad layout and the scheme shown in Fig. 2.5 is adopted. Starting from each hit in M3, called *track seed*, a straight-line is extrapolated towards the interaction point and is extended backward up to the station M5. In M2, M4 and M5, hits are looked for a regions, the so-called *field of interest* (FOI), centered in the intersections between the station and the straight-line. If at least one hit is found in M2, M4, M5 FOIs, the track is flagged as a muon candidate. A second straight-line passing through the hit in M2 and the track seed, is extrapolated to M1 to define the center of the FOI. If at least one hit is found in the M1 FOI, the track is definitely flagged as a muon.

Since the logical layout is projective, there is a one-to-one mapping from pads in M3 to pads in M2, M4 and M5. There is also a one-to-one mapping from pairs of pads in M2 and M3 to pads in M1. This allows the track-finding algorithm to be implemented using only logical operations.

Once track finding is completed, an evaluation of p_T is performed for muon tracks. The p_T is

determined from the track hits in M1 and M2. Because of the distance between M1 and M2 (3.1 m) and the high granularity of M1, a good resolution of the p_T measurement, $\sim 20\%$, is obtained. The momentum measurement assumes a particle from the interaction point and a single kick from the magnet.

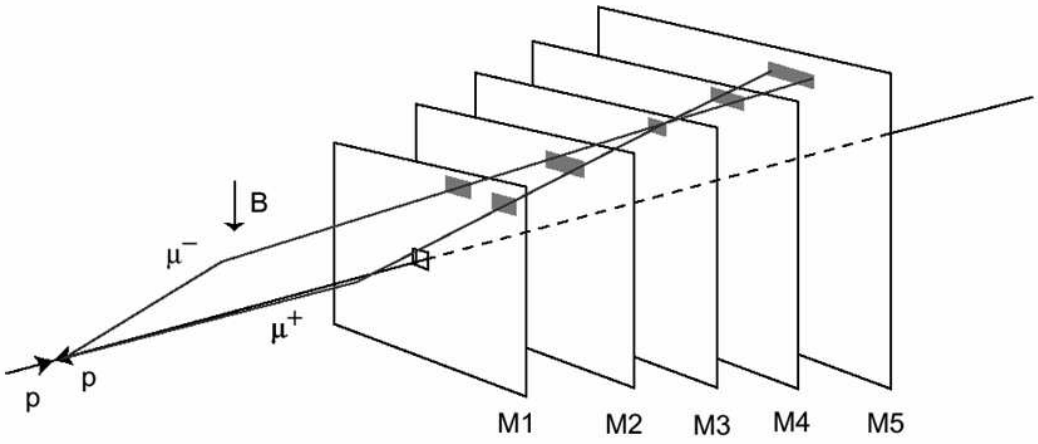

Figure 2.5: Track finding by the muon trigger. In the example shown, μ^+ and μ^- cross the same pad in M3. The highlighted in the various station represent the field of interest where the hits are searched.

A first consequence of this scheme is that the L0 trigger efficiency is highly affected by the single station efficiency, as follows:

$$\epsilon_{trigger} = (\epsilon_{station})^5$$

where $\epsilon_{station}$ is defined in a fixed time window of 20 ns because the hit must be also assigned to the correct bunch crossing, which are separated by 25 ns.
In order to improve the single station efficiency, providing also some redundancy, the M2-M5 stations consist of four independent detector layers, and the hits of the station is the logical OR of the hits of all layers. Only two detector layers are foreseen for the M1 station in order to reduce the material budget in front of the calorimeters.
The efficiency for M2-M5 stations must be $> 99\%$, and $> 96\%$ for the M1 station, due to the presence of only two detector layers.
As result of such stations efficiencies, the L0 muon trigger efficiency comes out to be higher than 92%.

2.4.1 Background environment

The high hit rates in the chamber affect the muon transverse momentum resolution due to incorrect hit association. Four classes of backgrounds relevant to the B$\rightarrow \mu$X detection can be distinguished:

1. *Decays in flight muons:* The large number of π/K mesons produced in the $p-p$ collisions contribute mainly to the background in the muon system through decays in flight. Such decay muons form the main background for the L0 muon trigger.

2. *Shower particles:* Photons from π^0 decays can interact in the area around the beam pipe and generate electromagnetic showers penetrating into the muon system. Hadrons emerging from the primary collision can interact later in the calorimeters and contribute to the background in the muon system through shower muons or hadron punch-through.

3. *Low-energy background:* Another important background is associated with low-energy neutrons produced in hadronic cascades in the calorimeters, the muon shield or in accelerator components. They create low-energy radiative electrons via nuclear n-γ processes and subsequent Compton-scattering or via the photo-electric effect in the detector material of the muon chambers. The photons have a probability of a few per mil to generate detectable electrons via these effects, which are in general only affecting a single detector layer. Moreover, the hits due to the low energy background can occur delayed up to a few 100 ms after the primary collision.

4. *Beam halo muons:* The charged-particle flux associated with the beam halo in the accelerator tunnel contains muons of a rather wide energy spectrum and the largest flux at small radii. In particular those halo muons traversing the detector in the same direction as particles from the interaction point can cause a L0 muon trigger.

Background caused by real muons traversing the detector is well simulated with the available Monte Carlo packages [23], [24]. An estimate for the rate in the various regions of the muon system has been obtained from a detailed study [25], [26], whose results are summarized in Tab. 2.1.

The nominal rates are calculated for a luminosity of $\mathcal{L}$ = 5$\times$10^{32} cm^{-2} s^{-1}. The maximal rates are then obtained applying a safety factor of 5 in the stations M2–M5 and a safety factor of 2 in the station M1, which is positioned in front of the calorimeters and therefore is less affected by the uncertainties in the showering processes in the absorber material. The

	Station 1	Station 2	Station 3	Station 4	Station 5
Region 1	230 kHz/cm^2	7.5 kHz/cm^2	2 kHz/cm^2	2.3 kHz/cm^2	880 kHz/cm^2
	460 kHz/cm^2	37.5 kHz/cm^2	10 kHz/cm^2	6.5 kHz/cm^2	4.4 kHz/cm^2
Region 2	93 kHz/cm^2	5.3 kHz/cm^2	650 Hz/cm^2	430 Hz/cm^2	350 Hz/cm^2
	186 kHz/cm^2	26.5 kHz/cm^2	3.3 kHz/cm^2	2.2 kHz/cm^2	1.8 kHz/cm^2
Region 3	40 kHz/cm^2	1.3 kHz/cm^2	200 Hz/cm^2	150 Hz/cm^2	130 Hz/cm^2
	80 kHz/cm^2	6.5 kHz/cm^2	1.0 kHz/cm^2	750 Hz/cm^2	650 Hz/cm^2
Region 4	12.5 kHz/cm^2	230 Hz/cm^2	83 Hz/cm^2	50 Hz/cm^2	45 Hz/cm^2
	25 kHz/cm^2	1.2 kHz/cm^2	415 Hz/cm^2	250 Hz/cm^2	225 Hz/cm^2

Table 2.1: Particle rates in the muon system.The first row gives the calculated rate at a luminosity of $\mathcal{L}$ = 5×10^{32} cm^{-2} s^{-1} assuming a total $p-p$ cross-section of σ=102.4 mb; in the second row the rate includes the safety factors.

rate rises from a few hundred Hz/cm^2 in the outer regions of stations M4 and M5 to a few hundred Hz/cm^2 in the innermost part of station M1.

2.5 Muon system technologies

High particle fluxes in the muon system impose stringent requirements on the instrumentation. These requirements include the rate capability of the chambers and the robustness after long-term irradiation, that must be taken into account together with the required performance for the prefixed physics goal. The technology choice has been determined by the following parameters:

1. *Rate capability:* The selected technologies must tolerate the expected particle rate without efficiency losses;
2. *Ageing robustness:* The detector must tolerate, without damages or performance losses, the integrated charge accumulated in 10 years of operation;
3. *Time resolution:* The muon system must provide unambiguous bunch crossing identification with high efficiency. The requirement is at least 99% efficiency within 20 ns window for M2-M5 stations, and at least 96% for M1 station.
4. *Spatial resolution:* A good spatial resolution is required, especially in M1 and M2, in order to obtain an accurate p_T evaluation ($\sim$ 20%). Therefore it is important to reduce as

much as possible the probability of having more than one pad fired by a crossing track. This effect is described as geometrical pad cluster size. Depending on the average crossing angle of the track, the pad size and the layer separation, the geometrical pad cluster size varies between 1.1 in the outer part and 1.2 to the inner part of the muon system;

Based on the above considerations, the $\sim$ 99% of the area of the Muon system will be equipped with Multi Wire Proportional Chamber (MWPC) [27]. The innermost region (R1) of the first station (M1), where a particle flux up to $\sim$ 500 kHz/cm^2 is expected, will be instrumented with triple-GEM detectors (Gas Electron Multiplier) [28]. It should be stressed that the M1R1 region, of about $\sim$ 0.6 m^2 area, will be crossed by about the 20% of the total triggered muons.

The technical specifications and the performances of the MWPC detectors are summarized in the following section, while the performances of a triple-GEM detector, the subject of my thesis, will be discussed in detail in the following two chapters.

2.5.1 MWPC detectors

The MWPC chambers for the station M2-M5 are composed by four symmetric gas gaps, each of them with a plane of anode wires in between of two cathode planes. The gap is 5 mm wide and the anode-cathode distance is 2.5 mm. The wires are made of gold-plated tungsten with a diameter of 30 μm and a pitch of 2 mm. A schematic view is given in Fig. 2.6, while in Tab. 2.2 are summarized the main parameters of the MWPC detectors.

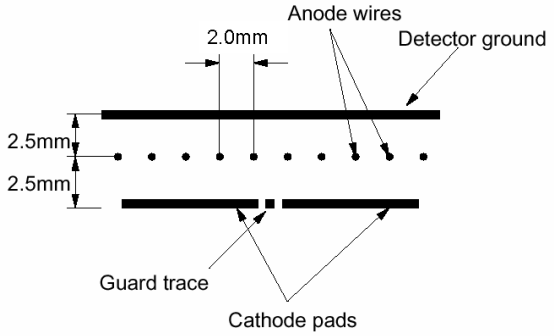

Figure 2.6: Schematic view of one sensitive gap in a MWPC.

Parameter	Design value
No. of gaps	4
Gap size	5 mm
Anode-Cathode distance	2.5 mm
Wire Diameter	30 μm
Wire pitch	2 mm
Wire tension	70 g
Gas mixture	$Ar/CO_2/CF_4$ (40/50/10)
Primary ionisation	$\simeq 10\,e^-$/mm
Gas Gain	$\simeq 10^5$
Threshold	> 5 fC

Table 2.2: Main LHCb MWPC parameters.

Chambers are readout in different way, depending on their position in the muon system:

- In region R4 of all the five stations, the chambers have anode-wire readout through decoupling capacitors;
- In region R3 of all the five stations and in regions R1 and R2 of stations M4 and M5 cathode pads are readout;
- In regions R1 of stations M2 and M3 and in regions R2 of stations M1 – M3 a combined readout of wire and cathode pads is used.

Anode wires are grouped into vertical strips to measure x whereas the y coordinates are provided by the granularity of the horizontal cathode pads.
Wires are grouped in pads of 4 to 42 to match the required granularity, varying from 6 mm in region R1 of station M2 to 62 mm in region R2 of station M5. The Muon system requires 864 MWPC chambers, with $\simeq 2.5\times10^6$ wires and about 80,000 front-end channels.

Five centers are foreseen to produce the whole MWPC chambers: one in S.Petersburg's Nuclear Physics Institute (PNPI), three in Italy (Ferrara, Firenze and Laboratori Nazionali di Frascati) and one at CERN. These centers have been equipped with similar tools, which are automated in order to speed up the construction and to achieved the required mechanical precision and tolerance. The details of the MWPC construction is reported in Ref. [27].

MWPC performances

An intensive programme of development work has been undertaken. Several MWPC prototypes have been constructed according to the different read-out requirement and the relative performances have been measured in various tests beam and in laboratory.
For completeness, I report some results obtained on the full size prototype with cathode-pad readout for Region 3 of Station 3 (M3R3). The chamber prototype have been built in the Laboratori Nazionali di Frascati with the final design, materials and construction procedure. The measurement have been performed at the T11 beam line at CERN PS with 3.6 GeV/c pions. In Fig. 2.7 is shown the efficiency in 20 ns window and the pad cluster size as function of the high voltages for a MWPC station. A wide working region, defined as the HV range between the onset of efficiency plateau (99%) and the HV at which the pad cluster size is under 1.2., of about $\sim$ 200 Volt, is obtained for an electronics threshold of 7 fC.

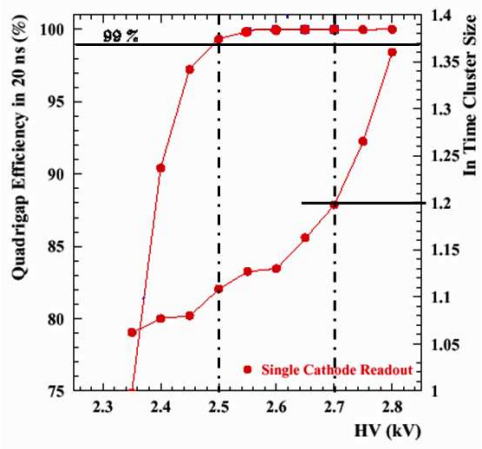

Figure 2.7: Efficiency in 20 ns time window and in-time pad cluster size as a function of the high voltage (HV) for a MWPC station [29].

Global ageing tests have been performed at the ENEA-Casaccia in the Calliope gamma facility with a ^{60}Co source. The test has been performed together with our full size triple-GEM detectors and it will be discussed in Sec. 4.5.
During this test the MWPC integrated $\sim$ 500 mC/cm of wire equivalent to $\sim$ 5 years of operation at LHCb experiment [30].

2.6 Electronics

The muon system front-end electronics (FEE) produces the digital output signals from detectors and transfer the information to the L0 muon trigger as quickly as possible [31]. The readout electronics chain comprises the following elements:

- *CARDIAC boards* directly on the chambers. The board is equipped with amplifier, shaper and discriminator chips called CARIOCA, and a DIALOG chip that combines the output signals of the CARIOCA to form logical channels;

- *Intermediate (IM) boards* placed on the side of the muon apparatus, to generate logical channels for those regions where this has not been possible on the chambers, because the logical channels are made of physical channels belonging to different chambers;

- *Off-Detector Electronics (ODE) boards*, also located on the side of the apparatus, where the data is synchronised and dispatched to the L0 trigger.

Such electronics must fulfill stringent requirements also in term of radiation hardness due to their location in the cavern. As an example, the specifications of CARIOCA chips [32] are summarized in Table 2.3.

Parameter	Specification
Maximum signal rate	1 MHz
Maximum total dose	1 MRad
Peaking time	$\sim$ 15 ns (C_{det}=250 pF)
Input resistance	$< 50\,\Omega$
Average pulse width	< 50 ns (CARIOCA output)
ENC (r.m.s) for the positive amplifier	1880e^-+45$e^-\times C_{det}$ (pF)
ENC (r.m.s) for the negative amplifier	2240e^-+42$e^-\times C_{det}$ (pF)
Sensitivity	$\sim$ 16 mV/fC

Table 2.3: Front-end CARIOCA chip parameters [32].

Chapter 3

The Gas Electron Multiplier

Fifty years ago, a radical innovation in the field of radiation detectors came from the invention of the Multi-Wire Proportional Chamber (MWPC) by Charpak [33].
The good position accuracy and rate capability, the modularity and the possibility to instrument large areas at relatively low cost, are all features that let the MWPC and their descendants, such as drift and time projection chambers, spread from high energy physics experiments up to astro-particle physics and medical applications.
Nevertheless, with the coming of new high luminosity colliders, the MWPC has shown some limitations concerning the capacity to tolerate the very high radiation fluxes.
To overcome these limitations, a new class of gas detectors, called *micro-pattern gas detectors* (MPGD), has been developed since twenty years, and some of the technologies born from that R&D are nowadays well-established, with several experiments exploiting them and many future experiments planning to do that.
This chapter will explain the passage from MWPC to MPGD in the next section, focusing then from Sec. 3.2 to Sec. 3.6 to the description of Gas Electron Multiplier technology, that is the subject of my thesis. Eventually, Sec. 3.7 to Sec. 3.8 will describe the R&D performed by our group on new fast gas mixture, in order to qualify this technology for the instrumentation of the region around the beam pipe of the LHCb-M1 station.

3.1 From Multiwire Proportional Chamber to Gas Electron Multiplier Detectors

The limitation of rate capability in wire detectors is due to the low drift of ions from the anode wire towards the cathode. In fact, at high particle flux, the ion cloud generated around the wire creates a positive space charge that reduces the electric field near the wire, leading to a *rate-dependent* gain drop. For a MWPC the maximum rate capability, depending on the detector geometry (wire pitch, anode-cathode wire distance), is generally below 1 MHz/cm^2 [34].

An improvement in rate capabilities comes from the reduction of wire-cathode distance, in order to speed up ions collection. However, below 1 mm wire spacing and below 2 mm anode-cathode gap, the MWPC becomes difficult to operate because of electrostatic instabilities arising from the mechanical tolerances.

The first example of the micro-pattern detector was the Micro-Strip Gas Chamber (MSGC) introduced by Oed [35] in 1988 and extensively developed by other authors in the following years [36]. The new device improved the rate capability and the position accuracy by more than one order of magnitude. The detector geometry is shown in Fig. 3.1: the anode and the

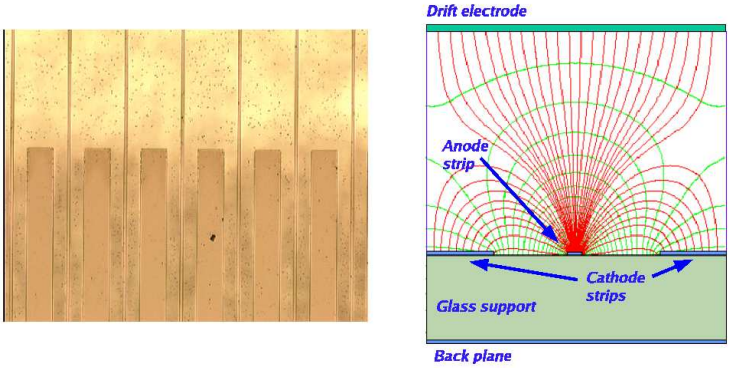

Figure 3.1: Micro Strip Gas Chamber: left) picture of the anode and cathode strips; right) sketch of the detector.

cathode are thin metallic strips which are placed on an insulating support. The upper electrode, called drift electrode, is used to define the drift region. A further electrode behind the insulating support, the back-plane, can be segmented as orthogonal strips giving the second coordinate.

The strips, alternatively connected to positive and negative voltage, act as a multi-anode pro-

portional counter. The electrons, produced by the radiation crossing the detector in the drift region, move towards the anode strips where they are multiplied. The ions produced in the avalanche are mainly collected in the neighbouring cathode strips typically 100 μm distant from the anode.

Standard photolithography technology allows to produce $0.3 \div 0.5$ μm thick cathode and anode strips with 100 μm of pitch. The manufacturing process is the same used for the production of multi-layer printed boards.

Operating instabilities were observed in the early device due to the charging-up of the insulating support. In fact when high particle flux crosses the detector, a part of the multiplication ions could be collected on the insulating support. This accumulated charge produces a change of the electric field between the strips changing the detector gain. This effect, which is rate dependent, could be reduced or eliminated using slightly conducting supports [37], and rate capability up to 100 MHz/cm^2 could be achieved [38].

MSGCs appeared however rather susceptible to aging and discharge damages.

Long-term studies have shown a slow degradation of performances, attributed to the formation of polymers in the avalanche. Anyway, with the proper choice of the components, as gas mixture and detector materials, a long-term survival up to collected charge above 100 mC per cm of strip equivalent to about ten years of operation at LHC has been demonstrated [39].

The appearance of destructive discharges appeared instead to be a more serious problem. In fact, a transition from avalanche to streamer, which is gas gain and ionization density dependent, could easily followed by a discharge due to the short distance of the electrodes. The discharge could heavily damage the strips increasing the dead channels population on long-term operation. This limitation is particular apparent in the new luminosity colliders, where among the particles to be detected, rare but heavily ionizing tracks (nuclear fragments, gamma and neutron conversions) are present. Thus a gain arrangement, that allows at the same time the detection of minimum ionization particles (m.i.p.) excluding the damage produced by the crossing of heavily ionizing particles, is very challenging [40].

Motivated by the above mentioned problems, a great effort has been made to find a more rugged alternative detector to the MSGC. In fact in the following years many of such detectors have been invented (Fig. 3.2): the microgap chamber (MGC) [41], the Microdot [42], the "Compteur $\grave{a}$ Trous" (CAT) [43], the Micromesh gas chamber (MicroMeGas) [44], the Micro-Groove [45] and the WELL [46] detectors.

Among the micro-pattern detectors the *Gas Electron Multiplier* (GEM), proposed in the 1997

by F. Sauli [47], introduced some peculiarities that contributed to its success. In the GEM detector the conversion, the multiplication and the signal induction regions are physically distinct, resulting in a greater freedom in the readout geometry. Moreover, the possibility to divide the multiplication in more steps allows to drastically reduce the problem of discharge and the ageing processes.

Nowadays this technology is well established, and it has essential tasks in several high energy experiments, such as for example COMPASS [48], TOTEM [49] and LHCb, as I explain in this dissertation.

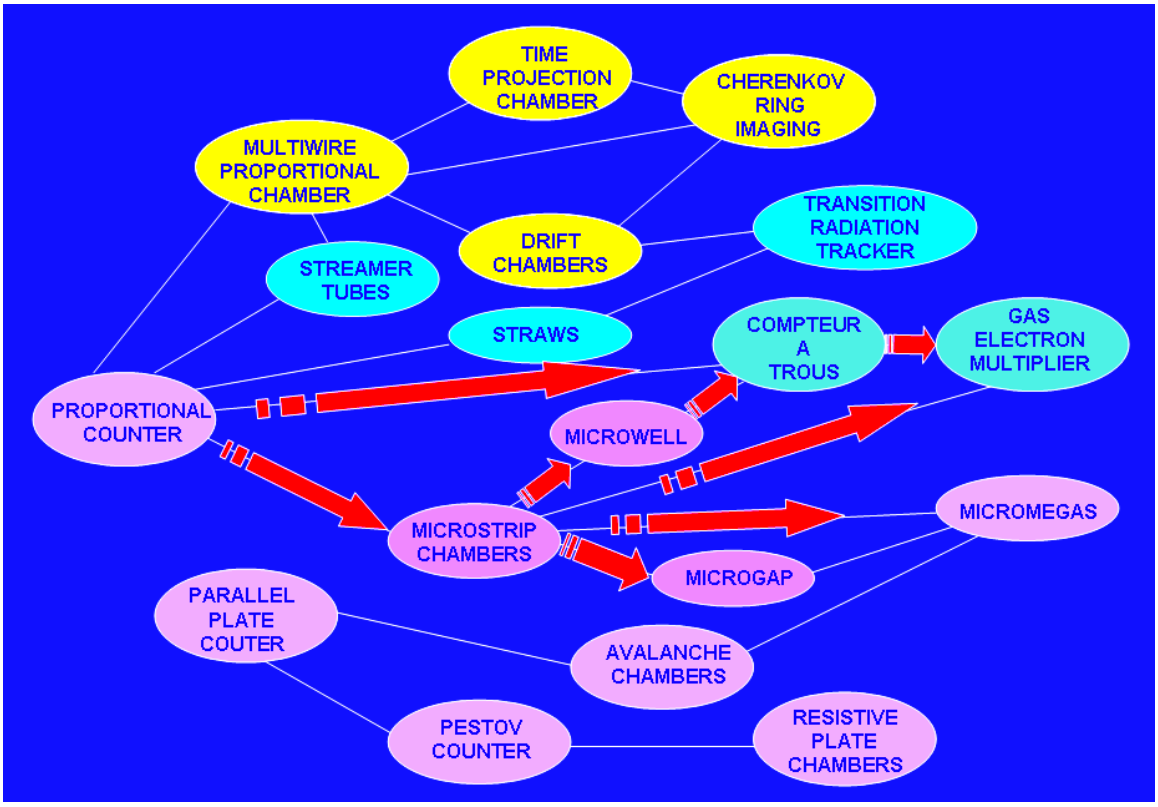

Figure 3.2: The gas detector family tree.

3.2 The GEM idea

The Gas Electron Multiplier (GEM) is a 50μm thick insulating kapton foil, clad on each side with a thin copper layer (5μm) and chemically perforated with a high density of holes. The holes have a bi-conical structure with an external diameter of 70 μm and internal of 50 μm and a pitch of 140 μm [51] (Fig. 3.3).

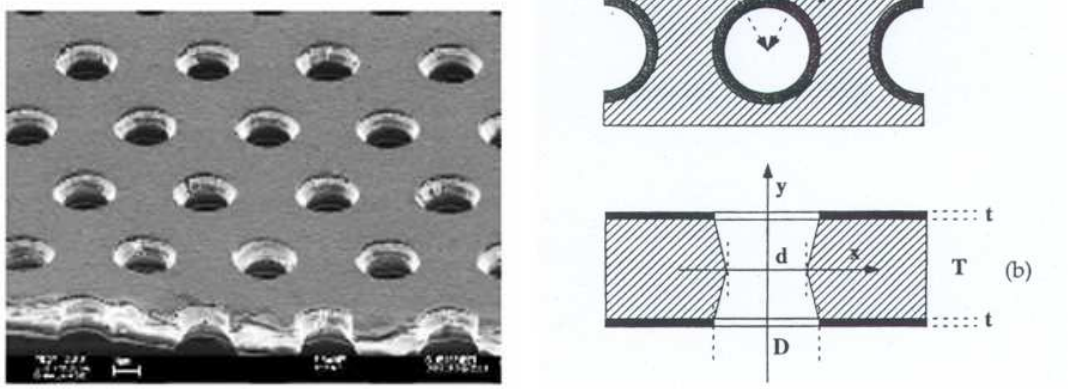

(a) GEM foil as seen at the electron microscope.

(b) Cross section of the geometry of GEM foil and the bi-conical shape of the holes.

Figure 3.3: The GEM foil

In a GEM detector the hole acts as a multiplication channel for the electrons released by ionizing radiation in the gas mixture. Applying a suitable voltage difference (300$\div$500 V) between the two copper faces, a high electric field ($\sim$ 100 kV/cm) is generated inside the holes. In this region, an electron could acquire enough energy to develop an avalanche. The reachable gain with a single GEM can be greater than 10^3.

The GEM manufacturing technology is realized using conventional photolithography methods [52].

The process starts with the production of two identical masks, whose pattern is transferred to the photo-resist coated foils by exposure to UV light. For large size GEMs, a crucial parameter is the precise alignment of the two masks. Indeed, since the patterned copper layer is used as a mask during the chemical process of the kapton etching, any misalignment between the two masks results in slanted holes, yielding lower gain. This is a particularly difficult requirement due to the use of plastic masks that can deform under thermal stress. The shape of the holes is successively obtained by the immersion of the patterned foil in a solvent. The GEM manufacturing processes is summarized in Fig. 3.4.

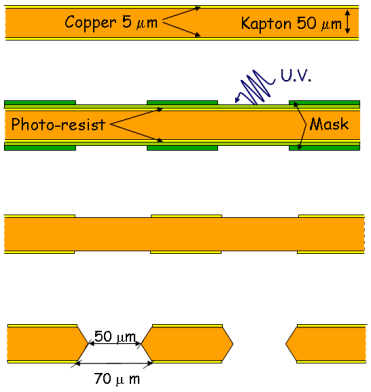

Figure 3.4: GEM manufacturing technology. From the top: commercially available kapton foil; the double mask alignment and the photolithographic process; copper etching by chemical solution; kapton etching using the copper layers as masks.

The choice of the geometrical parameters of a GEM foil, as the hole diameter, the pitch and the hole shape, and the manufacturing technique are a compromise between production yield [1] and safe operation of the detector [54].

[1] At present, different techniques, based on laser and plasma etching methods [53], have been used for GEM manufacture. Using these techniques, the production of the holes is more complex and slower than the chemical one. Moreover, these methods could produce local defects, such as the creation of metal "bridges" inside the hole which compromise the GEM operation.

3.2.1 Influence of hole diameter

In order to achieve a higher gain, the field lines density in the amplification channel can be increased by raising the voltage difference between the upper and lower GEM electrodes, or by reducing the hole diameter. Fig. 3.5 shows the correlations between the effective GEM gain and the hole diameter, measured at equal gas mixture and electric fields conditions. A gain saturation effect is observed for hole diameter below $\sim$ 70 μm which, as will be discussed in Sec. 3.3.4, is due to the increasing losses of electrons of the avalanche that hits the internal kapton surface or are collected by the lower GEM electrode. The saturation effect, while limiting the possible gain enhancement, has the very positive effect of reducing substantially the dependence of the detector gain from the precision of the manufacturing process.

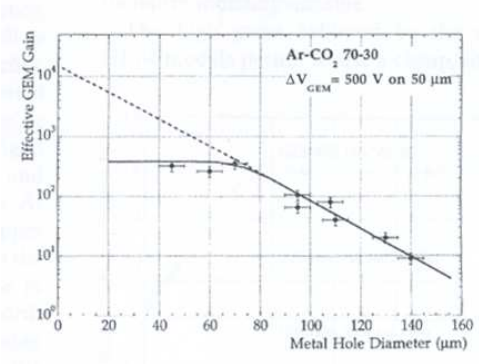

Figure 3.5: Measured effective gain of GEMs in Ar/CO_2 (70/30) with different metal hole diameters. The exponential fit to the points extrapolated to the expected gain for a 50 μm thick parallel plate geometry deduced from the known value of the Townsend coefficient [54].

3.2.2 Influence of hole pitch

The hole pitch does not play a direct role on the gain behavior, but when combined with the hole diameter, affect the *collection efficiency* of the electrons released in the upper volume of the GEM foil into the holes. The *collection efficiency* is correlated with the so called *electron transparency* [2]; as will be discussed in the Sec. 3.3.4, it gives a measure of the electrons losses crossing a hole due to different effects, and plays an important role in the

[2] At this point, the concept of the electron transparency can be understood through the optical transparency. The latter is defined as the ratio between the total area of holes and the total area of the foil: $t=\pi D^2/2\sqrt{3}P^2$ where D is the external diameter and P the pitch and a cylindrical shape of the hole is assumed. A higher optic transparency is achieved by reducing the pitch value at a fixed hole diameter.

detector performances.
At this level, it is possible to deduce that a high *collection efficiency* is achieved with a small pitch, as shown in Fig. 3.6.

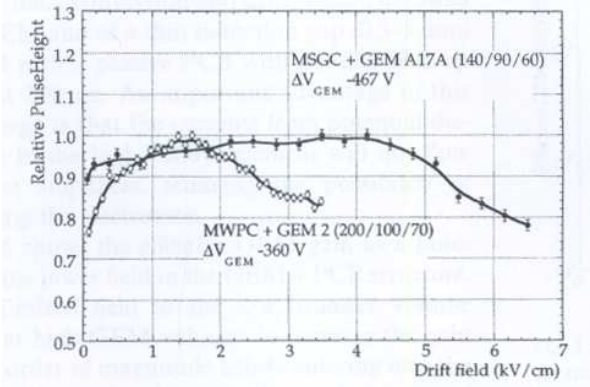

Figure 3.6: *Collection efficiency* as a function of drift field in a GEM of 140 μm pitch and 90 μm holes and a GEM of 200 μm pitch and 100 μm holes [54].

3.2.3 Influence of hole shape

The hole shape affects the *charging-up*, a short-term rate-dependent instability of the electrode resulting as a small increase of the gain due to the presence of the kapton insulating close to the multiplication channels. In fact, the electrons and the ions from the avalanche, collected and accumulated on the insulating kapton surface, produce an alteration of the electric field inside the multiplication channel. The hole geometry which best minimizes this effect is the cylindrical shape, as shown in Fig. 3.7.
The choice of a bi-conical shape is a compromise between a good production yield and the limited charging-up effect with respect to the conic shape [3] [54].

[3]Recently a new single mask technique is under development at CERN for the realization of a *"early cylindrical"* hope shape. Such a technique will open the way for the production of very large size GEM foils (limited only by the manufacturing tools dimensions), since the current limits of GEM foils size is mainly due to the alignment issues of the double mask technique, more difficult as the foil increases in size.

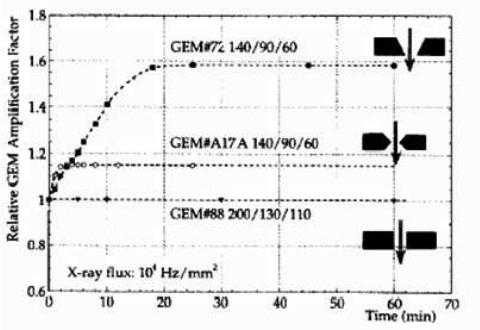

Figure 3.7: Time dependence of the gain for several hole shapes under a particle rate of 10^4 Hz/mm^2 [54].

3.3 The single GEM detector

The first gas detector based on GEM technology is obtained by inserting a single GEM foil between two flat parallel electrodes [55]. The upper electrode plays the role of cathode while the lower one is the readout anode.

The cross section of a single-GEM detector is shown in Fig. 3.8, together with the labeling of the different detector parameters.

The drift field, E_d, is generated between the upper side of the GEM foil and the cathode, while the induction field, E_I, between the lower side of the GEM foil and the anode (PCB). The relative regions are called drift and induction gaps.

Electron produced by ionization in the drift gap are driven by means of the low E_d towards the GEM holes, where multiplication occurs. Some of the electrons from the multiplication are collected on the lower side of the GEM foil. The fraction of the multiplication electrons

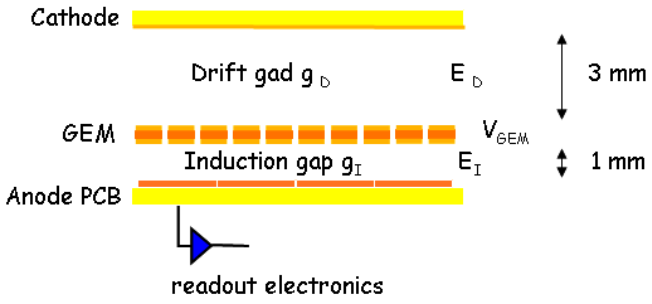

Figure 3.8: Cross section of a single GEM detector: E_D and E_I are the drift and the induction fields, while g_D, g_I are the drift and induction gaps; V_{GEM} is the voltage difference applied to the two copper layers of the GEM foil.

that are transferred in the induction region, gives rise to an induced current signal on the anode. Typically the fraction of multiplied electrons that are transferred in the induction region is $\sim$ 50% and this fraction depends on the electric field inside the hole and electric field below the GEM (Fig. 3.9).
The multiplication ions are mainly collected on the upper side of the GEM foil instead of drifting towards the cathode, leaving the GEM hole from charges in a relatively short time (few μs), thus ensuring this kind of detector a high rate capability.

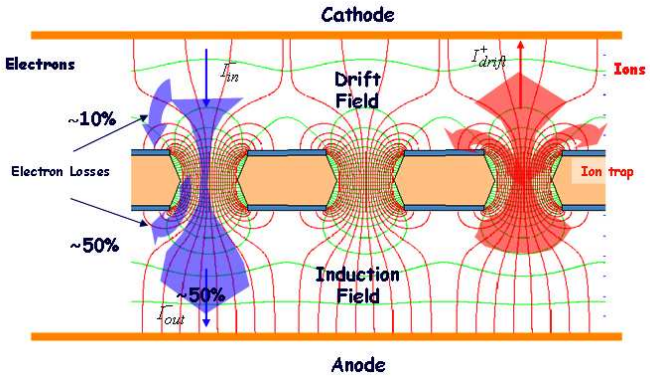

Figure 3.9: Qualitative scheme (not in scale) of a single-GEM detector operation together with the 2D map of electric field lines (red) and equipotential lines (green) in proximity of the GEM holes.

Generally, the read-out is a simple and cheap printed circuit board (PCB): the structure of the readout can be easily adapted to experimental needs, using strips or pads of arbitrary shapes connected to the front-end electronics (Fig. 3.10). Since the read-out is kept at ground potential, considerable simplification of the front-end electronics is also achieved.
As mentioned above, the induced signal is purely due to the motion of the electrons in the induction gap. Taking into account the high electron mobility, the induced signal is fast and not affected by the ion tail typical of the wire chamber [34].

The parameters of a single-GEM detector, with defined GEM foil geometry and gas mixture, are:

- the electric fields in the drift and the induction gap;
- the thickness of the drift and the induction region;
- the voltage difference applied to the GEM foil.

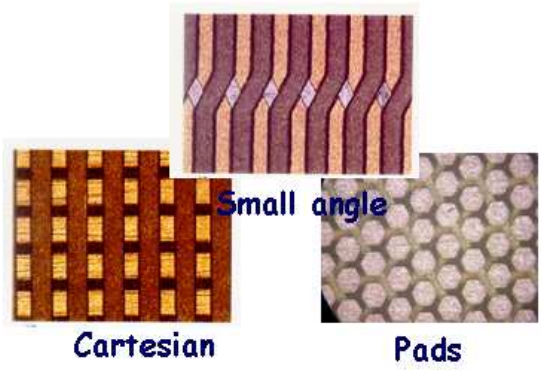

Figure 3.10: Various readouts used with a GEM based detector.

3.3.1 The gap electric fields

Since a GEM detector has a multiple electrode structure, the study of the effects of gap electric fields must be performed measuring the current on all electrodes, to understand where the fraction of current not collected by the readout anode has been lost.
Useful hints are obtained by gas detectors simulation tools, such as MAXWELL [56] [4] and GARFIELD [57] [5]

The drift field

The purpose of the drift field is to collect the primary electrons, produced by the ionization particles in the gap, into the GEM holes. Fig. 3.11 shows a comparison of relative signal amplitude as a function of the drift field, deduced from a measurement of current and from pulse height with two shaping times (100 ns and 1 μs) [55].
At low field values ($<$0.5 kV/cm), the curves drop due to a low electron drift velocity and large diffusion. At intermediate value ($\sim 1 \div 3$ kV/cm), the signals reaches a plateau and decrease again for higher value of drift field. The latter effect is due to the defocusing effect [58] of field-lines above the GEM, which leads the primary electrons to be directly collected on the upper electrode of the GEM.
The above dispersive effects are correlated to the so-called *collection efficiency* which will be discussed in detail in Sec. 3.3.4.

[4] The Maxwell tool is an engineering program. It allows to construct the 3D geometry of a detector, the so called "cell", taking into account all the detector material properties.

[5] The Garfield program is the common framework used for the simulation of gas detectors.

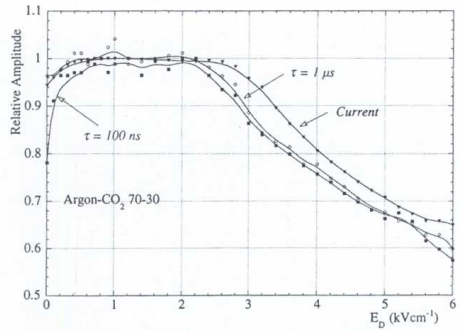

Figure 3.11: Relative signal amplitude on the PCB as a function of the drift field [55].

For a given gas mixture and GEM foil geometry, the value of the drift field is chosen in order to optimize the *collection efficiency*. In Ar/C0$_2$ (70/30) gas mixture the typical value of the drift field is 2 kV/cm [55].

The induction field

The task of the induction field is to extract the multiplied electrons from the GEM holes and to transfer them towards the anode.
Fig 3.12 shows the electron current induced on the bottom electrode of the GEM (I$_B$) and on the pad (I$_S$), together with the sum (I$_{TOT}$), as a function of the induction field [55]. The drift field was set to 1 kV/cm to ensure full *collection efficiency* in GEM holes.

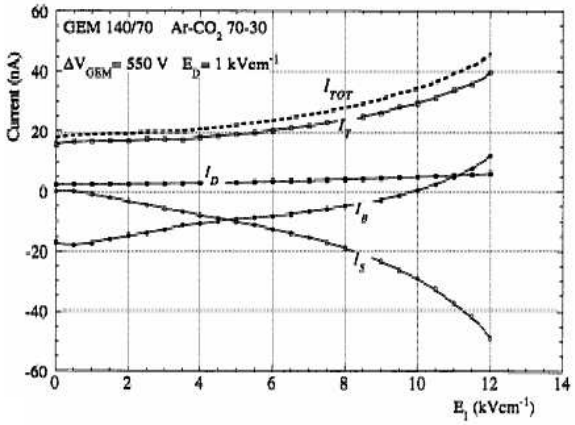

Figure 3.12: Currents on the various electrodes of a single-GEM detector as a function of the induction field: I$_S$ current on the pad, I$_B$ and I$_T$ current on the bottom and upper layer of the GEM, and I$_D$ current of the cathode [55].

At very low value of the induction field all the secondary electrons, extracted from the GEM holes, are practically collected on the bottom GEM electrode and the induced signal is vanishing (Ramo-theorem). By incrementing the induction field, the secondary electrons begin to be collected on the readout electrode, increasing I_S and decreasing I_B.
At very high induction field, $E_I > 8$ kV/cm, discharges on the anode can occur due to the high electric field in proximity of the readout electrode edges.
Independently by the gas mixture used, a value of the induction field of ~ 5 kV/cm is a reasonable compromise and allows to collect a large fraction (50%) of the charge on PCB.

3.3.2 The drift gap thickness

The geometry of this gap has to be chosen in order to ensure a high particle detection efficiency. For a charged track, the number of electrons clusters created has a Poisson distribution with an average value $\overline{n}$ depending on the particle energy and the gas mixture used. For any reasonable choice of the gas mixture, a 3 mm wide gap guarantees the full efficiency of the detector.
A wider drift gap should essentially leave the detector efficiency unchanged, while it can increase the pile-up effects at very high particle rate as well as the ageing rate. In fact, the charge integrated by the detector obviously linearly depends on the value of the primary electrons released in the drift gap.

3.3.3 The induction gap thickness

The induction gap is typically 1 mm thick in order to maximize the signal fraction integrated by the amplifier. As will be discussed in Sec. 3.6, the GEM signal amplitude is proportional to the ratio between the electron drift velocity and the thickness of the induction gap.
This consideration suggests the use of a fast gas mixture as well as a small thickness for the induction gap. However, a sub-millimetric gap is not advised because it would require a high mechanical tolerance in order to avoid discharges on the PCB, and gain disuniformity of detector.

3.3.4 The GEM voltage

The voltage, V_{GEM}, applied to the two metal sides of the GEM foil develops a high electric field inside the holes, and the *intrinsic* gain of the GEM foil directly depends on the V_{GEM}:

$$G_{intrinsic} \propto e^{<\alpha>V_{GEM}} \tag{3.1}$$

where $< \alpha >$ is the average of the first Townsend coefficient [59] along the electron path through the hole. This coefficient is gas mixture and electric field dependent [6].
Generally, the *intrinsic* gain of a single-GEM detector can reach value of the order of 10^3.
As mentioned in the Sec. 3.3.1, there are dispersive effects that decrease the number of the effective electrons transferred on the anode. Consequently, the resulting *effective* gain is smaller than the *intrinsic* one.
These dispersive effects are correlated with the value of the electric fields above and below the GEM and the voltage V_{GEM}.
For a GEM-based detector it is possible to define the following quantities:

1. *collection efficiency* (ϵ^{coll}):

$$\epsilon^{coll} = \frac{electrons\ collected\ in\ the\ holes}{electrons\ produced\ above\ the\ holes} \tag{3.2}$$

   represents the ratio between the number of electrons entering the multiplication channels and the number of primary electrons generated above the GEM.
   The *collection efficiency* is generally a function of the electric field above the GEM and the electric field inside the hole.
   Simulation studies have shown that primary electrons are lost either because they are collected on the upper GEM electrode (defocusing effect [58]) or they hit the kapton surface inside the hole before starting the multiplication (Fig. 3.13, 3.14).

   As already shown in Fig. 3.11, this effect could be in general reduced decreasing the drift field or increasing the electric field inside the hole.
   In case of electronegative gas mixtures, additional primary electrons losses can occur before the multiplication due to the recombination effects. For example, for our gas mixture, $Ar/CO_2/CF_4$ (45/15/40), the electric field in the proximity of the hole ($\sim$ 10

[6] The rigorous formula of the intrinsic gain is: G=exp($\int[\alpha(x) - \eta(x)]\delta$x), where α and η are respectively the first Townsend and the attachment coefficient in the path δx. Both of these coefficients are field and gas mixture dependent. Due to the high value of the field inside the hole (100 kV/cm), the attachment coefficient becomes negligible and the previous formula reaches the Eq. 3.1.

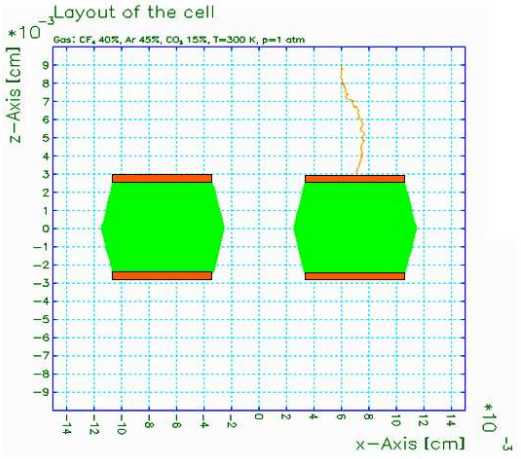

Figure 3.13: Primary electron collection on the upper GEM electrode.

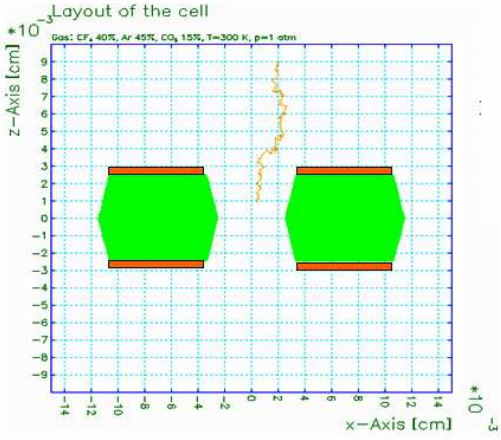

Figure 3.14: Primary electron capture before the multiplication.

kV/cm) can allows for a recombination of the primary electrons due to a high electron attachment with respect to the Townsend coefficient (Fig.3.15).

For the $Ar/CO_2/CF_4$ (45/15/40) gas mixture, the defocusing effect and the capture on the kapton are of the order of 20% and 5% respectively, while the electron attachment is about 10%, giving a global *collection efficiency* of $\sim$ 65%.

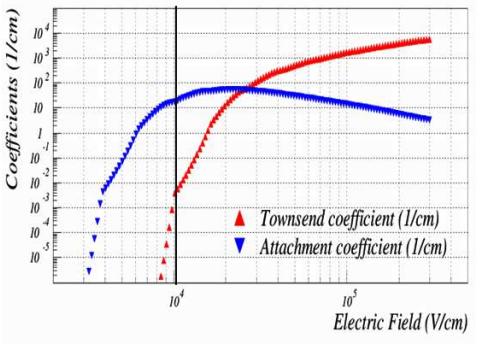

(a) For the Ar/CO_2 (70/30) gas mixture.

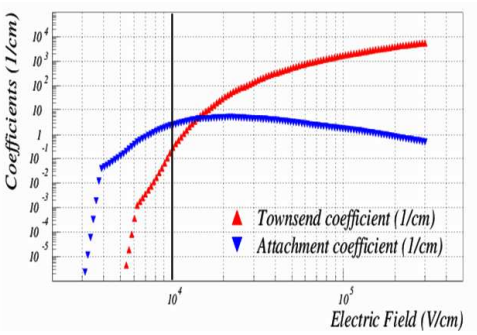

(b) For the $Ar/CO_2/CF_4$(45/15/40) gas mixture.

Figure 3.15: Townsend and electron attachment coefficients as a function of the electric field simulated with Imonte. The black line represents the value of the electric field in proximity of the entrance as well as the exit of the hole.

2. *extraction fraction* (f^{extr}):

$$f^{extr} = \frac{electrons\ extracted\ from\ the\ holes}{electrons\ produced\ in\ the\ holes} \tag{3.3}$$

this quantity represents the ratio between the number of electrons extracted from the holes and transferred to the PCB and the number of electrons multiplied inside the amplification channels.

The extraction fraction is a function of the electric field inside the hole and the electric field below the GEM.

The simulation studies, Fig 3.16, have shown that, in our geometry and fields configuration, $\sim$ 3% of the multiplication electrons are trapped at the hole surface due to the diffusion, $\sim$ 10% are ion captured in proximity of the hole exit. The remaining multiplication electrons, coming out from the hole, are either collected on the bottom electrode of the GEM or transferred to the induction region.

As discussed in the previous section, the induction field is set at 5 kV/cm to assure a safe detector operation. In this case a fraction of $\sim$ 50% of multiplication electrons are lost on the bottom electrode of the GEM foil and the other 50% goes towards the readout electrode. A total *extraction fraction* of about 35% is obtained.

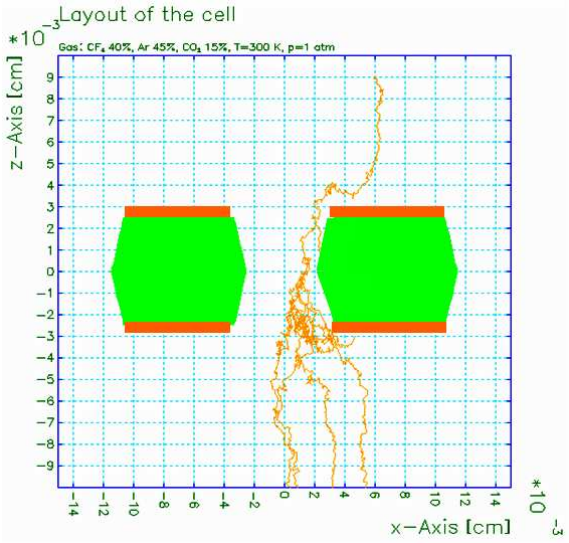

Figure 3.16: The trapping on the kapton surface and the collection on the GEM bottom side of the multiplication electrons.

The definition of the *collection efficiency* and *extraction fraction* allows to introduce the concept of the *effective* gain, G_{eff}, correlated with the *intrinsic* gain of a GEM foil, G_{intr} through the following relation:

$$G_{eff} = G_{intr} \cdot T = G_{intr} \cdot \epsilon^{coll} \cdot f^{extr} \tag{3.4}$$

where we define the *electron transparency* T of the single-GEM detector as the product of $\epsilon^{coll} \cdot f^{extr}$.

The maximum effective gain reachable with a single-GEM detector is of the order of 10^3. Higher gas gain, up to $10^4 \div 10^5$, can be achieved assembling more than one GEM foil in cascade at close distance one to each other.

3.4 The triple-GEM detector

A triple-GEM detector consists of three GEM foils piled-up and sandwiched between two electrodes, a cathode and an anode.
The use of three GEM foils allows to reach higher detector gain before the appearance of discharges (Fig. 3.17), as the gain is divided in three amplification stages; even if the third amplification stage is interested by the same charge of the case of a single GEM detector (operated at the same total gain), such a charge is spread over GEM holes thanks to the diffusion through the previous gaps.

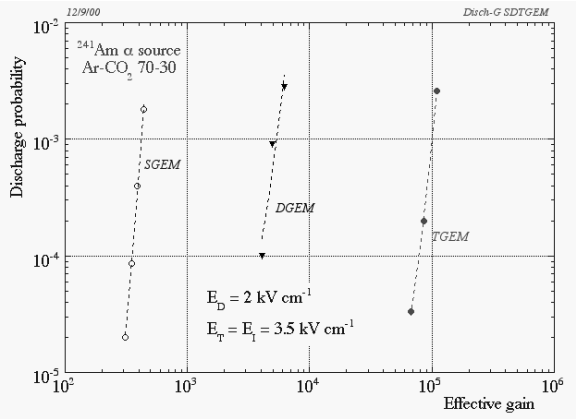

Figure 3.17: Discharge probability as a function of the gas gain for a single, double and triple GEM detectors in Ar/C0$_2$ (70/30) gas mixture [55].

A cross section of a triple-GEM detector, together with the labeling defining the geometrical and electrical parameters, is shown in Fig. 3.18. The voltage difference applied to the various GEM foils are called (from the top to the bottom) V_{GEM1}, V_{GEM2}, V_{GEM3}, and their sum V_{GEM}^{tot}.
The description of the single-GEM chamber, discussed in the previous section, allows to understand the operation of a triple-GEM detector. The gap between the cathode and the first GEM foil acts as conversion and drift region.
The gap between the last GEM foil and the anode is the induction region where, after the multiplication, in this case due to the three GEM foils, the charge induces the signal on the anode PCB.
For the electric fields and geometrical thickness of these gaps, the same considerations done for the single-GEM detector are valid.

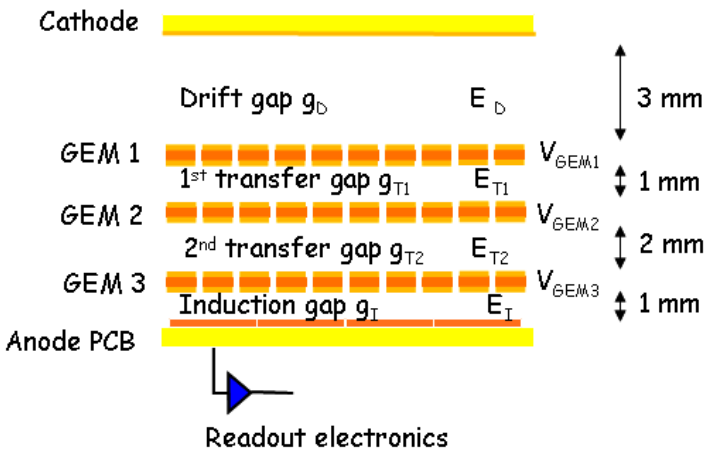

Figure 3.18: Cross section of the triple-GEM detector. E_D, E_{T1}, $E_{T2}$and E_I are the drift, the first and the second transfer and the induction fields respectively; g_D, g_{T1}, g_{T2} and g_I are the drift, the two transfer and the induction gaps respectively.

The other two gaps, between two consecutive GEM foils, are called transfer regions. They act as an induction region if they are referred to the above GEM, while as a drift region if they are referred to the GEM below. Thus the choice of the transfer fields and the relative thickness requires for additional considerations.

3.4.1 The transfer electric field

The purpose of the transfer field is to transport the secondary electrons produced in the holes of the above GEM and to collect them in the holes of the next GEM. This means that the value of the transfer field must be chosen in order to maximize at the same time the *extraction fraction* from the upper GEM and the *collection efficiency* to the lower GEM (Sec. 3.3.4).
Fig. 3.19 shows the induced current on the electrode readout as a function of the transfer fields for the Ar/$C0_2$ (80/20) gas mixture for a given value of drift and induction fields (E_D= 2 kV/cm, E_I= 5 kV/cm).
At low value of the transfer field ($E_T < 3$ kV/cm), the electron current is affected by a low *extraction fraction*. In fact, the multiplication electrons are extracted by the upper GEM holes but they are mainly collected on the bottom electrode of that GEM.
On the other hand, a high transfer field ($E_T > 4$ kV/cm) imply a poor *collection efficiency* due to a high defocusing effect. Indeed, the multiplication electrons, coming from the above GEM, are mainly collected on the upper electrode of the successive GEM.

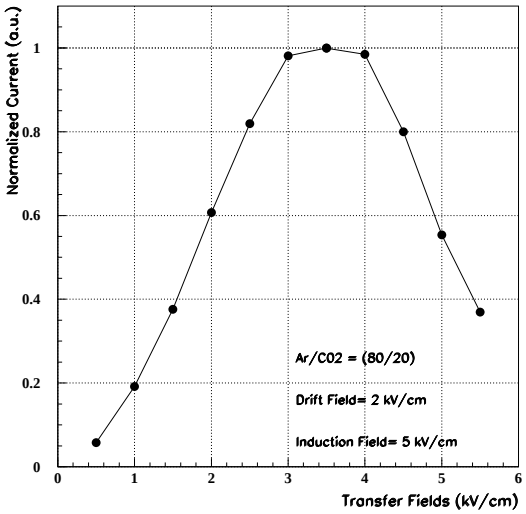

Figure 3.19: Induced current on the readout electrode as a function of the transfer field (E_{T1}=E_{T2}) for the Ar/$C0_2$ (80/20) gas mixture.

For an Ar/$C0_2$ (80/30) gas mixture, a typical value for both transfer fields is in the range of 3÷4 kV/cm.

3.4.2 The transfer gap thickness

In order to improve the time performance of the detector and to keep the discharge probability as low as possible, several tests were performed for different size of the transfer gaps, using the following detector geometry (g_D/g_{T1}/g_{T2}/g_I): 3/2/2/1, 3/1/2/1 and 3/1/1/1.
The results of these tests are discussed in the next sections.

The first transfer gap

As a charged particle crosses the detector, the gas ionization occurs in each gaps of the detector. The main difference between the primary electrons produced in the various gaps is the number of multiplication steps that they undergo along their drift towards the anode: the electrons produced in the drift gap pass through the three multiplication steps, while those generated in the first transfer gap cross only two GEM foils.
Due to statistical fluctuations of the total ionization and the gas gain, the ionization produced in the first transfer gap, and multiplied by the last two GEM, can induce a signal large enough

to be discriminated by the front-end electronics. This signal, depending on the drift velocity of the gas mixture and the gap thickness, will be anticipated, with respect to the signal produced by the electron coming from the drift gap, of the quantity $\Delta t = g_t/v_{drift}$.
This effect, particularly important for the time performance of the detector, has been called *bi-GEM effect* [60].
Fig. 3.20 shows the time spectrum obtained with the $Ar/C0_2/CF_4$ (60/20/20) gas mixture for 1 and 2 mm first transfer gap thickness.

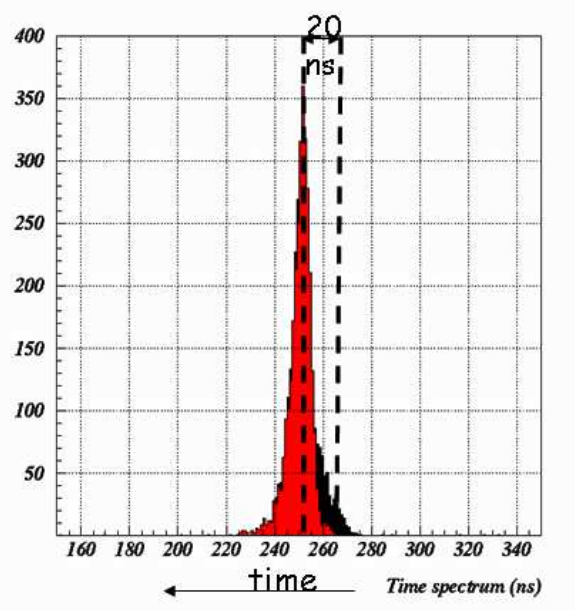

Figure 3.20: Time spectrum of a GEM detector with 1 mm (red) or 2 mm (black) thick first transfer gap. The black distribution is broader because of anticipated signals originated by the ionization of first transfer gap (*bi-GEM effect*).

For an electric field of 3 kV/cm, the electron drift velocity of this gas mixture is about 10 cm/μs. With a 2 mm gap (black distribution), the time spectrum is characterized by the presence of small amplitude events in advance of $\sim$ 20 ns with respect to the main signal, broadening the distribution. A 5% of the total number of events are represented by *bi-GEM* events.
Vice versa with a 1 mm thickness (red distribution) the anticipated signals, in this case in advance of $\sim$ 10 ns with respect to the main signal, are practically disappeared, being included in the global fluctuations of the arrival time of the electrons. In this case, the *bi-GEM* events are less than 2% of the total.

This result suggests that the thickness of the first transfer gap has to be keep as low as possible. We set the value of g_{T1} to 1 mm.
A further reduction of the *bi-GEM* effect could be achieved by increasing the amplification on the first GEM, as will be discussed in Sec. 3.4.3.

The second transfer gap

In the second transfer gap the effects of small amplitude and anticipated signals are vanishing. In fact, the primary electrons produced in this gap are multiplied only by the last GEM, thus they can very rarely give rise to a signal over the electronic threshold.
On the other hand, the thickness of this gap is correlated with the discharge probability. As will be discussed in Sec. 3.7.4, the number of electron-ion pairs could exceed the Raether limit (transition from avalanche to streamer) in the third amplification step (GEM3), and a discharge can develop inside the hole.
For all gas detectors, the discharge effect can be minimized by adding a suitable fraction of a quencher component to the gas mixture, although the quantity and the type are limited by the long-term degradation of the detector performance due to ageing processes.
For a triple-GEM detector using a given gas mixture, the discharge effect can be reduced by increasing the thickness of the second transfer gap. Indeed, a larger gap allows to increase the electron diffusion in that region. Since the transverse dimension of the electron clouds increases with the square root of the electron drift [34], the number of the holes involved in the multiplication process increase linearly with the thickness of a gap. Consequently, the diffusion allows the electron cloud to be spread over more than a single hole, reducing the probability of reaching the Raether limit in the third GEM (Fig. 3.21).
The measure of the discharge probability, as a function of the gas gain in the $Ar/C0_2/CF_4$ (60/20/20) gas mixtures, for two different thickness of the second transfer gap, 1 and 2 mm respectively, has been performed with an ^{241}Am (α) source [61].
As shown in Fig. 3.22, the discharge probability for a 2 mm gap (red curve) is a factor of 2 less than that one obtained with a 1 mm gap (black curve), for a gas gain of 4.5×10^4.
Taking into account the maximum size required by the muon system for the whole detector thickness and at the same time the necessity to minimize the discharge effect, we set the value of the second transfer gap to 2 mm.

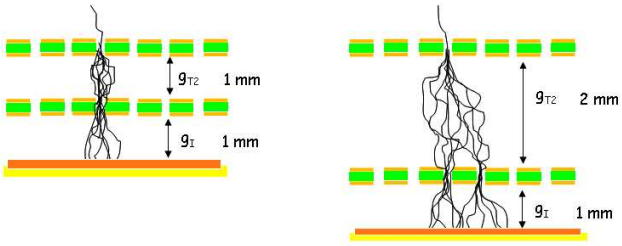

Figure 3.21: Qualitative schema of diffusion effect for different size of the transfer gap.

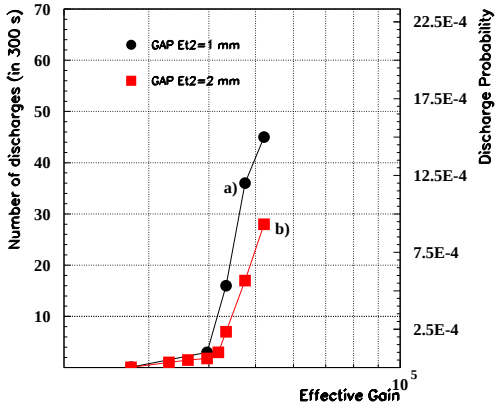

Figure 3.22: The discharge probability, performed with an ^{241}Am source, as a function of the gas gain in the Ar/C0$_2$/CF$_4$ (60/20/20) gas mixtures for 2 different thickness of the second transfer gap, 1 and 2 mm.

3.4.3 The GEM voltages

For a triple-GEM detector the *intrinsic* gain is an exponential function of V_{GEM}^{tot}.
Together with the electric field in the various gaps, that define the *electron transparency* T_{tot}, the *effective* gain of the detector is defined as follows:

$$G_{eff} = G_{intr} \cdot T_{tot} = \prod_{k=1}^{3} e^{<\alpha>_k \cdot V_{GEMk}} \cdot T_k = e^{<\alpha>^{tot} \cdot V_{GEM}^{tot}} \cdot \prod_{k=1}^{3} \epsilon_k^{coll} \cdot f_k^{extr} \qquad (3.5)$$

where the $< \alpha >$ is the average of the first Townsend coefficient [59] of the electron path through the hole, ϵ_k^{coll} and f_k^{extr} are the *collection efficiency* and the *extraction fraction* of the k^{th} GEM foil.

Since the effective gain depends on the voltage applied the three GEMs only through their sum, it is possible to unbalance these voltage differences in order to reduce the discharge effect in the last GEM. Indeed, at a fixed V_{GEM}^{tot}, i.e. at a fixed gain, it is convenient to increase the voltage applied on the first GEM while reducing the one applied to third GEM. In this case, the charge reached on the third GEM is greater but the diffusion effect allows the electron cloud to be spread over a larger number of holes, reducing the discharge probability. The studies with the α source enable us to choose the GEM configuration that minimizes the

discharge probability. The optimal configuration of the GEM voltages is [62]:

$$V_{GEM1} \gg V_{GEM2} \geq V_{GEM3} \tag{3.6}$$

This GEM voltage configuration, reducing the discharge effect, allows also to improve the detector time performance due to a decrease of the *bi-GEM* effect (Sec. 3.4.2). In fact, the incidental primary electrons produced along the first transfer gap will be multiplied with a lower gain with respect to the case in which the GEM voltage configuration is not unbalanced. The above GEM voltage configuration, together with 1 mm thick first transfer gap, allow to reduce the *bi-GEM* effect down to 1%. Finally, the *collection efficiency* on the first GEM is also slightly increased due to a reduction of the defocusing effect.

3.5 The time performance

The main request for triggering in LHCb Muon system is to provide a high efficiency in the bunch crossing time window. Hence, besides high overall efficiency, the triple-GEM detector should ensure good time performance.

The time performance of a GEM-based detector is correlated with the statistics of the clusters [7] produced in the drift gap.
The general expression for the space-distribution of the cluster j created at distance x from the first GEM, is [34]:

$$A_j^{\overline{n}}(x) = \frac{x^{j-1}}{(j-1)!}\overline{n}^j e^{-\overline{n}x} \tag{3.7}$$

where $\overline{n}$ is the average number of clusters created per unit length. For a given drift velocity in the drift gap, v_d, the probability-distribution of the arrival times on the first GEM for the cluster j gives:

$$P_j(t_d) = A_j^{\overline{n}}(v_d t_d) \tag{3.8}$$

Specifically for the first cluster produced closest to the first GEM (j = 1):

$$P_1(t_d) = \overline{n} \cdot e^{-\overline{n} v_d t_d} \quad \Rightarrow \quad \sigma_1(t_d) = \frac{1}{\overline{n} \cdot v_d} \tag{3.9}$$

The latter gives the *intrinsic* value for the time resolution of the detector if the first cluster is always detected.
A high primary ionization ($\overline{n}$) and a fast (v_d) gas mixture should be chosen in order to improve the time performance of a GEM detector.
A preliminary simulation study of the gas mixture properties [63] has been done by using the following simulation tools:

- *Magboltz*, which computes the electron drift velocity, the longitudinal and the transverse diffusion coefficients of a gas mixture;
- *Heed*, which calculates the energy loss through the ionization of a particle crossing the gas and allows to simulate the cluster production process;
- *Imonte*, which computes the Townsend and attachment coefficients;

[7] In general, the number of clusters produced in the drift region is correlated to the type of incident particle (α, γ, π, proton), to its energy and the gas mixture used as converter.

Using the *Magboltz* simulation tool, the electron drift velocity as function of the drift field for various gas mixtures tested had been estimated (Fig. 3.23). The curve of the Ar/CO_2 (70/30) gas mixtures, commonly used by other authors is also reported.

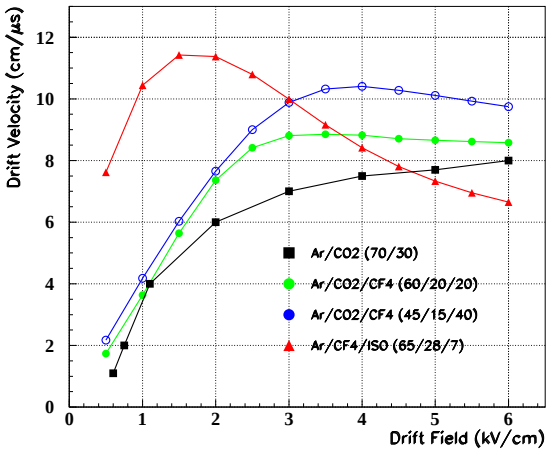

Figure 3.23: Simulated electron drift velocity for the studied gas mixtures. The curve of the Ar/CO_2 (70/30) is reported for comparison.

The $Ar/CO_2/CF_4$ (45/15/40) and the Ar/CF_4/iso-C_4H_{10} (65/28/7) reach the highest drift velocity, $\sim$11cm/μs, for 3.5 and 2 kV/cm drift field, respectively.
The *intrinsic* time resolution, which depends on the inverse of the product of the drift velocity and the specific primary ionization in the drift gap had been evaluated using *Magboltz* and *Heed* simulation tools.
Tab. 3.1 summarizes the properties of the gas mixtures together with the *intrinsic* time resolution, while in Fig. 3.24 is shown the *intrinsic* time resolution as a function of the drift field.

Gas Mixture	Drift velocity (drift field)	$<$ Clusters/mm $>$	Intrinsic time resolution
Ar/CO_2 (70/30)	7 cm/μs (@3 kV/cm)	3.3	4.7 ns (@3 kV/cm)
$Ar/CO_2/CF_4$ (60/20/20)	9 cm/μs (@3 kV/cm)	5	2.3 ns (@3 kV/cm)
$Ar/CO_2/CF_4$ (45/15/40)	10.5cm/μs (@3.5 kV/cm)	5.5	1.7 ns (@3.5 kV/cm)
Ar/CF_4/iso-C_4H_{10} (65/28/7)	11.5 cm/μs (@2kV/cm)	5.7	1.5 ns (@2 kV/cm)

Table 3.1: Summary table of the gas mixture properties: the optimized drift velocity, and the average cluster yield, the *intrinsic* time resolution.

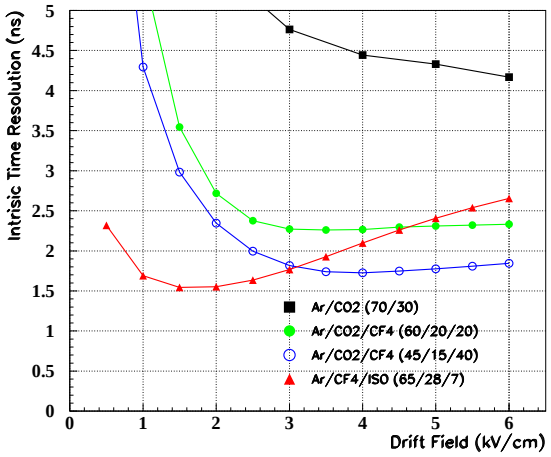

Figure 3.24: The *intrinsic* time resolution of a triple-GEM detector as a function of the drift field. The curve of the Ar/CO_2 (70/30) is also reported as comparison.

The result of this simulation study is that the best *intrinsic* time performance is achieved with the $Ar/CO_2/CF_4$ (45/15/40) and the Ar/CF_4/iso-C_4H_{10} (65/28/7) gas mixtures.

It should be stressed that the *intrinsic* time resolution represents a lower limit. In fact, taking into account the limited *collection efficiency* of the first GEM (Sec. 3.3.4), the statistical fluctuation of the gas gain [66] and the finite threshold of the electronics, it could happen that the signal induced by the first cluster cannot be discriminated. In this case the successive pile-up of clusters is needed to have a signal above the electronic threshold. This effect is the main limitation of the detector time resolution.
In order to avoid or to reduce this effect, it is necessary to increase the single electron detection capability. The use of a fast gas mixture, characterized by a high drift velocity at a relative low value of drift field, which ensures a large *collection efficiency* in the first multiplication stage, gives a high detection efficiency of the first cluster.

3.6 The signal formation

In GEM detector the signal is completely induced by the electron motion in the induction gap. As the first electron emerges from the last GEM, it starts to induce a current on the pads which stops when it is collected.
The current I_k induced on the electrode k, due to a moving charge q and velocity v_d, can be calculated using the Ramo's theorem [65]:

$$I_k = -\frac{q\overrightarrow{v_d}(x) \times \overrightarrow{E}_k(x)}{V_k} \tag{3.10}$$

where $\overrightarrow{E}_K(x)$ is the electric field created by raising the electrode k to the potential V_k.
If V_k= 1 V and all the other pads are connected to ground, Ramo's theorem becomes:

$$I_k = -q\overrightarrow{v}(x) \times \overrightarrow{E}_k^w(x) \tag{3.11}$$

where $\overrightarrow{E}_k^w(x)$ is called the *weighting field*.
The $\overrightarrow{E}_k^w(x)$ behavior has been simulated [63] and it results to be practically constant in the induction gap meaning the electron drift velocity is constant too.
It is expected that each electron emerging from the last GEM induces a rectangular current signal in the nearest pad with a width dependent on the time spent by the electron to cross the induction gap:

$$i = -\frac{q}{t} = -\frac{qv_d}{x} \tag{3.12}$$

where x is the thickness of the induction gap and v_d is the electron velocity in that gap.
The expression points out that, for each given charge produced by a certain primary ionization and detector gain, higher induced signals can been achieved by reducing the thickness of the induction gap and using a fast gas mixture, or a high induction field (in the limit of safe operation).

3.7 The R&D activity on triple-GEM detector

To fulfill the M1R1 requirements of the LHCb experiment and to assure a safe operation mode in such a harsh environment, we proposed to adoption of a triple-GEM detector.
The use of this type of detector as a triggering device is certainly a novelty, since GEM detectors was born as tracking device, with little interest to the optimization of the time performance. But for LHCb muon trigger, a critical issue is the high efficiency in the bunch-crossing identification, which implies a high time resolution.
Because the typical GEM detector time resolution with an Ar/CO_2 (70/30) gas mixture is about 10 ns r.m.s [50], an intense R&D activity has been performed by our group at Laboratori Nazionali di Frascati (LFN) and the Cagliari section of the Istituto Nazionale di Fisica Nucleare (Ca-INFN), on new fast gas mixtures, based on CF_4 and isobutane, in order to improve this limit.
These new gas mixtures have also required the study the long term capability of this technology to tolerate 10 years of LHCb operation without damages or performance losses.
For this R&D activity small size prototype have been used, where the geometrical configuration can be easily changed and adapted to the specific test to be performed. These prototype have been realized with three GEM foils (10×10 cm^2 active area) previously stretched with a home-made tool in order to avoid electrostatic instability (see Sec. 4.3.1) and glued on fiberglass (FR4) frames. The anode readout is segmented in 6×16 mm^2 pads. The cathode has made up of a kapton foil, with copper on one side, glued on a similar frame. All frames have then fixed inside a FR4 gas-tight box (Fig. 3.25).
The pads have been connected to a fast preamplifier based on VTX-chip with a sensitivity of 10 mV/fC, peaking time of 5 ns and electronic noise charge of about 1300e$^-$ r.m.s at zero input capacitance. The VTX chip, supplying an analog output, resulted to be particularly suitable in this R&D phase.
More details of the prototype chamber construction and the VTX readout can be found in [61].

In the Sec. 3.7.1 and Sec. 3.7.2 the effective gain and the rate capability measurement are respectively discussed.
The results obtained with the fast CF_4 and isobutane based gas mixtures will be discussed in Sec. 3.7.3 and 3.7.3 respectively in term of time resolution and efficiency (in 20 ns time

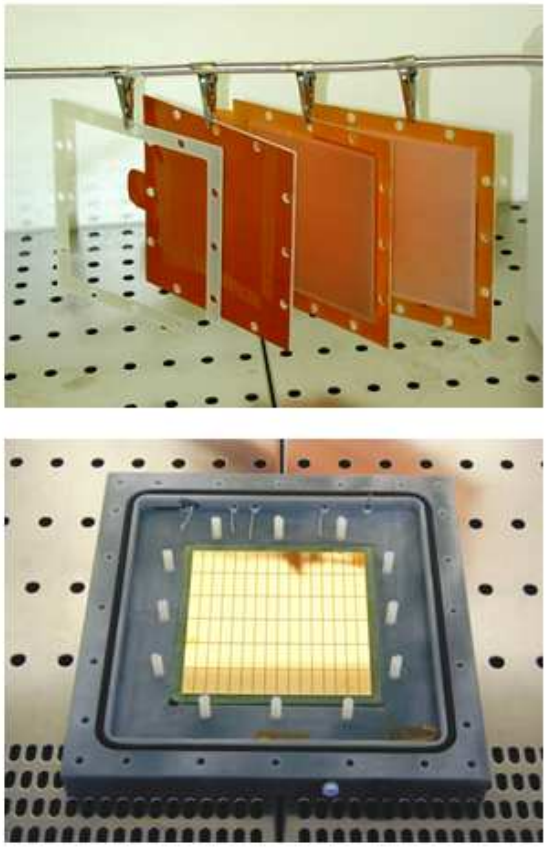

(a) Top: The three GEMs glued on the FR4 frames of different thickness; Bottom: the readout pads mounted on the FR4 box.

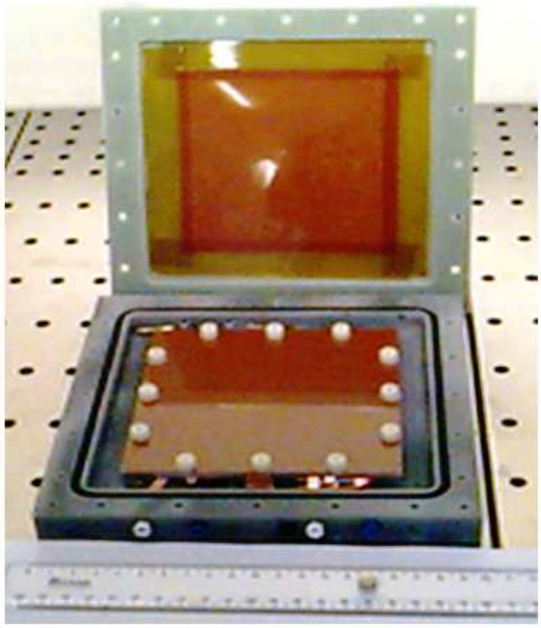

(b) The three GEMs stacked in the FR4 box.

Figure 3.25: The 10×10 cm^2 triple-GEM prototype.

window), while the effects of such gas mixtures on the discharge and ageing effects will be shown in Sec. 3.7.4 and Sec. 3.7.5 respectively.

3.7.1 Effective gain measurement

As already discussed in Sec. 3.4.3, the effective gain of a triple-GEM detector is related to V_{GEM}^{tot} and the first Townsend coefficient [59] as follows:

$$G_{eff} \propto e^{<\alpha>V_{GEM}^{tot}} \tag{3.13}$$

The gas gain measurement has been performed by irradiating a triple-GEM prototype with a high intensity 6 keV X-ray tube.
The current induced on the pad I_{PAD}, for a given X-ray flux Φ_{RX} and irradiating area S, is proportional to the detector gain G, through the relation:

$$I_{PAD} = e \cdot N_{\gamma} \cdot S \cdot \Phi_{RX} \cdot G \tag{3.14}$$

where e is the electron charge and N_{γ} is the gas ionization produced by an X-ray photon, that depends weakly on the gas mixture ($\approx$ 200 electron-ion pair).

Taking into account the different cross sections of the photon conversion in the various gas mixtures, the rate of converted photon, $S \cdot \Phi_{RX}$, has been preliminary measured connecting the pads to the readout electronics. Fig. 26(a) shows the measured particle rate on the pads as function of V_{GEM}^{tot} for the gas mixtures tested. The counts have been recorded with a scaler at the discriminator output, with a discriminator threshold set to 70 mV well above the electronic noise.
Successively, the readout electronics has been removed and the induced current on the readout pads has been measured. Fig. 26(b) shows the effective gain of the detector as a function of V_{GEM}^{tot} for the various gas mixtures tested and for the Ar/CO_2 (70/30) gas mixture, commonly used by other authors.
From the exponential fit, the average Townsend coefficient for the different gas mixtures tested has been determined (Tab. 3.2).

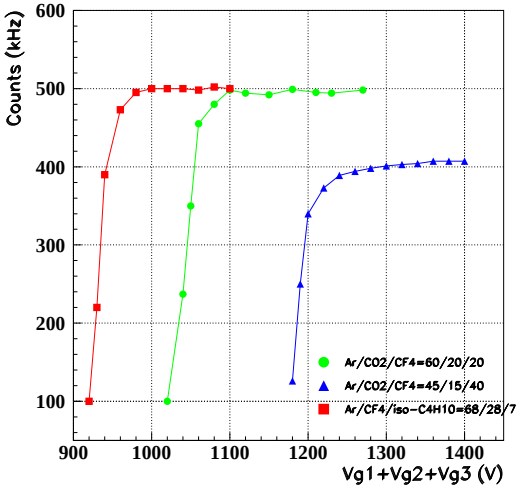

(a) Effective particle rate as a function of V_{GEM}^{tot} for various gas mixtures. The different height of the plateau is due to the different cross sections of the photon conversion in the gas mixture.

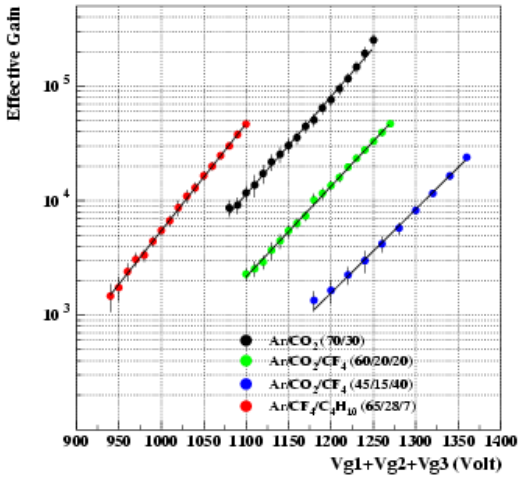

(b) Effective gain of a triple-GEM detector as a function of V_{GEM}^{tot} for the various gas mixtures tested.

Figure 3.26: Effective gain measurements.

Gas mixture	$< \alpha >$ (V^{-1})
Ar/C0$_2$ (70/30)	19.6×10^{-3}
Ar/C0$_2$/CF$_4$ (60/20/20)	18.2×10^{-3}
Ar/C0$_2$/CF$_4$ (45/15/40)	16.9×10^{-3}
Ar/CF$_4$/iso-C$_4$H$_{10}$ (65/28/7)	21.5×10^{-3}

Table 3.2: Results of the exponential fit of the Townsend coefficient along the multiplication path for the various gas mixtures tested.

3.7.2 Rate capability

The rate capability of a detector depends on the time required by the ions to move from the avalanche region to the ion collection electrode. In a GEM structure the ions produced inside the hole are mainly collected on the upper electrode of the GEM itself in a time of the order of few μs.

The detector rate capability has been measured with the $Ar/CO_2/CF_4$ (60/20/20) gas mixture at the gas gain of 2×10^4. A good gain stability was observed up to a particle rate of 60 MHz/cm^2 (Fig. 3.27), demonstrating a very high rate capability of the detector (this measurements was only limited by the maximum flux of our X-ray tube) that is well above the LHCb requirement.

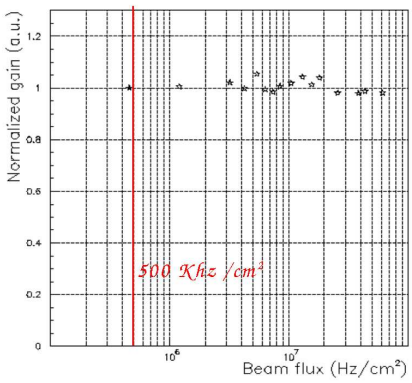

Figure 3.27: Rate capability measurement of a triple-GEM detector: normalized gain as a function of the X-ray flux. The gain stability shows a very good rate capability and is well above the LHCb requirement (500 kHz/cm^2).

3.7.3 Time and efficiency performances

Several tests have been performed at the T11 beam facility of PS-CERN with a π beam of 3$\div$4 GeV/c. These tests allowed us to measure the time performance and the efficiency in 20 ns time window of the detector operated with the new gas mixtures, for optimized geometry and electric field configurations.

The time performance

As discussed in Sec. 3.5, the time performance of a GEM-based detector are correlated with the gas mixture properties. In particular, it has been shown that good time resolution can be achieved using fast and high primary ionization gas mixtures.
A comparison of the time distribution for the considered gas mixtures is shown in Fig. 3.28 [67]. The configuration of the various electric fields which optimize the *collection efficiency* and time performance for the different gas mixtures are summarized in Tab. 3.3.

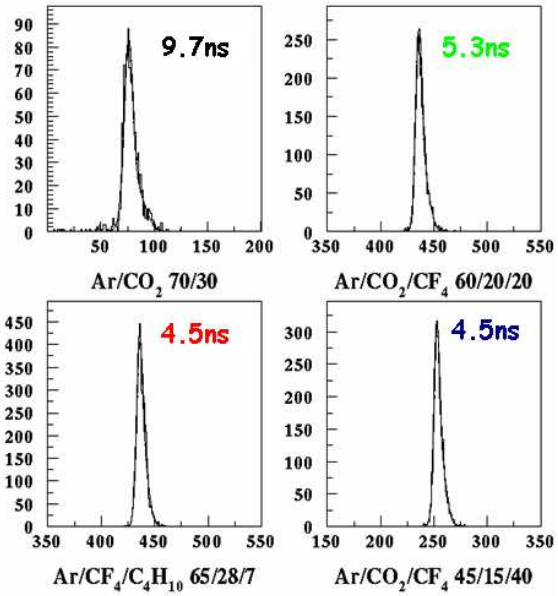

Figure 3.28: The best time distribution for single detector obtained at PS beam facility of CERN [67]. The relative gas gain was: 1×10^5 for the Ar/CO_2 (70/30); 3×10^4 for the $Ar/CO_2/CF_4$ (60/20/20); 1×10^4 for the $Ar/CO_2/CF_4$ (45/15/40); 2×10^4 for the Ar/CF_4/iso-C_4H_{10} (65/28/7).

Gas mixture	E_D (kV/cm)	E_{T1} (kV/cm)	E_{T2} (kV/cm)	E_I (kV/cm)
Ar/CO_2 (70/30)	3.0	3.0	3.0	5.0
$Ar/CO_2/CF_4$ (60/20/20)	3.0	3.5	3.5	5.0
$Ar/CO_2/CF_4$ (45/15/40)	3.5	3.5	3.5	5.0
Ar/CF_4/iso-C_4H_{10} (65/28/7)	2.0	3.0	3.0	5.0

Table 3.3: The electric field configuration used during the tests of the new gas mixtures.

As expected from the simulation, a considerable improvement with respect to the Ar/CO_2 (70/30) gas mixture ($\sim$ 10 ns of r.m.s) is obtained with the iso-C_4H_{10} and CF_4 based gas

mixtures, reaching time resolutions better than 5 ns (r.m.s.).

The time resolution (r.m.s.) of a single chamber as function of the gas gain is shown in Fig. 3.29. As expected, an obvious improvement of the time performance is observed increasing the detector gain.
Fig. 3.30 shows the time resolution measurement for two detectors logically OR-ed, to emulate the LHCb station composed by two triple-GEM detectors.

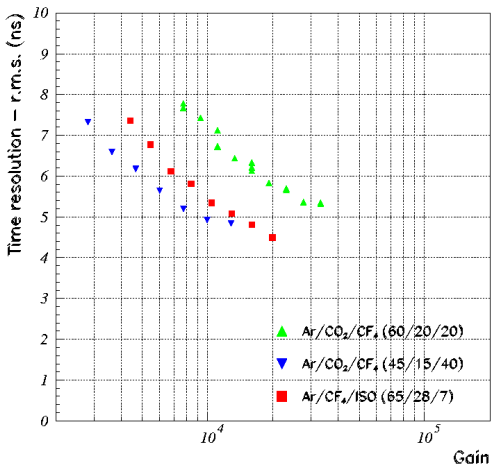

Figure 3.29: Time resolution (r.m.s) as a function of the gas gain for a single detector.

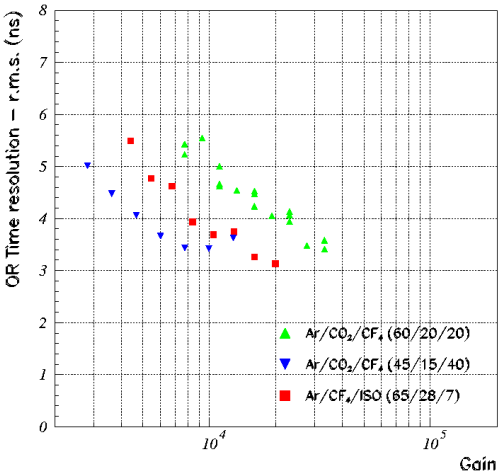

Figure 3.30: Time resolution (r.m.s) as a function of the gas gain for two detectors logically OR-ed.

The efficiency in 20 ns time window

In order to trigger muons produced in consecutive bunch-crossing, a triple-GEM station, i.e two detectors logically OR-ed, should have an efficiency in 20 ns time window higher than 96%.

Fig. 3.31 shows the efficiency in a 20 ns time window as a function of the effective gain for a single detector. As expected the slow and the low primary ionization Ar/CO_2 (70/30) gas mixture does not fulfill the above requirement, even at very high gas gain ($\epsilon_{20} < 85\%$).
Vice versa, the use of iso-C_4H_{10} and CF_4 based gas mixtures, allows to reach efficiency in 20 ns time window larger than 96% at moderate gas gain.
The configuration of the electric fields for the various gas mixtures is the same as that re-

ported in Tab. 3.3.

Fig. 3.32 shows the efficiency within 20 ns time window for two detectors logically OR-ed. Besides a better time performance, the use of two detectors for station provides also some redundancy.

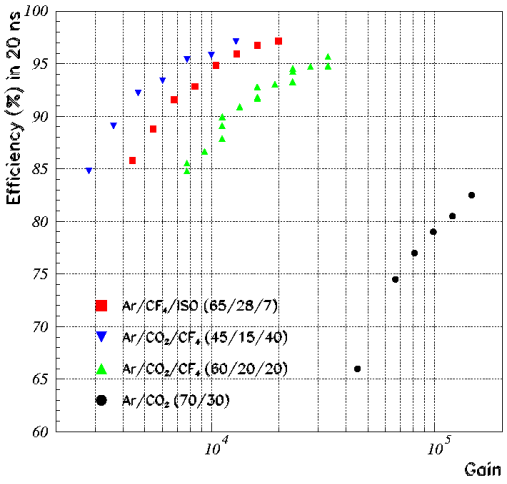

Figure 3.31: Efficiency in 20 ns time window as a function of the gas gain for a single detector. The Ar/CO_2 (70/30) gas mixture is also reported as a comparison.

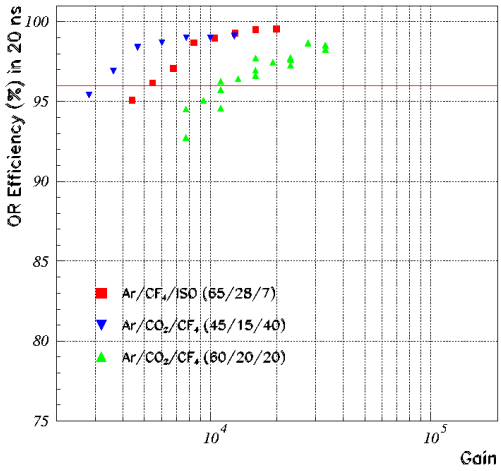

Figure 3.32: Efficiency in 20 ns time window as a function of the gas gain for two detectors logically OR-ed.

3.7.4 The discharge process

The occurrence of discharges in a gas detector is correlated to the transition from avalanche to streamer regime [68] during the multiplication process. This transition is gain and primary ionization density dependent. Indeed, for a given ionizing radiation, the increase of the applied voltage above a certain threshold value, results in a propagating streamer. The threshold value for the transition from avalanche to streamer depends on the type of the ionizing radiation, being lower for highly ionizing particles. The voltage threshold is correlated to the reaching of the Reather limit, that is when the avalanche size exceeds $10^7 \div 10^8$ ion-electron pairs [69],[70].

In GEM detectors, and more generally in micro-pattern detectors, due to the very small distance between anode and cathode, the formation of the streamer can be easily followed by

a discharge. The discharge acts as a short circuit between the two copper sides of the GEM foil discharging in a short time the whole charge stored in the GEM. This phenomenon represents one of the most important problems of damage in micro-pattern detectors.
In a triple-GEM detector the discharge probability is in general lower than for other micro-pattern detectors. This is due to the fact at a fixed gas gain a triple-GEM detector has the advantage to share the total gain on the three GEM foils.
In particular, for triple-GEM detectors the discharge probability is larger in the third GEM where the charge density is higher. As discussed in Sec. 3.4.2, a 2 mm 2^{nd} transfer gap helps to reduce the discharge probability.

Discharge studies have been performed at the πM1 beam facility at Paul Sherrer Institute (P.S.I.) of Zurigo. The detector prototypes were irradiated with a low energy hadron flux with an intensity of up to 300 MHz on about $\sim$ 15 cm^2 of the detector active area. The beam is a quasi continuous beam with 19 ns time separation between two particle bunches. In our experimental area, the beam was composed of 300 MeV/c pions with an estimated contamination of 7% of protons. Low momenta particles produce more primary ionization than m.i.p., thus enhancing discharge probability in order to have a more conservative test.

The discharge probability is defined as the ratio between the observed frequency of discharges and the incident particle rate. The measurement was performed by monitoring and acquiring the currents drawn by the various GEM electrodes. We counted discharges by detecting the current spikes on the pads, corresponding to the OR of the discharges on the three GEM foils.
In Fig. 3.33 the discharge probability per incident particle is reported as a function of the gas gain for the three gas mixtures. The presence of the isobutane allows to sensibly reduce the discharge probability even at very high gain. This result is due to the high isobutane cross section of photon absorption in the range of 1 and 10 eV that limits the streamer propagation. During the PSI test each detector integrated, without any damages or ageing effect, about 5000 discharges on 15 cm^2, i.e $\sim$ 330 discharges/cm^2.
Taking into account the average charged particle rate expected in LHCb (Φ_{LHCb}=184 kHz/cm^2), the maximum discharge probability ($P_{LHCb}^{discharge}$) to integrate 330 discharges/cm^2 in 10 years

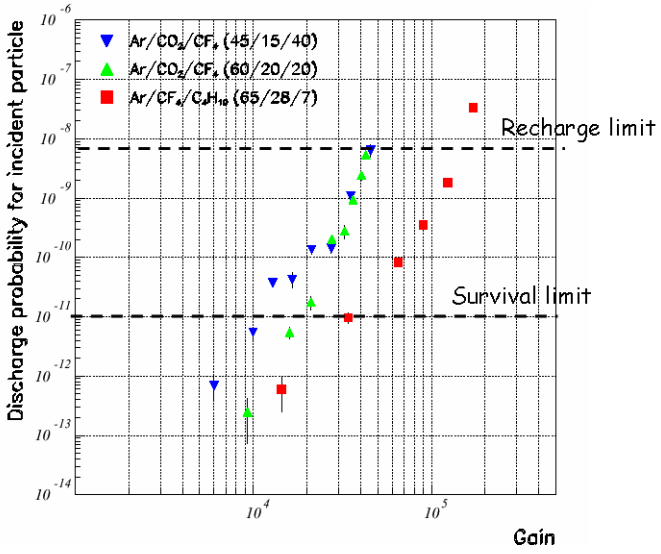

Figure 3.33: Discharge probability per incident particle as a function of the effective gain for a detector with 3/1/2/1 gap geometry.

(Δt_{LHCb} = 10^8 s) of LHCb running could be calculated as follows:

$$P_{LHCb}^{discharge} = \frac{integrated\ \ discharges\ \ per\ \ cm^2}{\Phi_{LHCb} \cdot \Delta t_{LHCb}} \simeq 10^{-11}$$

The estimated maximum discharge probability, which represents a survival limit for discharges, corresponds to a gas gain of about 1.2×10^4, 2×10^4, 4×10^4 respectively for the $Ar/CO_2/CF_4$ (45/14/40), $Ar/CO_2/CF_4$ (60/20/20) and Ar/CF_4/iso (65/28/7) gas mixtures.

To be more precise, it would be necessary to take into account also the dead time produced by discharges. Since the capacitance of a GEM sector is $\sim$ 10 nF and the limiting resistor is 1 MΩ, the recharging time of a GEM sector (S_{sector}= 80 cm^2 see Cap. 4) in which the chamber results inefficient is $\sim$ 10 ms .
To keep this inefficiency below 0.1%, the maximum tolerable discharge probability comes

out to be:

$$\begin{aligned} P_{LHCb}^{discharge} &< \frac{0.1\%\ inefficiency}{\Phi_{LHCb} \cdot S_{sector} \cdot t_{recharge}} \\ &< 6.8 \times 10^{-9} \end{aligned}$$

Therefore, such a limit due to the recharging is less stringent than the above mentioned survival limit.

It should be stressed that the survival limit measured at PSI was conservative because all detectors were still working after the test.
For this reason, we performed a further destructive test to determine the maximum number of discharges that the detector can stand before breakdown. This test was performed in laboratory with an ^{238}Am source. The irradiated area was 0.5 cm^2 and the detector was operated with the Ar/CO_2/CF_4 (45/14/40) at a gas gain of 4×10^4, much higher than the one foreseen for the operation in the experiment (6×10^3). The test was repeated three times and the detectors died after 500, 700 and 800 discharges. Taking the first of the three numbers, assuming the average charged particle rate expected in LHCb and 10 years of running, a maximum discharge probability of 5.4×10^{-11} per incident particle was calculated; from this number and from the results of Fig. 3.33, a maximum gas gain of about 1.8×10^4 for the Ar/CO_2/CF_4 (45/14/40) is obtained.
Since the detector damage due to a discharge across a GEM hole is correlated with the energy stored in the GEM, which scales with the power of two of the applied voltage ($\mathcal{E}$= 1/2 CV^2), and since the detector was irradiated with highly ionizing particles, also this result must be considered quite conservative.

3.7.5 The ageing process

Since the first developments of gaseous detectors, it has been common to find problems associated with long exposure to radiation, that limits their lifetime.
The observed phenomenology included the appearance of local and permanent damages detected as self-sustained discharges, excessive currents, gradual loss of performances (energy resolution, decrease and non-uniformity of the gas gain).
These ageing phenomena are correlated with the formation of polymeric layers on the detector electrodes, possibly induced by pollution released by materials used in the gas system or chamber construction, or impurities in the gas itself [71].
The chemistry of the ageing process has not been deeply studied yet, thus the approach to the ageing problem is still in most cases purely experimental.
It should be stressed that ageing test should be performed as close as possible to the real conditions. Consequently, the irradiated area of the detector should be as large as possible while the detector should be operated with a gas flow and radiation flux which are comparable to the ones foreseen in the experiment. Of course for time constrains such tests must be accelerated, using a radiation flux several times higher than required one, sometimes affecting the reliability of the results.

Considering the average charged particle rate expected at LHCb on the whole detector area and a gas gain of $\sim 10^4$, a current of about 8 μA is expected on the readout pads.
In this section preliminary aging tests, performed irradiating a small area of the detector, are discussed. This measurement allows to test the long-term radiation compatibility of the different gas mixtures with the GEM foil materials. On the contrary in Sec. 4.5 a global ageing test in very different experimental condition will be discussed.

Tests have been performed by irradiating a triple-GEM prototype with a high intensity X-ray tube. The X-ray flux was $\sim$ 50 MHz/cm^2 and the irradiated area was about 1 mm^2. The gain changes induced by the ambient parameters variations (temperature and atmospheric pressure) have been corrected by a second, low irradiated, triple-GEM detector used as a reference chamber. The reference chamber has installed in the same gas line upstream the high irradiated chamber. During the tests no humidity monitoring has performed and the gas has supplied with an open flow system, using Rilsan tubes for a global tube length of 15 m

(including exhaust line). We cannot exclude that these measurements have done with a not negligible water content (hundreds of ppm) in the gas mixture. No oil bubblers have used on the exhaust gas line. A gas flow of 100 cc/min is flushed in order to avoid the gas pollution due to the irradiation flux. A similar value is expected to be used in the experiment.
The behavior of the normalized gain as a function of the integrated charge is shown in Fig. 3.34, Fig. 3.35 and Fig. 3.36 for the various gas mixtures tested.
The integrated charge is given from the sum of pad readout current and third GEM bottom electrode (*G3Down*) current. Such a sum in fact really evaluates the charge produced by the detector during its history; the use of only charge induced on pads would be affected by the sharing ratio of total current between readout and *G3Down*, that depends mostly on the induction field setup, but that could in principle be subject to variations introduced by the aging process itself.
For the same reason the charge integrated in 10 years of LHCb operation (Δt_{LHCb}) has been estimated as follows:

$$Q_{LHCb}^{integrated} = 2 \cdot \Phi_{LHCb} \cdot \Delta t_{LHCb} \cdot e \cdot N \cdot G \tag{3.15}$$

where the factor 2 takes into account that the integrate charge is the sum of the currents induced on these two electrodes (in all our setups the current share ratio between them is about 50%); e is the electric charge (1.6×10^{-19} C), N is the specific ionization that is estimated to be $\sim$ 40 electron-ion pair for all the gas mixtures, G is the gas gain used in the test and Φ_{LHCb} is the maximum m.i.p.-equivalent flux expected in M1R1 (460 kHz/cm^2), since the average flux was not yet well estimated at the time of these tests[8].
Tab. 3.4 summarizes the values of the gas gain, the integrated charge and the equivalent LHCb years of running for each of the gas mixtures tested.

Gas mixtures	Gas gain	Integrated charge (C/cm^2)	Equivalent LHCb years
Ar/CO_2/CF_4 (60/20/20)	2×10^4	20	$\sim$ 16 years
Ar/CO_2/CF_4 (45/15/40)	6×10^3	4.2	$\sim$ 11 years
Ar/CF_4/iso-C_4H_{10} (65/28/7)	1×10^4	10.2	$\sim$ 15 years

Table 3.4: Summary table of the local ageing test.

As shown in Fig. 3.34 and Fig. 3.35 no ageing effects for CF_4-based gas mixtures, have been observed , while a moderate ageing (less than 10% in 10 LHCb equivalent years) has been

[8]The updated value of average flux (184 kHz/cm^2) would demonstrate that such results are even better, but the original value has been kept here to maintain consistency with all the publications of our group.

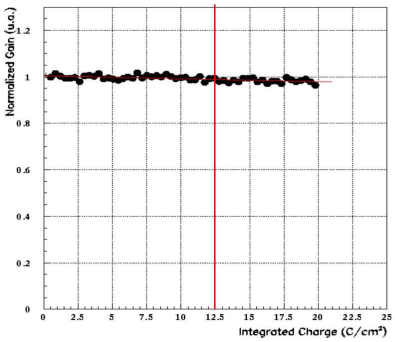

Figure 3.34: Normalized gain as a function of the integrated charge (PAD+G3D) for the $Ar/CO_2/CF_4$ (60/20/20) gas mixture [67]. The detector gas gain has been set at 2×10^4. The red line indicates the integrated charge corresponding to 10 years of operation at LHCb.

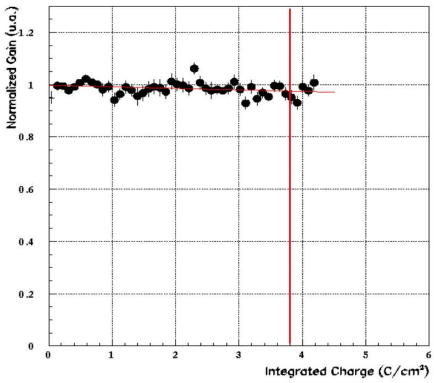

Figure 3.35: Normalized gain as a function of the integrated charge (PAD+G3D) for the $Ar/CO_2/CF_4$ (45/15/40) gas mixture [67].The detector gas gain has been set at 6×10^3. The red line indicates the integrated charge corresponding to 10 years of operation at LHCb.

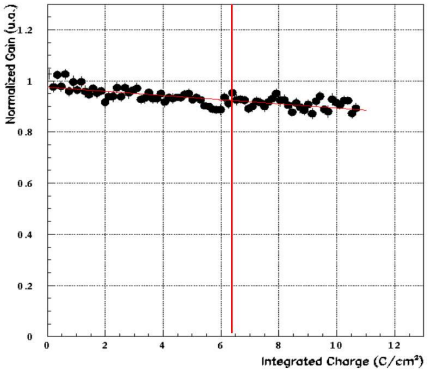

Figure 3.36: Normalized gain as a function of the integrated charge (PAD+G3D) for the $Ar/CF_4/iso\text{-}C_4H_{10}$ (65/28/7) gas mixture [67]. The detector gas gain has been set at 1×10^4. The red line indicates the integrated charge corresponding to 10 years of operation at LHCb.

observed with the Ar/CF_4/iso-C_4H_{10} gas mixture.
The positive result obtained with the isobutane gas mixture is probably due the presence of the CF_4 whose dissociation products, that can be very reactive radicals and can lead to the formation of hydrofluoric acid (HF) in presence of a not negligible water contamination, can be very effective in suppressing polymerization processes (CF_4 etching effect [72]).

3.8 Conclusions of the R&D activity

The R&D activity performed on the triple-GEM detector (10×10 cm^2 of active area) give us very interesting and unique results.
The detector shows very high rate capability, well above the maximum rate at LHCb.
The detector geometry, the electric fields configuration and the gas mixtures have been studied in order to optimize the detector efficiency in 20 ns time window and the time performance, and to minimize the discharge probability.
Time resolutions better than 5 ns are achieved with fast and high yield CF_4 and iso-C_4H_{10} based gas mixtures, considerably improving the results obtained in the past with the standard Ar/CO_2 (70/30) gas mixture ($\sim$ 10 ns).
With these new gas mixtures, the detector achieves an efficiency in 20 ns time window above the 96% at moderate gas gain, while keeping the discharge probability per incident particle lower than $\sim 5\times10^{-11}$.
In particular, the results with the high intensity pion/proton beams at PSI have shown that the use of a small fraction of iso-C_4H_{10} or a large amount of CF_4 results in very stable detector operation. Moreover, this test demonstrates that a triple-GEM is a very robust detector.
After a high intensity local X-ray irradiation equivalent to more than 10 years of operation at LHCb-M1R1, negligible ageing effects have been observed with the CF_4 based gas mixtures.

Taking into account these considerations and considering the necessity to avoid the use of flammable gas, we choose the Ar/CO_2/CF_4 (45/15/40) as the reference gas mixture for the LHCb experiment.
For this gas mixtures, the best choice for the electric fields of the detector is 3.5/3.5/3.5/5 together with the unbalanced configuration of the voltages applied to GEMs ($V_{GEM1} \gg V_{GEM2} \geq V_{GEM3}$).

Chapter 4

The triple-GEM detector in LHCb

The R&D performed on GEM detectors operated with fast gas mixtures has opened the way for trigger applications of this device. More specific studies have been required to fit the LHCb experiment needs, such as the design of the final detector, a further qualification of construction materials in the high-radiation environment, the definition of the service components (gas, low and high voltage), as well as the issues concerning the integration of the detector in the apparatus.
The responsibilities and the production has been shared between the two sites that participate to this project since the R&D phase: i.e. our group at the Laboratori Nazionali di Frascati (LNF) and the Cagliari section of Istituto Nazionali di Fisica Nucleare (Ca-INFN). Each site produced 18 chambers, corresponding to 6 instrumented station and 3 additional spare stations.
In the next section I describe the detector constraints and its design specifications; the description of the detector components is reported in Sec. 4.2; the construction procedure as well as the quality controls are discussed in Sec. 4.3; the electronics and service components in Sec. 4.4; the rad-hard qualification and the measurements of the performance of the final detector are described in Sec. 4.5 and in Sec. 4.6 respectively.

4.1 Detector overview and requirements

The total area of M1R1 region, about 0.6 m^2, will be covered with 12 stations composed by two triple-GEM detectors logically OR-ed pad by pad. The active area of each station is 200×240 mm^2.

The stations are arranged in four layers to provide full angular coverage: two layers are upstream and two downstream the wall support structure (Fig. 4.1).
Tab. 4.1 summarizes the space constraints of the M1R1 stations.

Station	Constraint
active area	200×240 mm^2
thickness	<75 mm
x-length	<430 mm
y-length	<310 mm

Table 4.1: Space constraints for a detector station in M1R1.

The stations must fit into the 37 cm space available between the RICH2 and the Preshower (Fig. 4.2).
However, the major constraint for the station is the space available around the beam pipe. Fig. 4.3 shows the transverse view ($y-x$ plane) with respect to the LHCb beam axis, as well as the chamber active area, the panels and the electronics dimensions. In this space is also included the gas pipes, the high voltage (HV) and the low voltage (LV) cables to supply the detectors and the electronics respectively.
The detector requirements in M1R1 region are:

- a particle rate capability up to 500 kHz/cm^2;
- each station must have an efficiency higher that 96% within 20 ns time window;
- a pad cluster size, i.e. the number of adjacent detector pads fired per track crossing the detector, should not be larger than 1.2 for a 10×25 mm^2 pad size;
- the detector must tolerate, without damages or performance losses, 10 years of harsh irradiation in such a region, with an average particle flux of 184 kHz/cm^2 for an average luminosity machine of 2×10^{32} cm^{-2} s^{-1};

Moreover, since the M1 is placed in front of the calorimeters, a special care has to be taken in the detector design to minimize the material budget. All components used for the chamber construction have been selected in order to minimize this requirement, obtaining a compromise between rigidity and low mass requirements. As shown in Tab. 4.2, the material budget of the detector station, electronics and Faraday cage is about 9% of X_0.

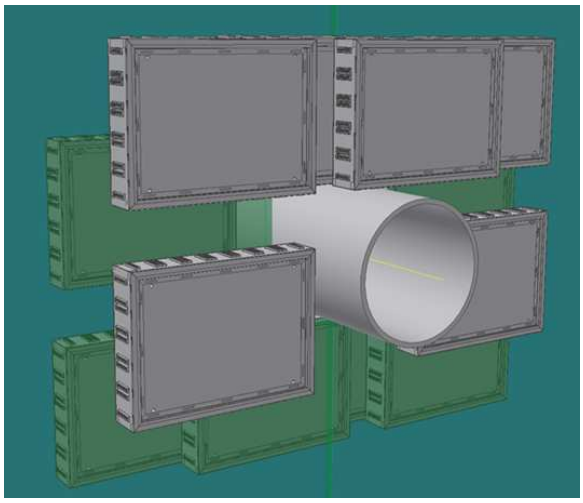

Figure 4.1: Sketch of the station arrangement in M1R1 region in the x-y plane. The two sets of detector stations, upstream and downstream the wall support structure, are shown with different colors.

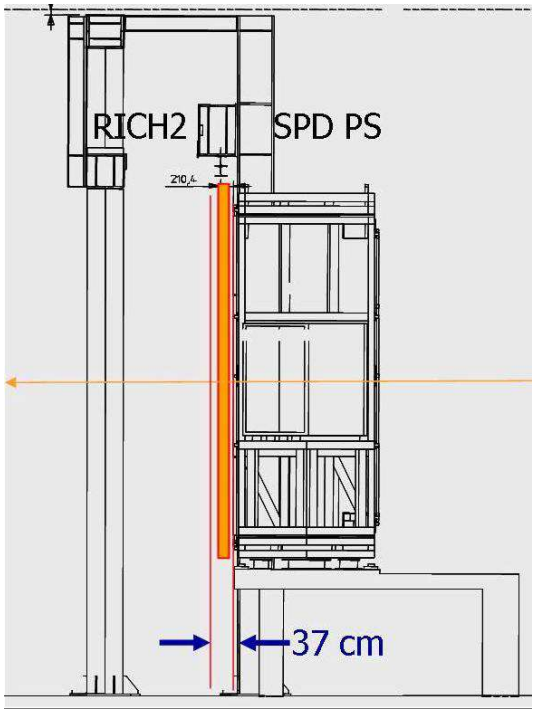

Figure 4.2: Sketch of the station arrangement in M1R1 region in the $y - z$ plane.

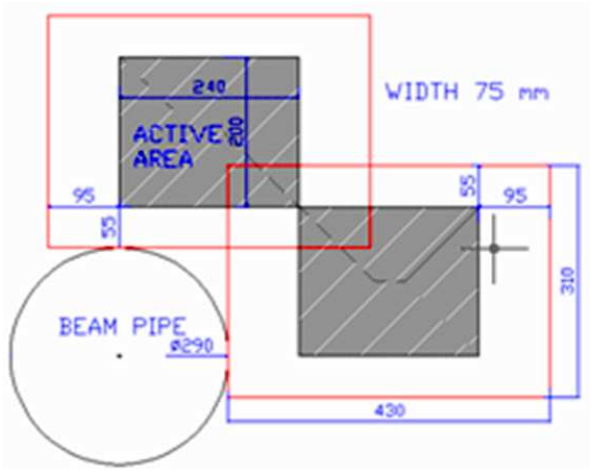

Figure 4.3: Transverse view ($x - y$ plane), with respect to the LHC beam axis, of the geometrical envelope of 2 out of the 12 stations, together with the chamber active area, the panels and the electronics dimension.

Detector component	**Materials**	**Radiation length** [cm]	**% of** X_0
3 GEMs foil	6×5 μm Cu	1.43	0.21
	3×50 μm kapton	28.6	0.05
			TOTAL: 0.26
Cathode plane	24 μm Cu	1.43	0.16
	2 mm FR4	19.3	1.03
	18 μm Cu	1.43	0.13
	1 μm Ni	1.42	0.007
	0.15 μm Au	0.33	0.005
	8 mm Honeycombs		0.15
			TOTAL: 1.48
Readout plane	24 μm Cu	1.43	0.16
	2 mm FR4	19.3	1.03
	18 μm Cu	1.43	0.13
	1 μm Ni	1.42	0.007
	0.15 μm Au	0.33	0.005
	8 mm Honeycombs		0.15
			TOTAL: 1.48
Frame (uniformly spread)	7 mm FR4	19.4	0.7
			TOTAL / chamber : 3.92
Electronics (uniformly spread)	1 mm $Si0_2$	12.3	< 0.5
Faraday Cage (uniformly spread)	300 μm Brass	1.43	< 0.5
			TOTAL / station : 8.84

Table 4.2: Material budget for a triple-GEM station.

In order to provide the full angular coverage, three stations are overlapped as shown Fig. 4.4, where the material budget distribution, in percentage of X_0, is reported. The material budget is $\sim 6\%$ X_0 in the active area, while it increases up to 20% in correspondence of the overlap of the FR4 frames.

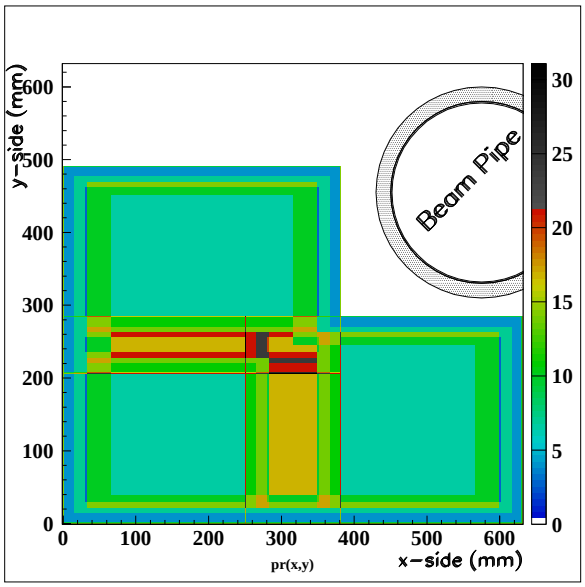

Figure 4.4: Material budget distribution in percentage of X_0 in the overlap of three stations.

4.2 Chamber components and design

The main components of the a triple-GEM chamber are: the cathode and the readout anode honeycomb panels, the GEM foils, the fiberglass frames that defines the gaps between the electrodes. As it will be explained in the Sec. 4.3, these components will be piled up and glued together to form the chamber.

4.2.1 The honeycombs panels

The main support of a chamber is given by two honeycomb panels acting as drift cathode and readout anode.
Such panels are composed by a 8 mm honeycomb foil glued between a gold plated (0.15 μm) PCB faced to the sensitive volume and a back-plane realized with a copper clad (12 μm) fiberglass foil (FR4, 1mm thick). The glueing is realized in a vacuum bag with all elements placed on a machined ALCOA-alloy reference plane.
The panels house two FR4 gas inserts, which are connected to the inner detector volume through two holes on the corner of the PCB. Four additional FR4 bushings are used as reference holes for the detector assembly and during the installation on the support wall.
Fig. 4.5 shows the various steps of the panels production, while Fig. 4.6 shows a sketch of the final panel assembly in the vacuum bag.
Panels are checked for planarity with a 3-D machine measuring on a grid of 35 points. Measurements of the first twelve panels show that the displacement from the average plane is of the order of 60 μm (r.m.s.) (Fig. 4.7).

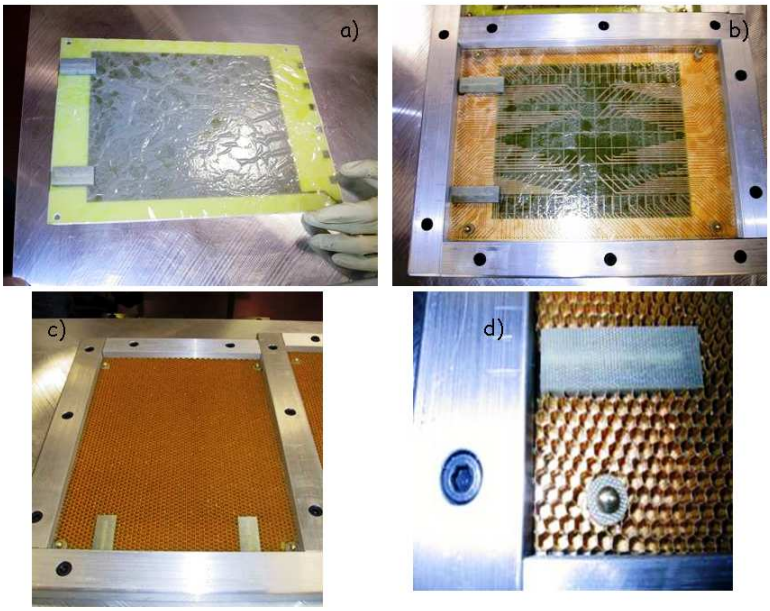

Figure 4.5: Panel production steps: (a) the cathode and (b) the readout PCB are coupled with gas inserts and four bushings. Then a thin 3M epoxy film is applied; c) the honeycombs foil, cut to size, is placed above followed by the back-plane; d) close view of the gas insert and the bushing.

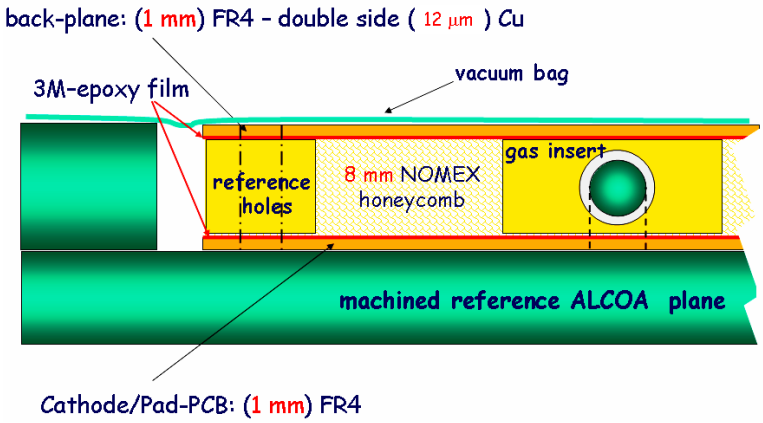

Figure 4.6: Sketch of the panel assembly in the vacuum bag.

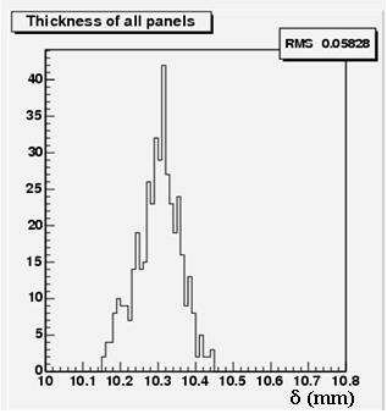

Figure 4.7: Distribution of the displacements from the average plane of twelve produced PCB panels.

Cathode PCB layout

The cathode PCB has an active area of 200×240 mm^2 realized with successive layers of copper (18 μm), nickel (1 μm) and gold (0.15 μm).
On one side (Fig. 4.8), seven pads are used as HV connections for all the electrodes that compose the detector.

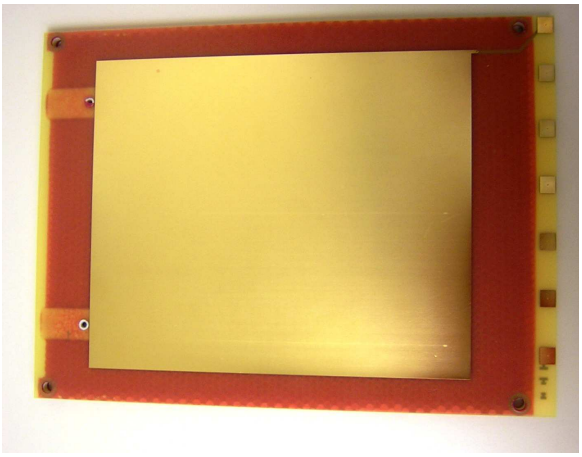

Figure 4.8: The PCB cathode: the gold-plated area represents the active area of the chamber. The two gas inserts and the seven HV pads are visible on the left and the right of the picture respectively.

Pad-readout PCB layout

The readout PCB is a matrix of 8×24 gold-plated pads (25×10 mm^2) with a ground grid of 100 μm between the pads (Fig. 4.9).

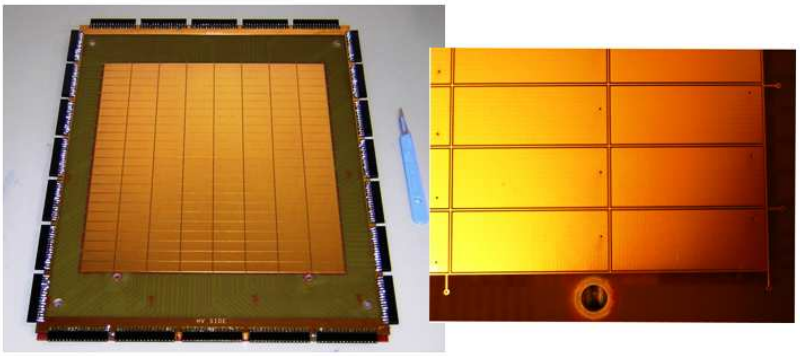

Figure 4.9: The pad readout: the gold-plated pad matrix of 200×240 mm^2 represents the active area of the chamber. The gas insert and the ground grid between the pads are shown in the detail.

The choice of this pad layout is motivated by the reduction of the pad cluster size, as demonstrated in a test on PS beam at CERN in 2004, where the performance of two chambers, one with this pad layout and the other without the ground grid between pads, were measured. A fine scanning of the detector response as a function of the particle impact point was performed, by means of small *finger* scintillators (3 mm wide) selecting only particles crossing the chamber on specific position inside the pad.
In Fig. 4.10 the scan at fixed detector gain over several pads is shown. The ground grid layout, reducing the cross-talk between pads, allowed to obtain a lower pad cluster size, while keeping a high efficiency. Such scans were performed for several detector gains, and the pad cluster size reduction effect of the ground grid is evident especially for higher gains (Fig. 4.11).
Pads signals are carried out through connectors placed all around the perimeter of the PCB, passing on the rear of the PCB. The capacitance (Fig. 4.12) of each pad including traces up to the output connector, which affects the minimum value of the electronics threshold, has been kept below 30 pf with the layout shown in Fig. 4.13.
A readout panel is validated for the chamber production if it satisfies the mentioned planarity criterion and if shorts or even some visible conductance (less than 10MΩ) are not present

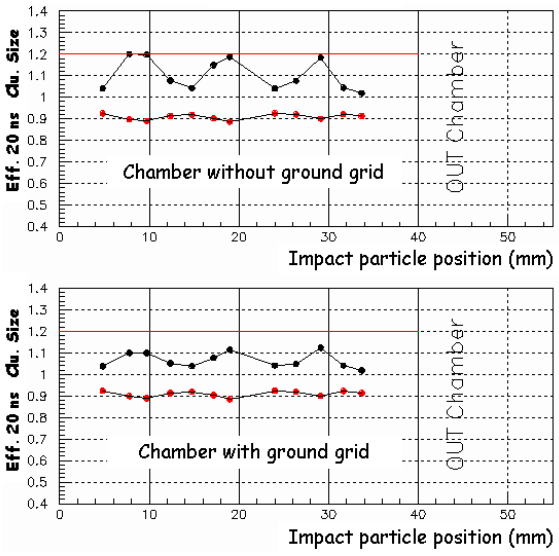

Figure 4.10: The pad cluster size (black dots) and the efficiency within 20 ns time window (red dots) as a function of the impact particle position for two chambers with different pad layouts.

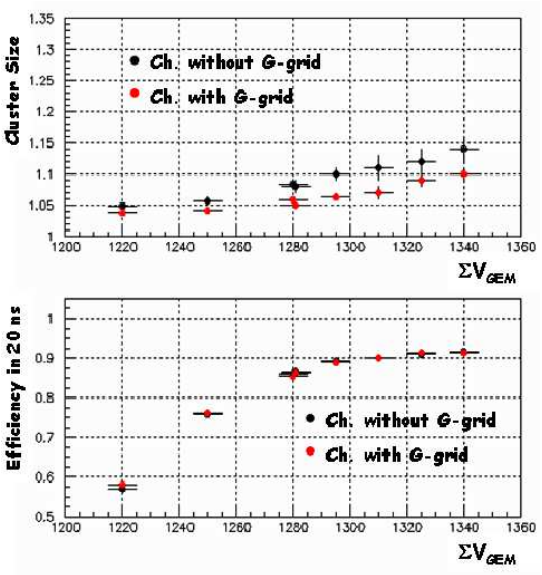

Figure 4.11: Average geometrical pad cluster size and average efficiency in 20 ns time windows as a function of V_{GEM}^{tot} for the pad layout with a ground grid (red dots) and without the grid (black dots).

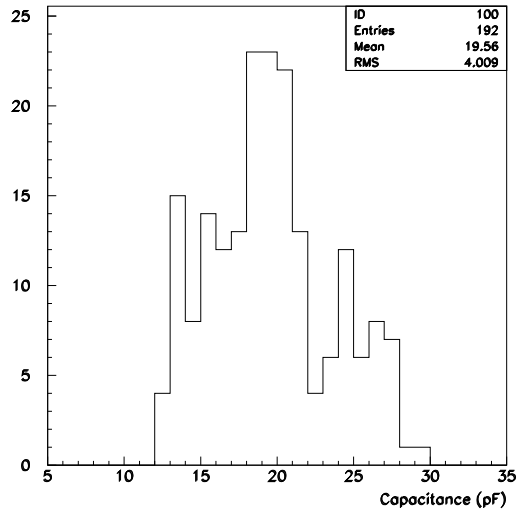

Figure 4.12: Capacitance distribution of our pad layout.

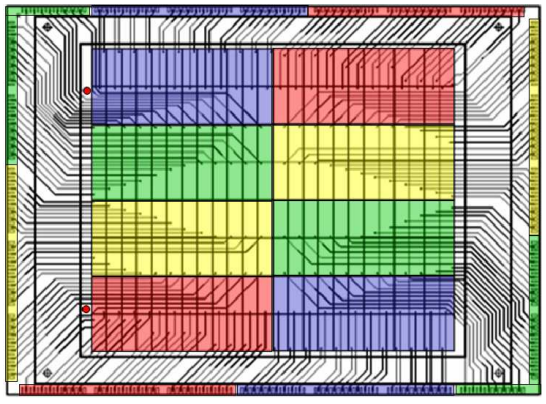

Figure 4.13: The readout PCB connections layout

between pads or pad to ground.

4.2.2 The GEM foil

The GEM hole has a bi-conical shape with an external and internal diameter of 70 μm and 50 μm respectively, and hole-pitch of 140 μm.
The GEM foils are manufactured by the CERN-EST-DEM workshop following the requested design. The foil has an active area of 202×242 mm^2, a bit greater than cathode and anode, to take into account for a small misalignment in the chamber.
Moreover, in order to reduce the energy stored on the GEM and the discharge propagation, one side of the foil has been divided in six sectors ($\sim 66\times240$ mm^2). The separation between sectors is 200 μm.
Fig. 4.14 shows the segmented side of a GEM foil and the HV connections. Sectors will be protected with 1 MΩ SMD limiting resistors, that are soldered after the frame glueing.

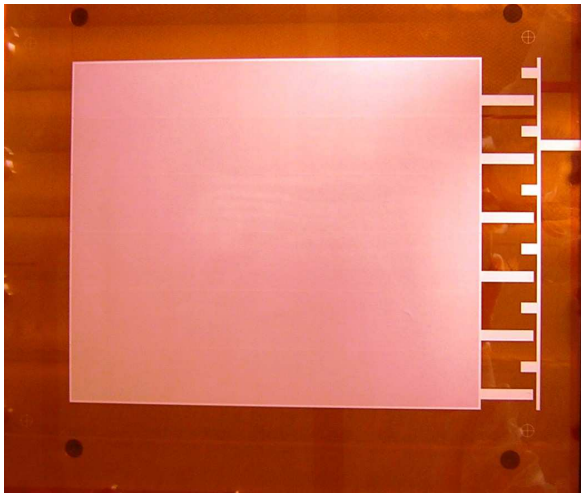

Figure 4.14: A GEM foil as seen from the segmented side. The HV connections are visible on the right of the picture.

Severe quality tests are performed on GEM foils. A preliminary optical inspection is performed with a microscope to check for photolithographic imperfections. Pictures in Fig. 4.15 shows some of the typical defects causing the rejection of a foil.
If the GEM foil passes the visual inspection, a high voltage test is performed. Such a test is done in a gas tight box (Fig. 4.16), flushed with nitrogen in order to keep the relative hu-

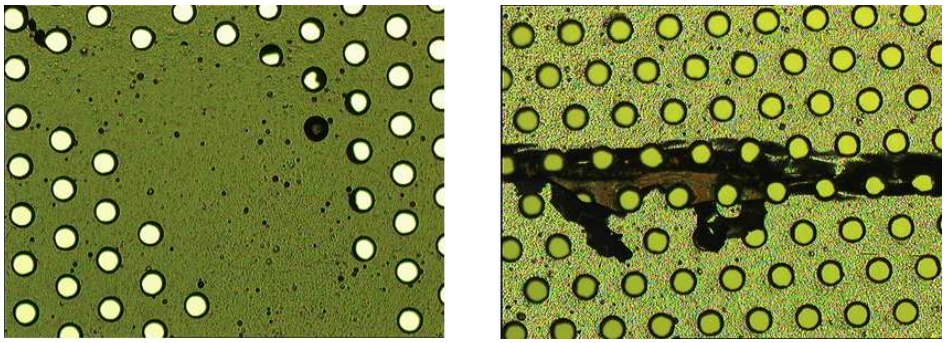

Figure 4.15: Typical GEM defects: top) closed holes; bottom) over-etching of the copper layer.

midity at $\sim$ 25% level. The voltage is applied through a 100 MΩ limiting resistor, to avoid damages in case of discharges. The acceptance requirement is a maximum leakage current of 1 nA at 500 V. The HV test is performed twice: on a new GEM foil; after the frame glueing and the soldering of the SMD limiting resistors in the slots of the frame, just before the final assembly.

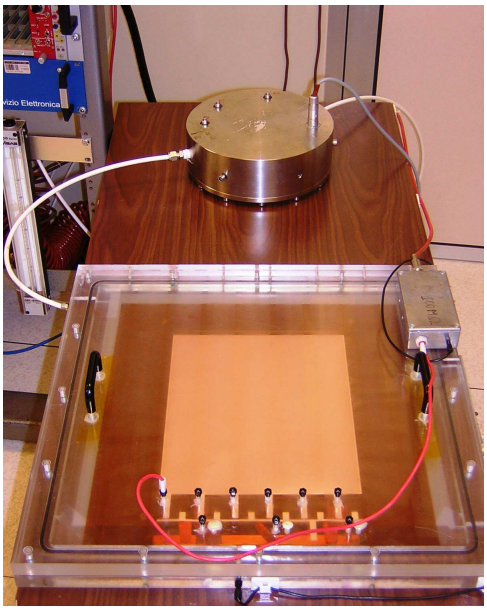

Figure 4.16: The gas tight Plexiglas box used for the HV test of GEM foils.

4.2.3 The frames

The GEM electrodes are supported by fiberglass frames (FR4) of suitable size and thickness (1, 2 or 3 mm), accordancing with the gap geometry of the detector.
On the HV side six slots, realized by the machining of the frames, house the limiting resistors. Four holes, drilled at the corners of the frame, are used as reference holes for the chamber construction. The layout of the frame in shown in Fig. 4.17.
Since the internal side of the fiberglass frame are in contact with the sensitive volume of the detector, they are visual inspected in order to find and eliminate any residual spikes or broken fiber. After the final cleaning, performed by means of an ultrasonic bath of deionized water, frames are dried in an oven at a temperature of 80^{o}C for 12 hours (Fig. 4.18).

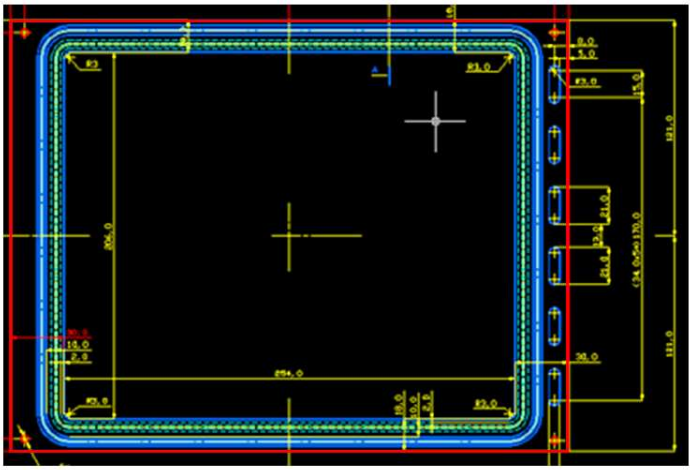

Figure 4.17: The frame layout.

Figure 4.18: The clean procedure of the frame. From the left to the right: the visual inspection; the cleaning in the ultrasonic bath; the drying in the oven at 80 ^{o}C.

4.3 Chamber construction and tools

All the construction operations are performed inside a class 1000 clean room. A sketch of the triple-GEM assembly is shown in Fig. 4.19.
The whole assembly procedure has been defined in each steps as follows:

- The GEM foils, good for the optical inspection as well as the HV quality tests, are stretched with a home-made tool equipped with jaws and gauge meters to monitor the applied tension. A mechanical tension of about 20 MPa is applied on the four sides of the foil (Fig. 4.20). The advantages of this stretching technique will be discussed in detail in the next section.

- The frame is glued on the stretched GEM foil using the Araldite 2012 epoxy, easy to handle (5 minutes work life and 2 hours curing time) and characterized by high electrical properties. The aging properties of this glue have been studied during the global irradiation test (see Sec. 4.5). In order to prevent epoxy spreading into the active area and to assure an uniform glue layer, a rolling wheel tool is used to apply the epoxy on the frame. Each GEM foil is framed following the above procedure with 1, 2 and 3 mm thick frame.

- The 1 MΩ SMD limiting resistors are soldered in the 6 slots of the frame (Fig.4.21) and a HV test of the GEM foil is performed again.

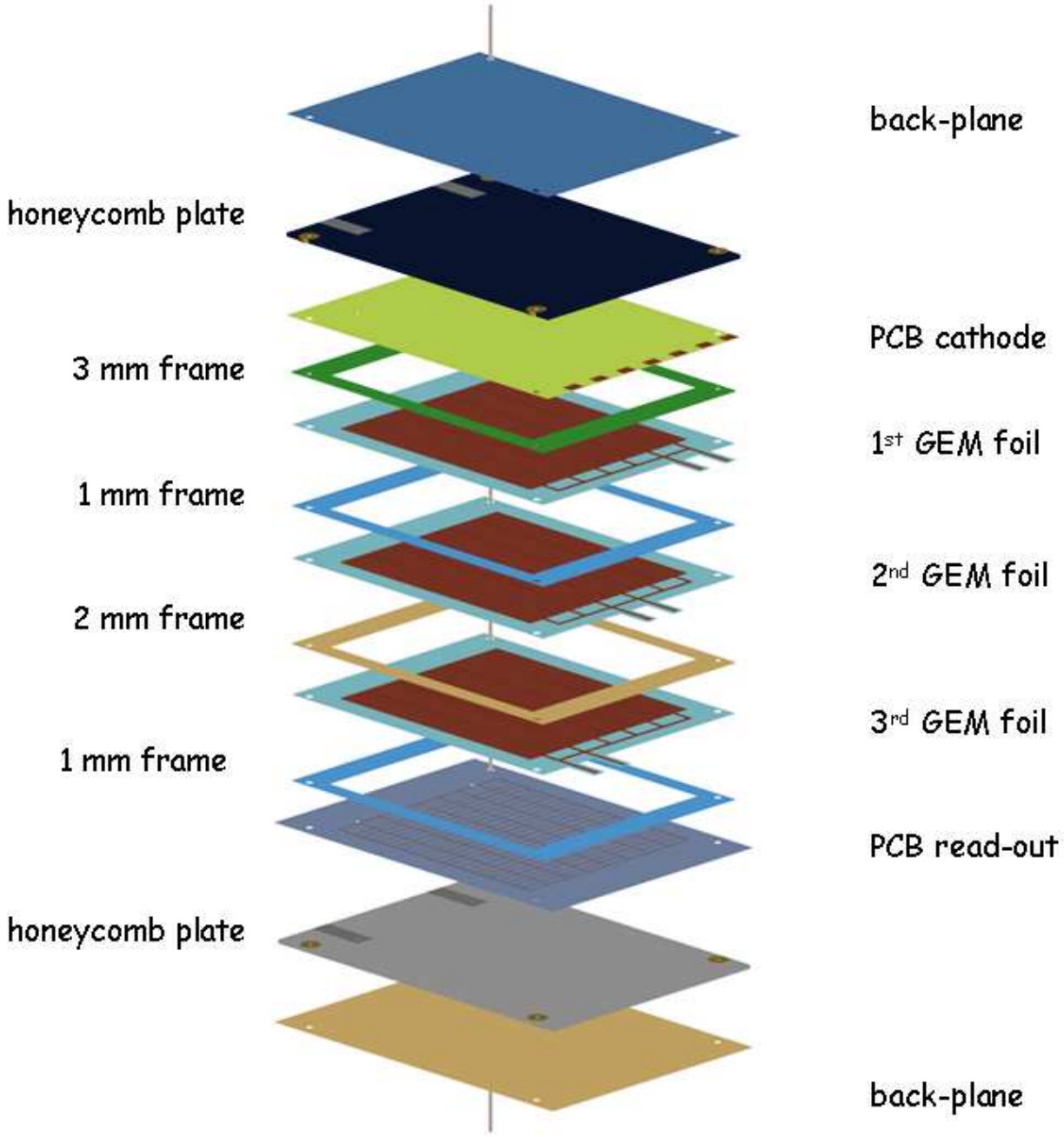

Figure 4.19: Exploded view of a triple-GEM assembly.

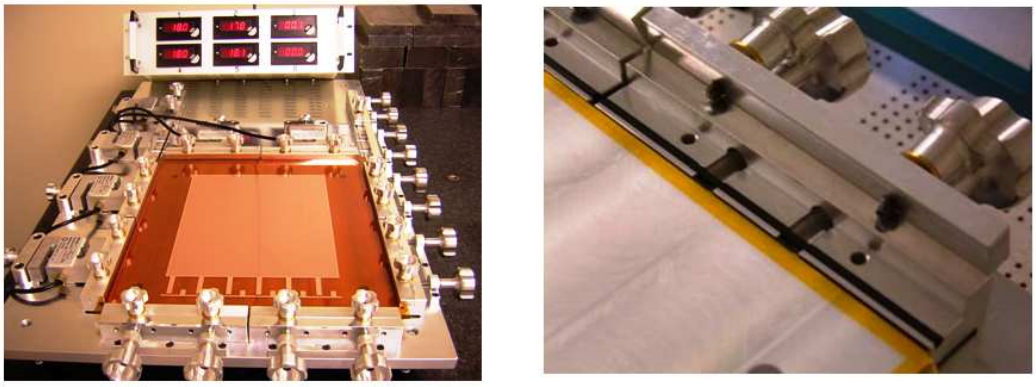

Figure 4.20: Left: The GEM foil under stretching; Right: a close view of the jaw, equipped with a plastic O-ring, used to clamp the foil.

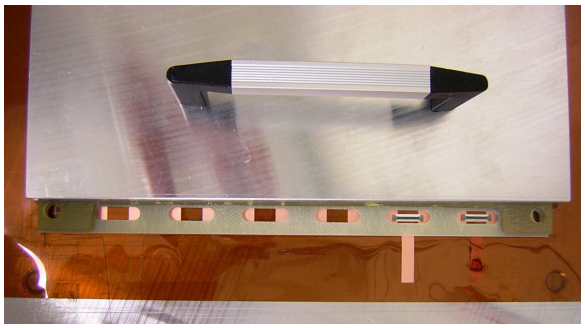

Figure 4.21: Soldering of the SMD limiting resistor inside the six slots of the frame.

- The three *framed GEMs* are glued on the top of the cathode PCB using the four reference pins to guarantee a precise mechanical positioning, in the following order: the 3 mm thick framed GEM, defining the drift gap; the 1 mm thick framed GEM (1^{st} transfer gap); the 2 mm thick framed GEM (2^{nd} transfer gap); and finally a 1 mm thick bare frame followed by the pad panel, defining the induction gap (Fig. 4.22).
  This assembly operation is operated on a precisely machined ALCOA-alloy reference plane. On the top of the whole sandwich a load of 100 kg is uniformly applied for 24h, as required for epoxy polymerization (Araldite AY103 + HD991 hardener). This glue has been preferred for this operation for his longer cure time (about 2 hours) that fits

the time needed for the whole detector assembly. It ensures a good electrical behavior, convenient handling properties and well-known aging properties [73].

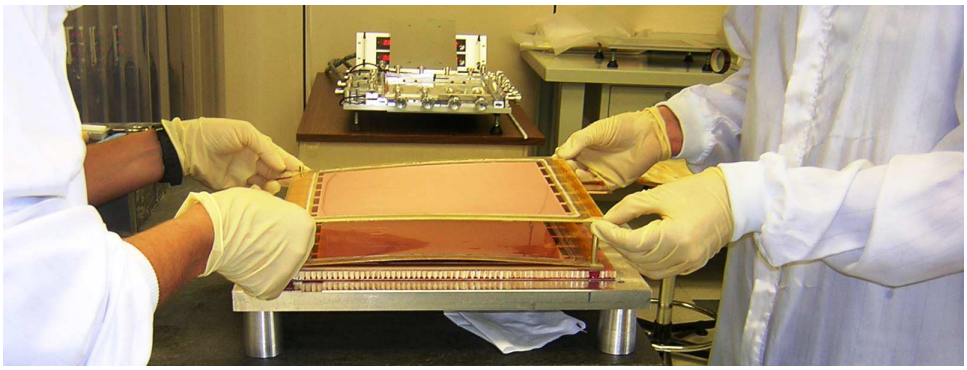

Figure 4.22: The framed GEMs are assembled on the cathode PCB.

- The last step is the soldering of the HV connections of all the GEM foils to the relative pads realized on the cathode panel. To avoid gas leaks from the corners of the chamber and to hang up the chamber on the muon wall, Stesalite bushings are inserted and glued in the the four reference holes of the structure.

4.3.1 The stretching of the GEM foil

The electrostatic force between the electrodes of two consecutive GEM foils can produce a sag of the foil itself, leading to electrostatic instabilities such as foil oscillation or possible discharges, or giving rise to local detector gain fluctuations.
In the triple-GEM detectors of COMPASS experiment, the GEM foils are not stretched and, to avoid problems associated with the sag, a grid of thin fiberglass spacer ($\sim$ 400 μm width) was used as a support for the GEM foil. Of course the support grid, placed inside the active area, causes some detector inefficiency [73].
To avoid electrostatic instability and to achieve a good uniformity of the detector response, we decided to stretch the GEM foil. The mechanical tension to apply on the GEM foil and its long term behavior have been accurately investigated.

The electrostatic pressure

In a planar capacitor the electrostatic attraction established between the two electrodes is given by [74]:

$$\frac{F}{S} = \frac{\epsilon}{2} \cdot (E)^2$$

where E is the applied electric field expressed in V/m and F/S is the electrostatic pressure expressed in Pa.

As previously described, a GEM detector is a system composed by several planar electrodes: since these electrodes are forced by power supply to be at a certain voltage, each single foil is attracted towards an equilibrium position placed at precise distances from the two neighbouring electrodes. At a first level of approximation, only on the third GEM foil the resultant force is different from zero, because of the greater induction field (5kV/cm) with respect to the second transfer field (3.5kV/cm) applied on the other face.

An *"upper limit"* estimation of the electrostatic pressure can be done taking into account the application of only a 5kV/cm field applied on one side of the GEM foil: assuming the permittivity of the gas mixture to be the same as that of the vacuum, an equivalent pressure of $\sim$1 Pa is obtained.

To estimate the sag produced by 1 Pa, a uniformly distributed load of 0.8, 1.6 and 2.4 N is applied on a GEM foil previously stretched at 20 MPa, and the foil bending is measured on a grid of 25 points with a 3-D machine (Fig. 4.23, 4.24).

From these measurements, assuming a linear dependence of the sag from the mechanical pressure, a maximum sag of $\sim$ 15 μm is extrapolated in the case of 1 Pa electrostatic pressure. Such a displacement, as demonstrated in Sec. 4.3.2, is practically negligible with respect to the one introduced by to the mechanical tolerance of about 100 μm, mainly due to the GEM glueing operations. Moreover no electric instabilities due to foil oscillations has been ever observed on all constructed chambers: the dark current on all electrodes is always below 1 nA.

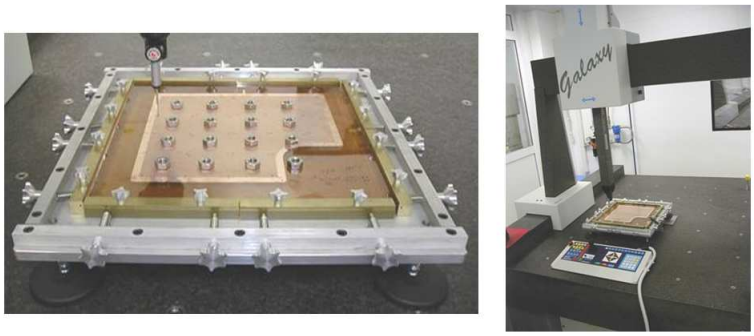

Figure 4.23: Left: Close view of the distributed load on the GEM foil; Right: The 3-D machine used for the measure GEM sag.

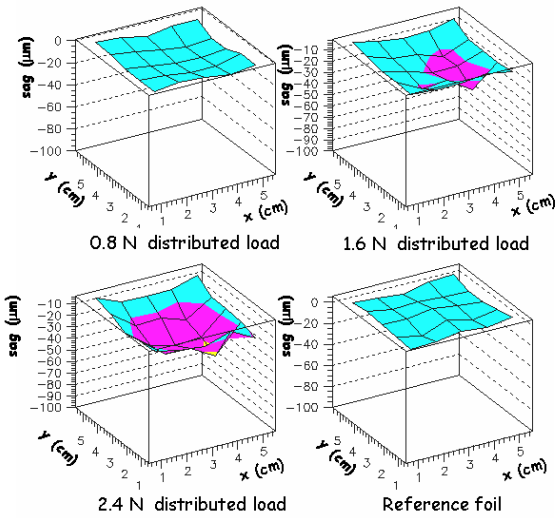

Figure 4.24: Measure of the bending of a GEM foil, previously stretched at 20 MPa, when a distributed load of 0.8, 1.6 and 2.4 N are applied.

The kapton creep

An additional effect to be taken into account is the kapton *creep*, i.e. the plastic deformation of the kapton when it is stressed above its yield stress [75]. The yield stress is the force at which the material behavior changes from the elastic to the plastic regime. In fact, applying repeatedly a mechanical tension to a GEM foil, the kapton strain does not return to its initial state. Fig. 4.25 shows the mechanical tension applied on a kapton foil, normalized at 20 MPa, as a function of the time for two consecutive stretching procedures. After two hours a mechanical tension loss of $\sim$ 10% is observed, while the creep rate decrease to about $\sim$ 1% in the same time interval. Taking into account for this effect, the GEM foil is stretched twice before to proceed for the gluing of the frame.

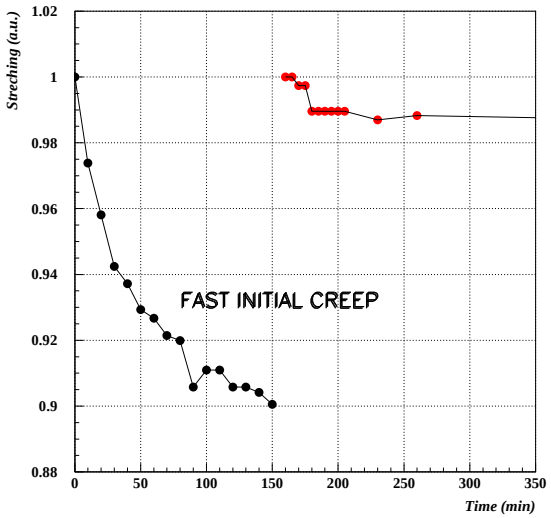

Figure 4.25: The mechanical stretching behavior as a function of the time. Repeated stretching allows to practically recover the kapton *creep* rate.

The effect of radiation

The radiation effects on the mechanical stretching of the GEM foil and on the epoxy resin, used to glue the GEM on the fiberglass frame, have been studied during the irradiation test described in Sec. 4.5. A *framed* GEM foil, produced with the procedure described in previous section, has been exposed to the same highly radioactive source used for the ageing test

of the detectors.
Before the irradiation such a foil showed a sag of $\sim$ 95 μm under a distributed load of 1 N applied on its surface.
After 10 days of irradiation at 20 Gy/h (equivalent to 4 years of operation at LHCb experiment), a sag of 120 μm has been measured in the same load conditions, corresponding to a mechanical tension loss of $\sim$ 20%, which, taking into account that the expected sag due to electrostatic force is less then 15 μm, demonstrate a negligible increase of few μm of the sag during detector irradiation.

4.3.2 Mechanical specifications

The uniformity of the chamber performances, such as the efficiency and the gas gain, mainly depends on the tolerance of the dimensions of each gap. In fact, since the tolerance on the GEM hole diameter is by manufacturing process very tight, $\pm$ 2.5 μm, and the gas gain saturates in the hole range of 40$\div$70 μm, the effect on the gain due to hole diameter disuniformity is practically negligible.
Taking into account the planarity of the PCB panels, the possible disuniformity of the glueing operations, the precision of the frame thickness, we estimate a global mechanical tolerance of $\sim$ 100 μm for each gap of the chamber.
As discussed in Sec. 3.4.3, the effective gain of a GEM detector is the product of the intrinsic gain of each GEM stage and the electron transparencies, that depend on the electric field inside the GEM holes and the electric field of the various gaps, i.e. E_D, E_{T1},E_{T2}, E_I.
Since the electric field can be assumed constant across the gap, its value is done by the ratio of the voltage difference applied to the electrodes and the thickness of that gap, i.e V/d. Therefore, a local variation of the gap thickness (δgap) will correspond to a variation of the electric field in the gap (δE_{gap}) and consequently to a variation of the effective gain, δG_{eff}, through the changes induced on the electron transparency, T:

$$\delta gap \implies \delta E_{gap} \implies \delta T \implies \delta G_{eff}$$

Since the effective gain is correlated with the charge collected on the the pads readout, the measurements of the effective gain has been performed measuring the current induced on the pads.

Considering that the drift field is set to 3.5 kV/cm in order to maximize the drift velocity

of the Ar/CO_2/CF_4 (45/15/40) gas mixture (Fig. 4.26), a mechanical tolerance of $\pm$ 100 μm on the drift gap, 3 mm thick, is $\sim$ 3% of the gap size, equivalent to a drift field variation of $\pm$ 0.1 kV/cm. The pad current as a function of the drift field is shown in Fig. 4.27. The red dotted line indicates the value chosen for the drift field, while the black lines indicate the range of variation ($\pm$ 0.1 kV/cm) corresponding to a mechanical tolerance of $\pm$ 100 μm. The resulting effective gain variation (δG_{drift}) is of the order of $\pm$ 1%.

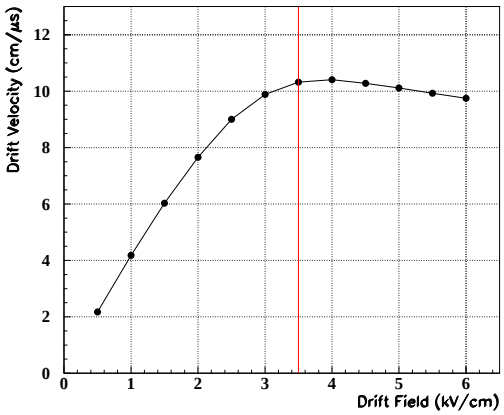

Figure 4.26: Electron drift velocity as a function of the drift field. The maximum drift velocity is reached when the drift field is set at 3.5 kV/cm.

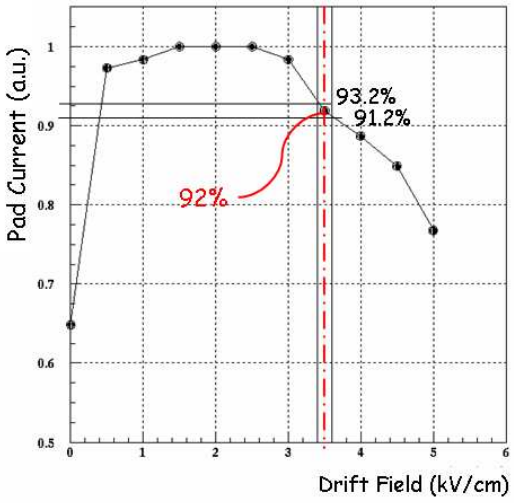

Figure 4.27: Normalized pad current of the detector as a function of the drift field. For a mechanical tolerance of $\pm$ 100 μm, the effective gain changes of about $\pm$ 1%.

The electric field of the first transfer gap is set to 3.5 kV/cm as a compromise between high transparency and low discharge probability, which is shown in Fig. 4.28 for different value of the first transfer field (measurement done with α source, see [61]). With an electric field of 3.5 kV/cm, the discharge probability results to be a factor of three less than that one obtained with 4.5 and 5 kV/cm. This is due to a larger *extraction fraction* on the second multiplication step corresponding to a higher possibility to reach the Reather limit [69].
A mechanical tolerance of $\pm$ 100 μm for the first transfer gap, that for our detector is 1 mm thick, corresponds to a transfer field change of $\pm$ 0.35 kV/cm, and a gain variation (δG_{tran1}) of $\pm$ 3% (Fig. 4.29).

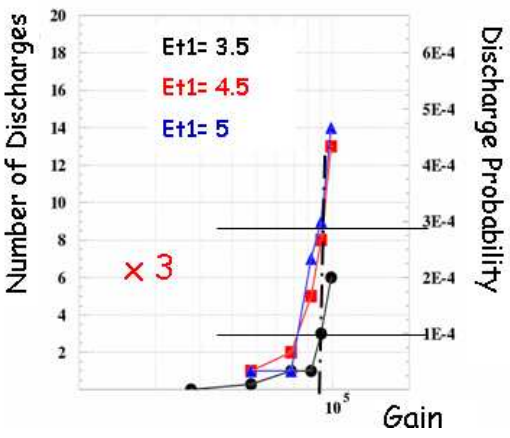

Figure 4.28: Discharge probability as function of the effective gain for different values of the first transfer field measured with an α source [61].

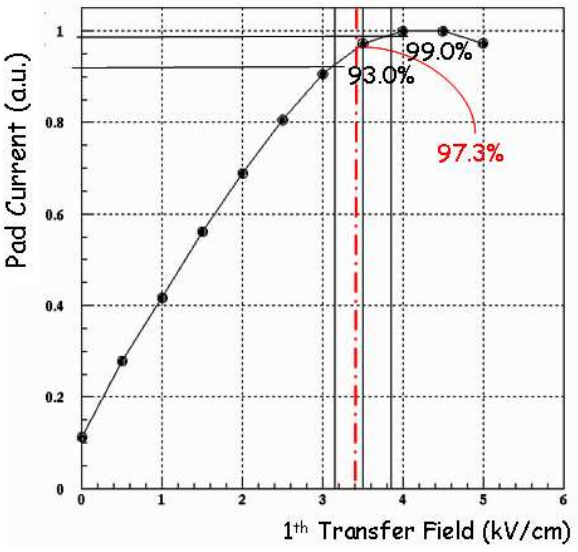

Figure 4.29: Normalized pad current as a function of the first transfer field. For a mechanical tolerance of $\pm$ 100 μm, the effective gain changes of about $\pm$ 3%.

At the same way, the second transfer field is set to 3.5 kV/cm as a compromise between high transparency and low discharge probability. As for the first transfer field, an electric field of 3.5 kV/cm ensures a discharge probability which is factor of two less than that one obtained with higher values [61] (Fig. 4.30).
For the second transfer field, a mechanical tolerance of $\pm$ 100 μm, which is 2 mm thick, is equivalent to a variation of the second transfer field of $\pm$ 0.18 kV/cm, corresponding to gain variation (δG$_{tran2}$) of $\pm$ 3%, as shown in Fig. 4.31.

The induction field allows to adjust the charge sharing between the pad and the bottom electrode of the third GEM. The current sharing on the pad and the bottom electrode of the third GEM, as a function of the induction field, is shown in Fig. 4.32. Due to the quite steep dependence of the effective gain on the induction field, a mechanical tolerance of $\pm$ 100 μm, 1 mm thick, corresponds to an induction field variation of $\pm$ 0.5 kV/cm, inducing a gain changes, δG$_{ind}$, of the order of $\pm$ 4%.

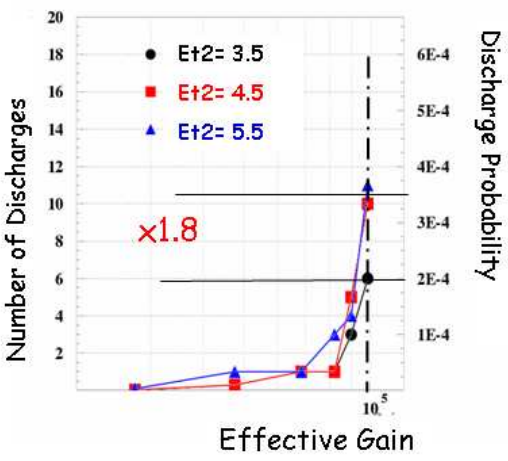

Figure 4.30: Discharge probability as a function of the effective gain for different values of the second transfer field measured with an α source [61].

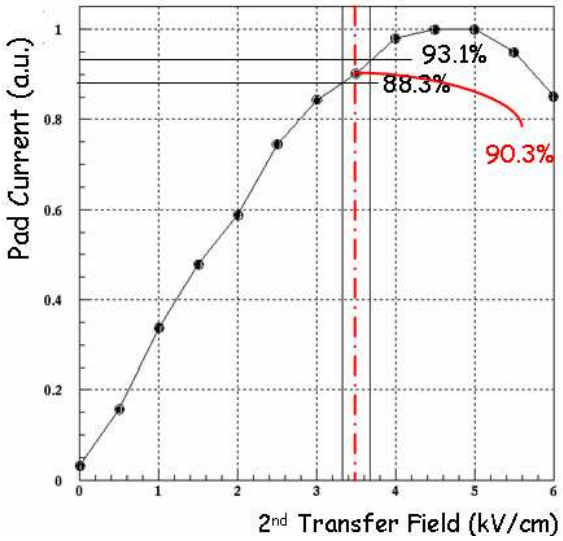

Figure 4.31: Normalized pad current as a function of the second transfer field. For a mechanical tolerance of $\pm$ 100 μm, the effective gain changes of about $\pm$ 3%.

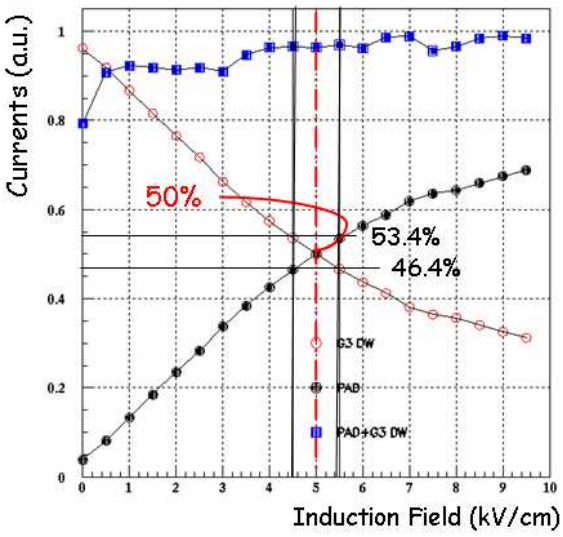

Figure 4.32: The current sharing on the pad (red dots) and on the bottom electrode of the third GEM (black dots) as a function of the induction field. A mechanical tolerance of $\pm$ 100 μm produces an effective gain variation of $\pm$ 4%.

In Tab. 4.3 the single contributions to the gain variation coming from each single gap are summarized. The global effect, ΔG_{eff}, obtained as the squared sum of each single contribution, comes out to be of the order of $\pm$ 6%.
A comparison between this estimation and a direct measurement of the gain uniformity of our chamber will be reported in the next section.

	Gap Thickness [mm]	E_{field} [kV/cm]	δE_{field} (δ gap = $\pm$ 100 μm) [kV/cm]	δG_{eff} [%]
Drift	3	3.5	0.1	1
1^{st} transfer	1	3.5	0.35	3
2^{nd} transfer	2	3.5	0.18	3
Induction	1	5.0	0.5	4
			Total Δ G_{eff}	*6*

Table 4.3: Summary of the gain variation due to a mechanical tolerance of $\pm$ 100 μm in each gap of the detector.

4.3.3 Quality check

Several quality check are performed, before the chamber assembly, on different detector components. Among these tests, the GEM foil tests and the panel planarity checks are discussed in the previous sections. For all the assembled chamber, before coupling them to form the station, the gas tightness and the gain uniformity are measured.

Gas leak test

In the experiment the gas mixture will be supplied in parallel for the 12 stations with an open flow system. The choice of an open flow gas system is due to the high irradiation of M1R1 region, that cause the deterioration of the gas mixture. In a closed gas loop system the polluted gas can cause a premature ageing of the detector (see Sec. 4.5).
Also a gas leak could imply an undesirable contamination of the gas mixture, for example with H_2O. Taking into account the large amount of CF_4 (40%) presents in the gas mixture, a small fraction of water could give rise to the formation of hydrofluoric acid (HF), that could

etch the detector electrodes.

The gas leak rate is measured with respect to the one of a reference chamber, in order to take into account for atmospheric pressure and temperature variations. The leak of this reference chamber has been accurately measured in dedicated long runs, looking for periods of constant or repeating environmental conditions, and it is less than 2 mbar/day.

The setup of the test is shown in Fig. 4.33. Both chambers are placed in a foam box, to ensure a good thermal insulation, and are inflated in parallel up to an overpressure of ~ 10 mbar. Then the overpressure decay is monitored through two distinct probes and compared (Fig. 4.34).

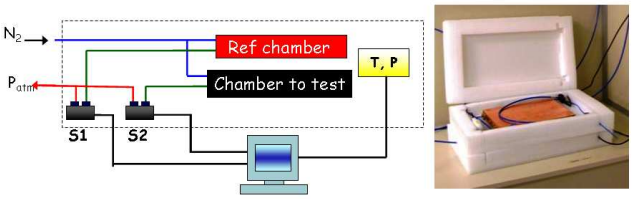

Figure 4.33: Gas leak setup.

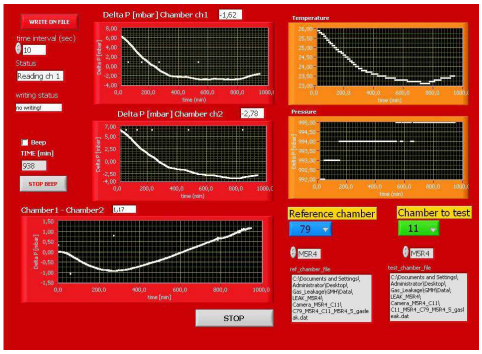

Figure 4.34: Monitor display of the leak rate measurement.

The typical gas leak rate of the chambers is of the order of few mbar/day, as shown in Fig. 4.35, where rates of 2 mbar/day of most of the produced chambers mean a gas leak comparable or lower than the one of the reference chamber. Such values ensure a humidity level of less than 100 ppm per volume for a gas flow rate of 80 cc/min (as foreseen for the experiment).

Gain uniformity measurements

The uniformity gain is performed with a ~ 6 keV X-ray tube (Fig. 4.36). The current induced on each pad, 192 per chamber, is read-out with a 1 nA sensitivity current-meter and corrected for the temperature and the pressure variations. The water content and the temperature of the gas mixture are monitored with a probe mounted on the gas line outlet. The atmospheric

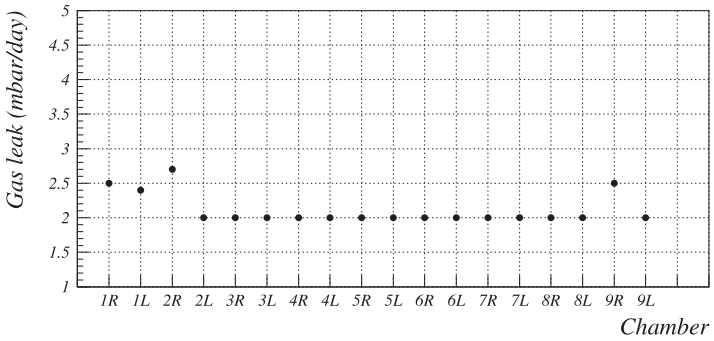

Figure 4.35: Gas leak rate of the whole LNF site production

pressure is monitored outside the gas line with another probe. The chamber is mounted on a X-Y plane moved with computer controlled step-motors. The measured gain uniformity is shown in Fig. 4.37. Taking into account the pad size (25×10 mm^2), the diameter of the X-ray collimator ($\sim$ 5 mm) and the X-ray beam spread, the small gain losses are due to a not full illumination of the 64 border pads.

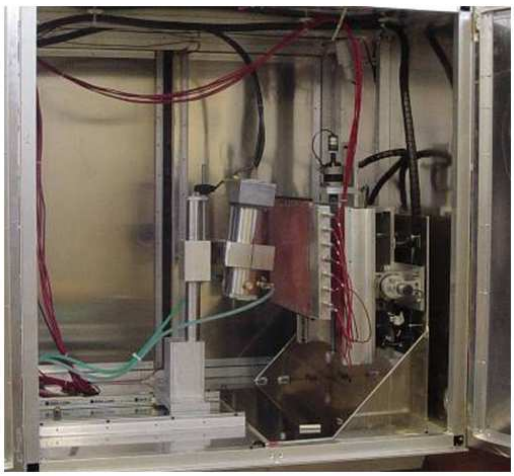

Figure 4.36: Picture of the X-ray tube.

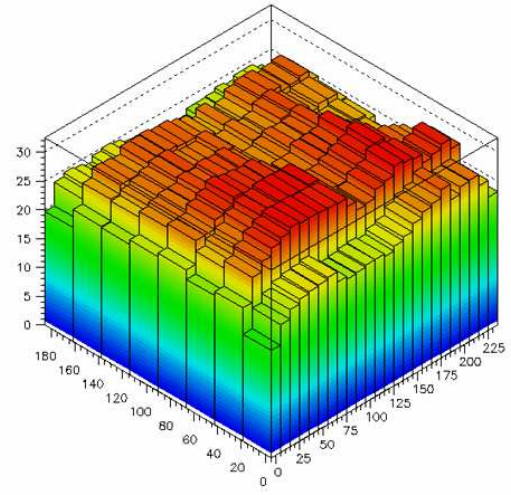

Figure 4.37: The gain uniformity measurement performed on a single chamber.

The measured gain uniformity with and without the border pads are better than 12% and 6% respectively. Not considering the border pads of the readout, the measured gain uniformity is in good agreement with the estimated contribution of the mechanical tolerances of detector

gaps, as discussed in the previous section.
In Fig. 4.38 the measurements on LNF site production is shown.

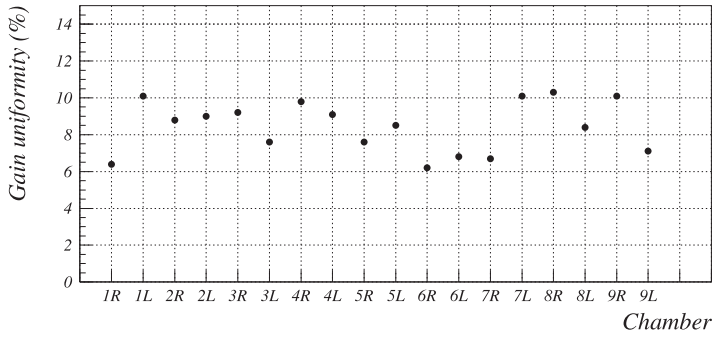

Figure 4.38: Gain uniformity of the LNF site production

4.3.4 The detector integration

A M1R1 detector is composed by two of the described chambers, coupled through the reference facing the two cathode panels one to each other. Such a station is then integrated with the Faraday cage, the front-end electronics (FEE) boards, the HV filters and connectors, the gas pipes, the LV and signals distribution card (Fig. 4.39).
The FEE boards are mounted all around the perimeter of the station, and one of the difference with respect to the MWPC boards (see Sec. 4.4.1) is that all chips and components are embedded on the same board, due to the tight space constraints especially near the beam pipe. This explains also the design of the HV filters, that had to fit in the space behind FEE board in the HV side of the chamber, and the HV connector (radiation hard, produced by Radiall), embedded in the one of the angle bar of the Faraday cage.
Inlet and outlet gas pipes are split in two smaller line in order to obtain a more uniform gas supply. The gas flows in the first chamber of the station, entering through the two gas inserts of the readout panel and exiting from the two gas inserts of the cathode panel; then it flows in the second chamber, entering through the cathode inserts and exiting from the anode inserts towards the exhaust.
Each completely integrated station is switched on (HV as well as FEE) and kept under test for at least one day: HV currents are monitored and the FEE noise rate is measured. The presence of dead channels is investigated exploiting the pulse generation feature of the FEE

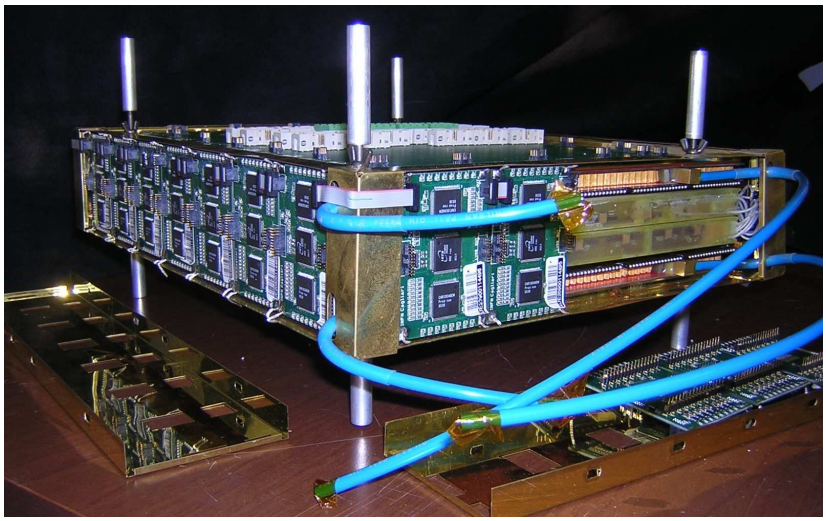

Figure 4.39: An M1R1 station, after the integration of all components: FEE, HV filters and LV cards.

boards (see Sec. 4.4.1), and boards with noisy or dead channels are replaced.
Such controls has been performed again after the transportation at CERN in August 2007, where detectors are stored before the installation on the apparatus, foreseen in the first months of 2008.

4.4 The detector electronics and services

The GEM detectors has a specialized version (CARDIAC-GEM) of the front-end electronics implemented for MWPC of the rest of the muon system, due to the tight space constraints around the beam pipe, that required to include all circuits in only one board, as well as the peculiarities of this kind of detectors, where signals are generated by the fast motions of the electrons, rather than ions as in wire chambers.
For the same reason we developed a custom High Voltage System, that has been preferred for flexibility and safe-operation among several solutions.

4.4.1 The CARDIAC-GEM front-end boards

The CARDIAC-GEM board houses two CARIOCA-GEM amplifier shaper and discriminator (ASD) chips and the DIALOG control chip. A spark protection circuit is implemented at the input stage of the pre-amplifier (Fig. 4.40). All the components are radiation hard since the boards are embedded on the detector, in a region where the total ionising dose foreseen in 10 years of operation can arrive to 5000 Gy and the neutron and hadron fluences are in the range of $10^{13}/cm^2$.
CARIOCA-GEM chips receives analog signals from 8 channels of one of the chambers and produce the discriminated digital signals, with threshold adjustable channel by channel. It has been modified with respect to the standard version implementing an higher amplifier gain and removing the ion tail cancellation circuit [76]: in fact in GEM detectors ions do not contribute to the signal formation, because only electrons through the third GEM arrive in the induction gap.

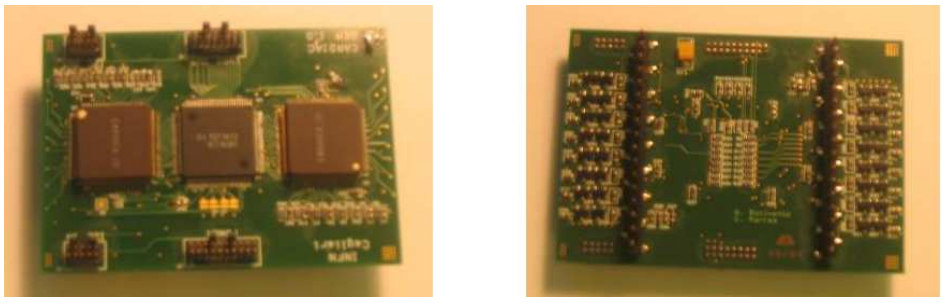

Figure 4.40: Top and bottom view of a CARDIAC-GEM board, showing the two CARIOCA-GEM chips, the DIALOG chip and, on the rear, the spark protection circuits.

The DIALOG chip takes the 16 digital signals coming from the two chambers and performs the *OR* of corresponding physical channels, in order to obtain the logical channel to be sent to LHCb DAQ. It provides the threshold for the CARIOCA-GEM discriminators and is equipped with adjustable delays for every input line in such a way to match in time the various input signals with steps of 1.6 ns. Moreover some monitoring and debugging features such as internal counters, channel masks and pulse generators are included.

An initial issue experimented with this electronics has been the spread of threshold parameters over the different channels, that comes out to be not negligible. The minimum detectable charge depends mainly on the temperature and low voltage variations that are corrected with an online calibration procedure foreseen for all Muon electronics during calibration runs. However the correspondence between such a minimum detectable charge and the equivalent threshold value in voltage, as well as the slope of the correspondence are slightly channel by channel dependant.

For GEM detectors boards we preferred to measure these parameters instead of using their mean values, in order to achieve operation at a lower uniform electronics threshold.

By means of s calibration bench the minimum detectable charge and the slope has been measured and recorded in a database for all CARDIAC-GEM board. The measure has been performed by injecting several fixed charges at the input of the preamplifiers, through a known capacitance that is comparable with the one of a readout pad.

Such a calibration has been very effective, allowing to obtain a noise rate of few tens of Hertz even at threshold down to 2.5 fC (Fig. 4.41).

A lower threshold is of course desirable since it gives the possibility to operate the detectors at a lower gas gain, resulting in a longer lifetime. Taking into account the increased environmental noise that can be found in the experimental area, the operative threshold could be around 3–3.5 fC. In any case, in Sec. 4.6, a measurement at the SPS beam will demonstrate that performance degrades very smoothly up to a threshold of 5 fC.

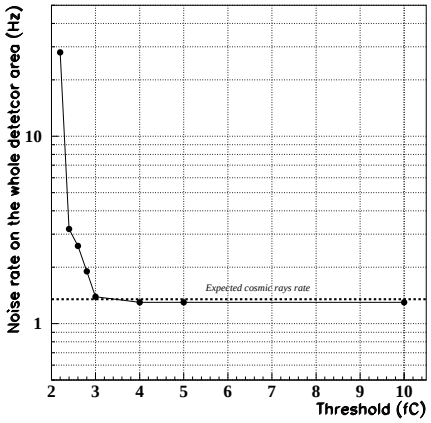

Figure 4.41: The noise rate measured on a station as a function of the FEE threshold.

4.4.2 The High Voltage System

GEM detectors are composed by many electrodes and the high voltage must be supplied with particular care. In fact the voltage of an electrode must be compared with the voltages of the neighbouring electrodes to define the fields in such regions: a too high field can cause discharges, or in case of the two electrodes of a GEM, the breakdown of the kapton dielectric, leading a sector of the GEM to a permanent short.
It must be stressed that the same care on the maximum allowed voltages between electrodes must be taken also during transient phases, such as the ramping up, as well as variations of the HV settings or even the switching off of the detector.
The simple solution of seven independent HV channels must then be designed with a robust control system that moves voltages gradually with the right choice of the HV *ramp-up* and *ramp-down* rates. It has been used during the R&D phase in most of the measurements and the tests on beams.
However this solution has been discarded especially because of the high cost, with any commercially available device.
A safer solution is constituted by a passive divider, as used for GEM detectors of the COMPASS experiment [48]. The disadvantage is less flexibility, because it is not possible to tune a voltage while keeping fixed the others.
A tentative in this direction has been performed using three HV channels and two separate

passive dividers per chamber (Fig. 4.42): the first and the second GEM electrodes were supplied by one divider and the third GEM electrodes were supplied by the other one; the cathode was supplied by the remaining HV channel.

The first issue of this solution is the impossibility to keep fixed transfer and induction fields while tuning the voltage on the GEM foils (Fig. 4.43, top). More serious are the problems of heat dissipation, taking into account the tight space constraints around the beam pipe, introduced by the high currents of the dividers (several mA, see Fig. 4.43, bottom) required to obtain stable voltages on all the electrodes, where currents of few μA are expected during the operation.

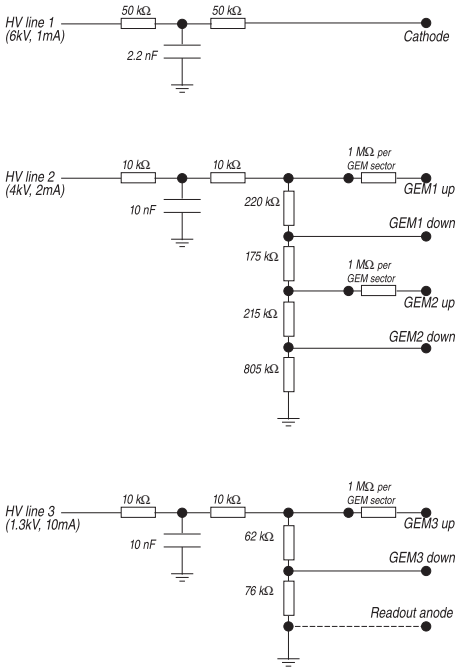

Figure 4.42: Scheme of the HV supply using three HV lines and two dividers.

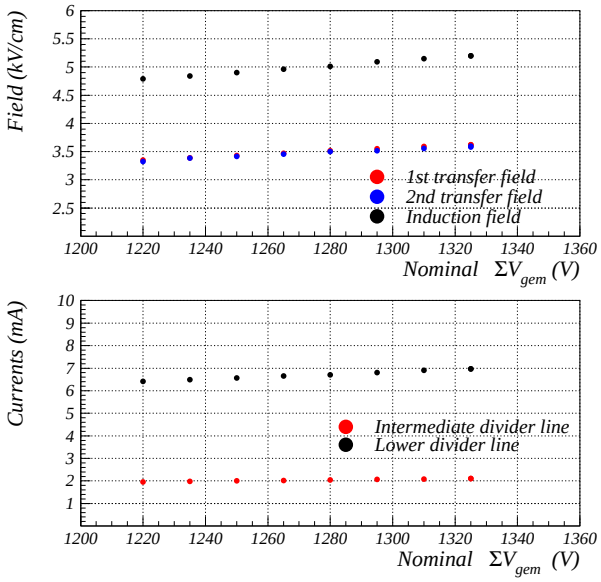

Figure 4.43: (top) Transfer and induction fields behaviour while tuning the voltage settings on the GEM foils. (bottom) The divider current as a function of the voltage settings on the GEM foils.

A completely new and safer solution, based on floating HV channels, has been developed by the LNF electronic pool [77]. The basic module (Fig. 4.44, 4.45) of this device is composed by a chain of seven floating HV channels, whose voltage is always referred to the voltage of the previous channel of the chain and only the third GEM bottom electrode (*G3Down*) is referred to ground.

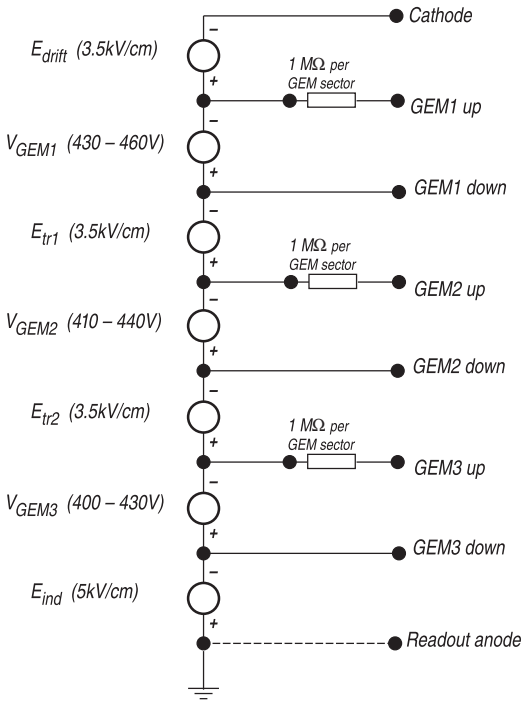

Figure 4.44: Scheme of the new HV device basic module.

Figure 4.45: Picture of the new HV device basic module.

The complete HV crate includes 24 of such modules for the complete M1R1 instrumentation, as well as 24 current-meter modules to monitor with high precision (1nA sensibility) the current on the *G3Down* of each chamber.
This solution allows to finely tune the GEM voltages independently one from each other and from the gap fields, while ensuring a safe operation because the maximum allowed voltage differences are fixed by the hardware itself. In principle the modularity of the whole system allows the fine current monitoring of all the electrodes, but we decided to readout only the one drawn by the *G3Down* that, for our induction field choice (5kV/cm), is practically equal to the current flowing through the readout anode (see Sec. 4.3.2). In addition our choice reduces the cost of the whole system without losing important features.
The HV system will be placed in the control room, so a rad-hard technology is not required. We placed all the HV lines of one station (i.e. 7 HV lines and a ground return line per chamber, 16 total lines) in the same multi-polar cable, that is plugged to the connector situated on one angle bar of the Faraday cage.

4.5 The global irradiation test

In M1R1 region a triple-GEM detector must tolerate, without damage or performance losses, an integrated charge of ~ 1.8 C/cm^2 in 10 years of operation. This value can be calculated assuming to operate the detector at a gain of 6000 and to have an average particle flux of ~ 184 kHz/cm^2 for an average machine luminosity of $\mathcal{L} = 2\times10^{32}$ cm^{-2}s^{-1}; as explained in Sec. 3.7.5, a factor of 2 has been included because we measure the integrated charge as the integral of the sum of the readout and the *G3Down* currents, that are, for our choice of induction field, half of the current produced from the third multiplication stage.
Local aging test on small size detectors (Sec. 3.7.5) demonstrated negligible aging effects ($< 5\%$) with the Ar/CO_2/CF_4 (45/15/40) gas mixture after the integrated charge corresponding to ~ 11 years of operation at LHCb, where an higher rate of 460 kHz/cm^2 was assumed because the average rate was not well known yet. The use of the correct average rate would increase the lifetime estimation of a 2.5 factor, but it should be stressed that such a test involved only 1 mm^2 of the active area of the detector.
A global irradiation test was required to qualify the compatibility of the construction materials (for detector as well as gas system) with the gas mixture, especially for the large amount of CF_4 (40%) that is present.
This test has been performed at the Calliope irradiation facility of the ENEA-Casaccia Laboratory near Rome.

4.5.1 Test setup

The Calliope plant is a *pool type* irradiation facility equipped with a ^{60}Co radioisotope source with an activity, at the time of the test, of $\sim 8\times10^{14}$ Bq. The emitted radiation consists of photons with an energies of 1.17 MeV and 1.33 MeV. .
To reach the integrated charge of 10 years of LHCb operation in the time available for the test (about 35 days), a gamma dose corresponding to m.i.p. flux of about 20 MHz/cm^2 is required, i.e. 100 times the average M1R1 rate. To disentangle from possible misleading results that such an accelerated irradiation can give, we placed several chambers at different position and coverage inside the bunker, obtaining different irradiation rates.
In particular, a full size prototype, called *chamber "C"*, was placed in a low irradiation zone corresponding to ~ 1 MHz/cm^2 m.i.p. rate, and two full size prototype, called *chamber "A"* and *chamber "B"*, in the high irradiation zone corresponding to ~ 15 and ~ 20 MHz/cm^2

respectively. In Fig. 4.46 the Calliope plant, with the arrangement of the chamber inside the irradiation hall, is shown.

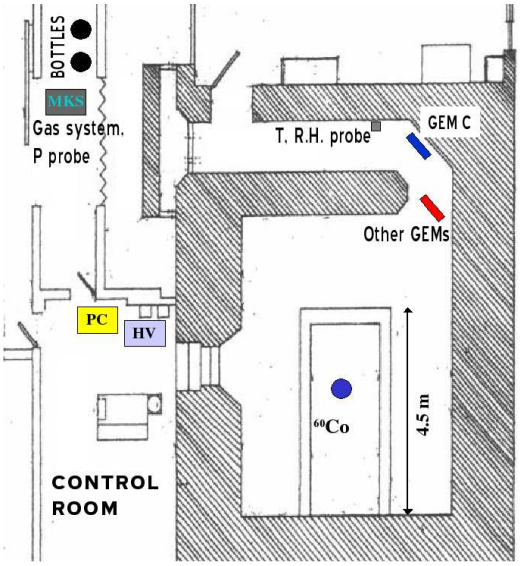

Figure 4.46: Disposition of the chambers in the irradiation hall.

Figure 4.47: Position of the chamber during the test. On top of the blue rack was placed the chamber A and B. On the black rack, where the radiation flux was less intense, was placed the chamber C.

Because of the very high current drawn (400–500 μA) by the detectors in the high irradiation position, to reduce the voltage drop introduced by sector resistors in the GEMs foils, the *chamber A* and the *chamber B* were equipped with 100 kΩ limiting resistors, while standard 1 MΩ limiting resistors have been used for the lowest irradiated chamber C.
Since the high humidity level of the irradiation bunker due to the presence of the water pool,

the gas distribution system was realized with specific materials. The whole gas inlet line was made of stainless-steel tubes, while the exhaust gas line was made of polypropylene tubes (not hygroscopic). The gas flow rate was 350 cm^3/min, to be compared with the single detector volume of $\sim$ 350 cm^3. The lowest irradiated detector was installed upstream in the same gas line of the high irradiated detectors. A probe was directly installed on the gas line, downstream the test chambers, in order to monitor the temperature and humidity of the gas mixture (Fig. 4.48). The water content in the gas mixture was substantially kept under few tens of ppm_V during the whole test. An additional probe supplied the monitor of the atmospheric pressure.

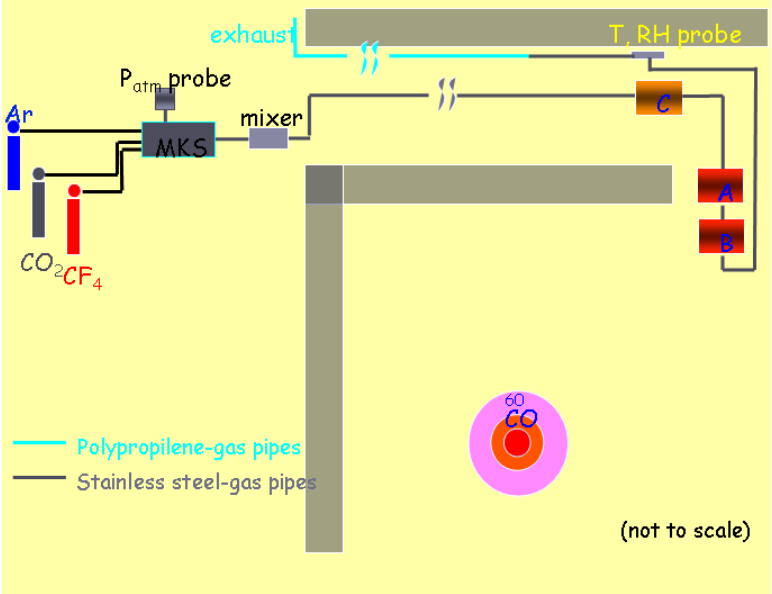

Figure 4.48: Sketch of the gas system.

The temperature and the atmospheric pressure variations were used to correct the gas gain of the chamber, according to the following empirical relation:

$$G \propto e^{<\alpha> V_{GEM}^{tot}} \cdot e^{\beta T/p} \tag{4.1}$$

where the parameters [1] , $<\alpha>$ = 17$\times 10^{-3}$ V^{-1} and β = 40 mbar/K, have been previously measured in laboratory with the X-ray tube.

[1] This formula differs with the one in Sec. 3.7.1 because the T/p variations has been extracted from the Townsend coefficient.

During the test the working voltage was set to V_{GEM}^{tot} = 1280 V, corresponding to a gas gain of $\sim 6\times10^3$ at T = 300 ^{o}K and p = 990 mbar.

4.5.2 Test results

After a period of about 35 days, the total accumulated charges by the three prototypes were ~ 0.16 C/cm^2 for the lowest irradiated detector, ~ 1.6 C/cm^2 and ~ 2.2 C/cm^2 for the highest irradiated ones, corresponding respectively to about 1 (*chamber C*), 8.5 (*chamber B*) and 11.5 (*chamber A*) years of operation at LHCb. At the end of the test *chamber C* has shown no aging, while current drops of ∼89% and ∼80% were observed respectively for chamber A and B, as shown in Fig. 4.49.

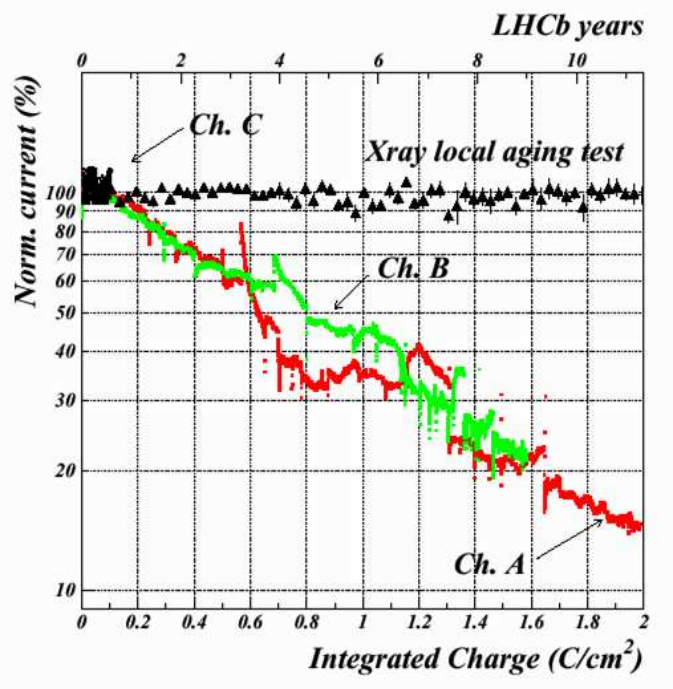

Figure 4.49: Comparison between local aging and the global irradiation test at the ENEA-Casaccia.

The result obtained in this test has been attributed to the insufficient gas flow rate (350 cm^3/min, the maximum available flow of our gas system) with respect to the very high gamma ray flux, that produced a readout current of the order of 400-500 μA. On the contrary, local aging tests were performed in completely different experimental conditions: a gas flow rate of

100 cm^3/min for a global detector current of 0.4-0.2 μA (over an irradiated area of the order of 1 mm^2).
Hints in this direction were given by the fact that *chamber C*, upstream in the gas line and exposed to a lower irradiation, didn't show any current drop. Moreover partial recovers were observed on detectors downstream in the gas line, when upstream detectors are switched off, or also when a detector was switched on again after being off for some time.
In this framework we believe that the global irradiation test has been performed in strong *gas pollution* conditions and then should be considered pessimistic and misleading. The measurements on aged chambers presented in the following sections support this hypothesis. Also the process that originates this result has been understood: chambers were submitted to a strong plasma etching by fluorine, produced in the fragmentation of the CF_4, and not quickly removed by the gas flow.

4.5.3 Gain and rate capability measurements on aged chambers

The gain of the irradiated detectors has been measured with the X-ray tube at a relatively low particle flux of $\sim$ 1.6 MHz/cm^2.
In Fig. 4.50 is shown the comparison between the effective gain of the chambers before (empty circles) and after (full triangles for chamber A, full squares for chamber B) the global irradiation test. The gain reduction is $\simeq$ 55% for chamber A, and $\simeq$ 32% for chamber B. In addition, as shown in Fig. 4.51, the chambers A and B exhibit a considerable rate capability reduction at high particle fluxes (a rate capability greater than 50MHz/cm^2 is measured on new detectors). In particular, a simple linear extrapolation of the last two measured points (full circles) up to the particles fluxes at which the chamber A has been operated during the global irradiation test (15 MHz/cm^2), indicates a gain drop of $\sim$ 30% ($\sim$ 40% for chamber B, considering the same loss of linearity of the rate capability of chamber A).
These results are compatible with the current drops observed at the global irradiation test and are summarized in Tab. 4.4. In fact, for chamber A the gain drop of 55% at low rate, and the loss of linearity of the rate capability at 15 MHz/cm^2 of 30%, can explain the current drop of 89% .
It should be stressed that the rate capability is still greater than 3 MHz/cm^2, well above the LHCb requirements for M1R1 (the maximum particle flux in M1R1 is $\sim$ 500 kHz/cm^2).

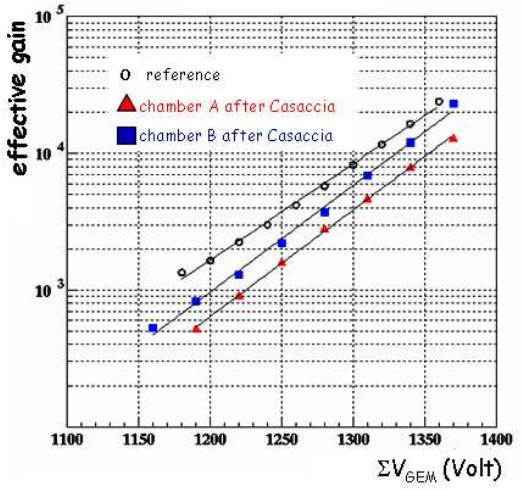

Figure 4.50: Comparison between the gain measured on a new GEM detector and the gain measured on chamber A and B after the Casaccia aging test.

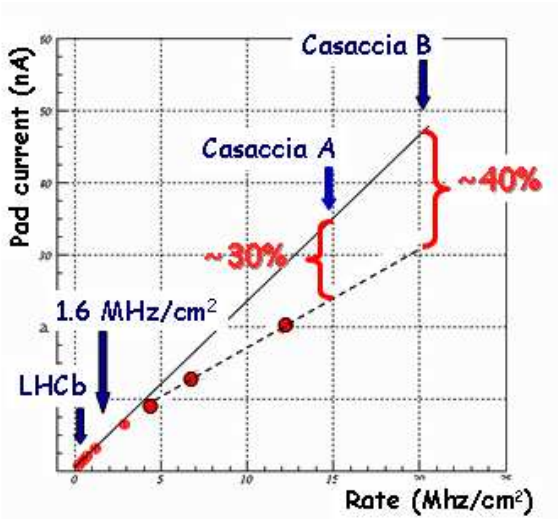

Figure 4.51: Rate capability loss of aged chamber A and B.

	Chamber A	Chamber B
Gain reduction	$\sim 55\%$	$\sim 32\%$
Rate reduction	$\sim 30\%$	$\sim 40\%$
Total reduction	$\sim 85\%$	$\sim 70\%$

Table 4.4: Summary table of the gas gain and rate reduction performed with the X-ray tube. The sum of the two effects is comparable with the gain drop observed at the end of Casaccia test.

4.5.4 Beam test results on aged chambers

The performance of the two chambers, A and B, was measured at the electron beam facility (BTF) at LNF before the irradiation, and after that it has been again measured at the PS beam facility at CERN. Both tests have been performed at a particle flux of ~ 100 kHz/cm^2, close to the average particle flux expected at the LHCb experiment.
The comparison of the results shows that aged chambers practically maintain the same performance in terms of efficiency in 20 ns time window, except for a moderate shift of the working points toward higher voltages. For chamber A the shift of the operating voltage, Fig. 4.52 (top), is about 15 V, while for chamber B the shift is negligible. For a station made with these two detectors logically OR-ed, the efficiency in 20 ns time window is practically unaffected, Fig. 4.52 (bottom).

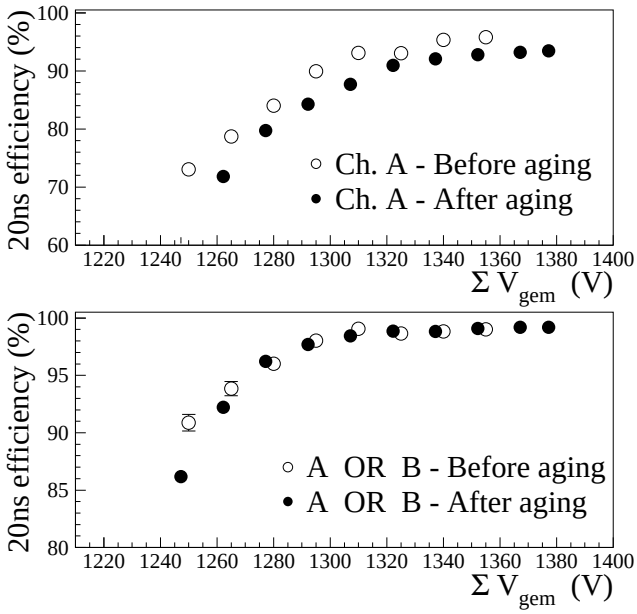

Figure 4.52: Efficiency in 20 ns time window before and after irradiation: (top) for chamber A; (bottom) for the two chambers logically OR-ed

This result points out the robustness of this kind of detector: even in such a hostile environment, where for example in a MWPC a wire could break, making impossible the operation because of the short between the cut wire and the cathode, a GEM detector can still work with slightly reduced performance.

4.5.5 SEM analysis and X-ray spectroscopy on aged chambers

In order to understand the mechanism occurred during the global irradiation test, a scanning electron microscope (SEM) analysis has been performed on various samples of the aged chambers.
Pictures in Fig. 4.53 and Fig. 4.54 demonstrated a fluorine etching of the internal profile of the GEM holes.

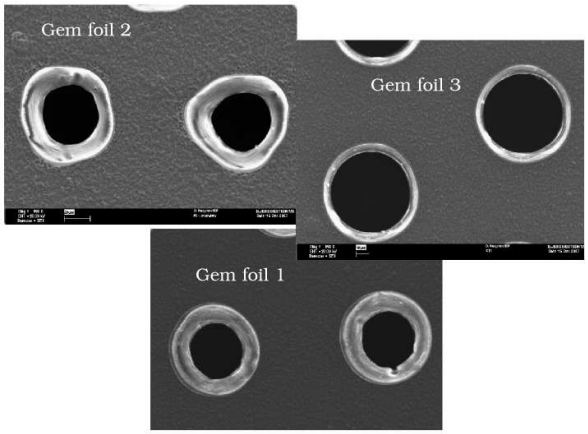

Figure 4.53: Picture of the three gem foils. The widening of the holes from the first to the third foil is visible.

As expected the etching effects are larger on the third GEM foil, minor effects are found on the second GEM, while the first GEM does not present any appreciable etching effects.

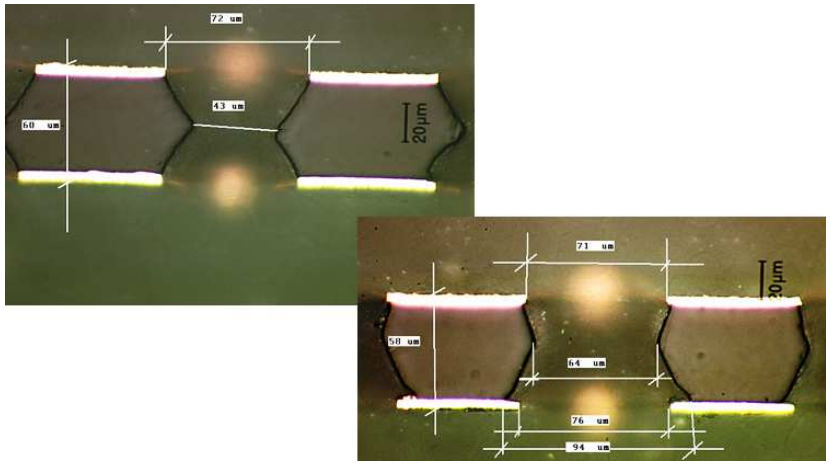

Figure 4.54: Cross section of first GEM foil (left), practically as new, and third GEM foil (right) of chamber A.

On second as well as third GEMs the observed effect consists of a appreciable widening of the external (copper) holes diameter, from the standard 70 μm up to 80 μm. In addition on the third GEM, where the etching processes were clearly larger, also the kapton inside holes has been etched: the internal hole diameter from the standard 45-50 μm becomes 60-65 μm.

Fluorine has been found on the bottom surface (where negative ions and electrons are collected) of the third and second GEM, being larger on the third GEM. In Fig. 4.55 the comparison between the X-ray spectra measured on the bottom surfaces of the three GEM foils are shown.

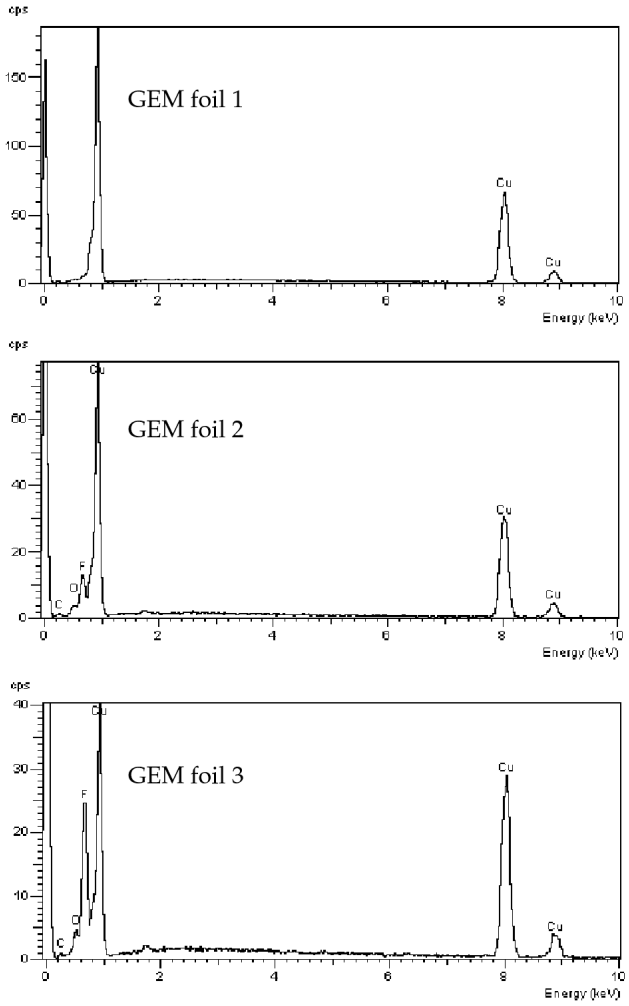

Figure 4.55: X-ray spectroscopy of the bottom surfaces of the three GEM foils of chamber A: no fluorine on the first GEM foil, small deposit on the second GEM foil and larger deposit on the third GEM foil.

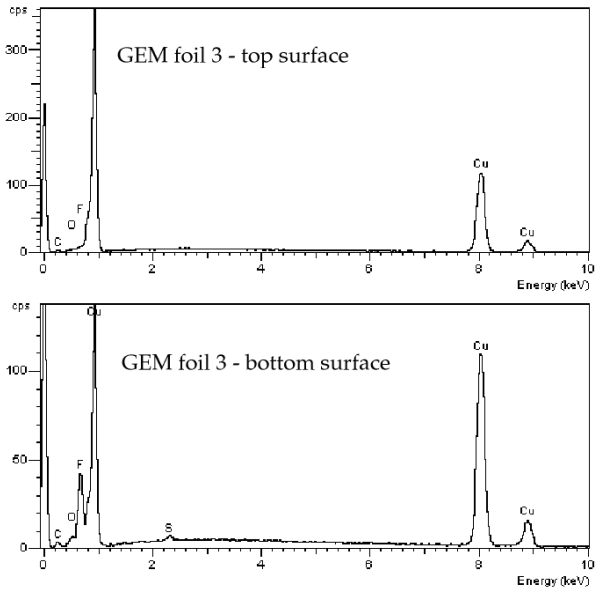

Figure 4.56: X-ray spectroscopy of the third GEM surfaces (top and bottom respectively) near the hole edge shows presence of fluorine only on the bottom surface.

Fluorine is mostly located on the copper around the holes edge, leading to the formation of a thin non conductive layer (a fluorine-copper compound). The Fig. 4.56, where the comparison between the X-ray spectroscopy of the top and bottom surfaces of the third GEM foil of the Chamber A is shown, demonstrated that such a mechanism does not involve the GEM top surfaces.

Fig. 4.57, 4.58 and 4.59 the compare the etching effects found on the third GEM foils of the two chambers (A and B respectively). The holes of chamber A are clearly more etched than those of chamber B, as well as a larger fluorine deposit is observed. During the global irradiation test chamber A accumulated the largest quantity of charge (~ 2.2 C/cm^2).
On the contrary cathodes (drift electrode) as well as anodes (the pad PCB) were found perfectly clean.

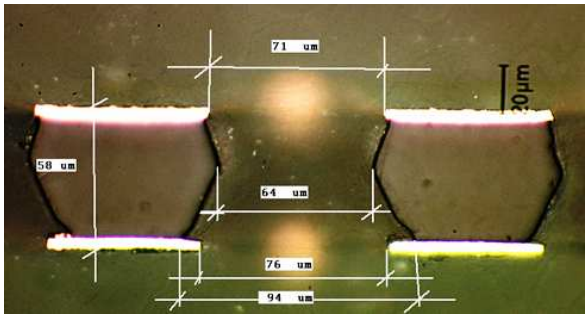

Figure 4.57: Cross section of third GEM foils of the chamber A.

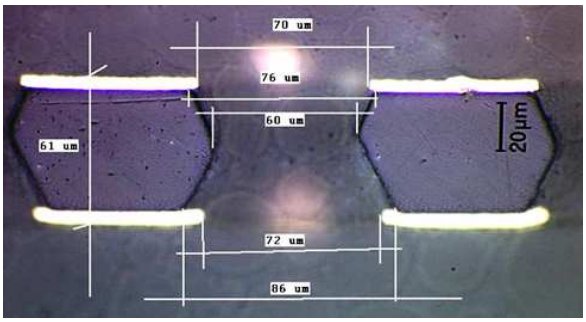

Figure 4.58: Cross section of third GEM foils of the chamber B.

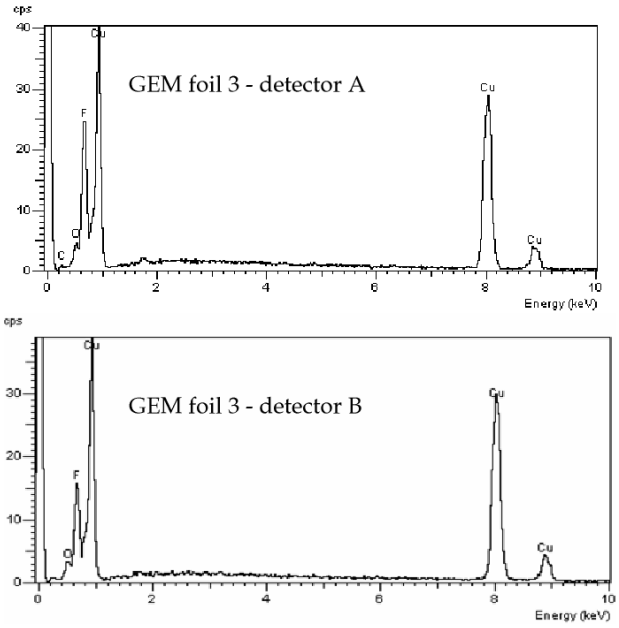

Figure 4.59: Comparison between the X-ray spectroscopy of the bottom surfaces third GEM foils, of the chambers A and B; larger fluorine deposit has been found on chamber A.

The results of the SEM analysis give a reasonable explanation of the observed effects:

- the enlargement of GEM holes leads to a decrease of the gas gain [55];
- the etching of the kapton inside the holes and the non conductive layer on the copper near the hole edge lead to enhanced charging-up effects, reducing the rate capability of the detector.

Finally, in order to demonstrate that the etching observed at the global irradiation test was essentially due to an insufficient gas flow rate compared with the high irradiation level, we reproduced such conditions irradiating with a high intensity X-rays beam a 10×10 cm^2 prototype, flushed with a reduced gas flow, Fig. 4.60. The current drawn by the chamber was about 1 μA on a 1 cm^2 irradiated area, while the gas flow was $\sim$ 20 cm^3/min. In such conditions we observe a permanent gain drop of about 40% in $\sim$3 LHCb equivalent years.
The test, repeated with a gas flow of $\sim$ 200 cm^3/min and with a current of 0.5 μA on a 1 cm^2 irradiated area, gave a result compatible with no aging in about 10 LHCb equivalent years.

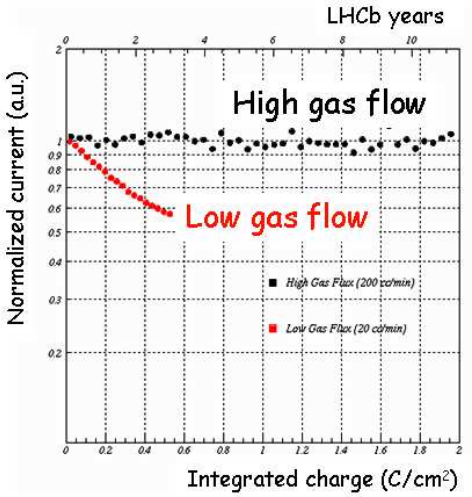

Figure 4.60: Comparison between the aging measured on a small prototype with low gas flow ($\sim$ 20 cm^3/min) and high gas flow ($\sim$ 200 cm^3/min).

4.5.6 Global ageing test conclusion

The results of the severe and systematic tests performed on triple-GEM detectors, indicate that the detector is robust and can tolerate the radiation dose foreseen in 10 years of operation in the region M1R1 of the LHCb experiment: detectors, even after a severe irradiation in very bad conditions, exhibit good time and efficiency (in 20 ns) performances, except for a shift of about 15 V on the working point for a single detector, while for two detector logically OR-ed the performances are practically unchanged.
In addition the results of the global irradiation test, apparently in disagreement with the other aging tests previously performed, have been understood. We have demonstrated that the etching observed during this test is clearly correlated with bad gas flow rate conditions. No etching occurs if the gas flow is properly set. In the LHCb running conditions, where the average current collected on pads by one full size chamber will be of the order of 5μA, a safe gas flow rate could be $\sim$ 80–100 cm^3/min, flushing all stations in parallel with its own gas line.

4.6 The detector performance at the SPS 40MHz beam

The performance of a detector fully integrated with CARDIAC-GEM electronics has been measured in October 2006 at the SPS beam at CERN. The SPS beam (180 GeV/c pions and muons) has been set up with a 25 ns bunch crossings time structure, and the data-taking has been performed with the official LHCb DAQ electronics and logic.
This generalized test involved also people from the MWPC group and other LHCb groups (in particular online, electronics, muon trigger), and the lessons learnt during the preparation has been very useful for the commissioning in the apparatus.

4.6.1 Test setup

The setup of the test has been designed in order to simulate the LHCb running condition, reproducing the LHC bunch crossing time structure and as much as possible many of the final characteristics of the experimental apparatus, such as the data-taking DAQ chain, the cable length and the grounding scheme.
We used one of the detectors built for the experiment, and all FEE boards has been previously calibrated as described in Sec. 4.4.1.
In Fig. 4.61 the position of the detector along the beam line is shown.
Two plastic scintillators have been placed in front of the detector for trigger purpose. In fact the LHCb DAQ chain write events on disk following the trigger scheme, so that for the test we provided an external trigger from the coincidence of the two scintillators. Without entering in the details of each component, the LHCb DAQ allows to record the detector information related to the bunch crossing corresponding to the external trigger, as well as bunch crossings before or after that, up to a maximum of 13 bunch crossings per trigger.
To record all the 13 consecutive bunch crossings, a reduction of the trigger rate was also required due to the limited bandwidth of the standard computer at the end of the DAQ chain, where data were at last written: with the introduction of a dead time in the external trigger generation, the trigger rate was decreased from about 10 kHz to $\sim$ 4 kHz.
The information collected from the detector, for each channel and bunch crossing, was a *4 bit word* encoding the arrival time of the hit *inside the 25 ns bunch crossing width*, i.e. the finest time resolution of the system was about 1.6 ns.
The SPS beam, composed by 180 GeV/c negative pions and muons on a spot of 4×4 cm^2,

Figure 4.61: The GEM detector position along the beam line. In front of the detector two scintillator has been placed to to compose the trigger.

had a time structure as shown in Fig. 4.62.
It was structured in *spills* of about 2 seconds every 12 seconds, that contain about 96 thousand *bursts* of 48 consecutive 25 ns wide bunch crossings. Signals from the machine allowed the synchronization of the DAQ with the bunch crossing structure.

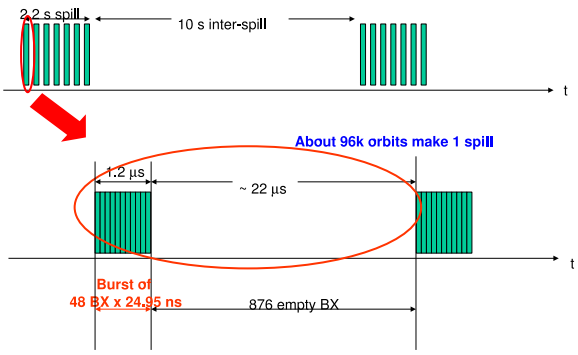

Figure 4.62: Beam time structure. During the *spill*, that last for about 2 seconds every 12 seconds, about 96 thousand *bursts* of 48 consecutive bunch crossings are present.

4.6.2 Time synchronization of detector signals

The synchronization of detector signals has been operated with the DAQ electronics (*coarse time alignment*) as well as the front-end electronics on the chamber (*fine time alignment*). The DAQ chain allows to delay or anticipate the signal in unit of bunch crossing, assigning the proper *bunch crossing number* to the data. According to a rough evaluation based on cable length, the bunch crossing where data were estimated to be has been placed in the middle of the 13 recordable bunch crossings per trigger. The corresponding time spread (over 300 ns) has been enough to find the right bunch crossing, that has then been shifted to the third slot of the sequence, in order to check detector behaviour up to about 250 ns after the event. The operation resulted rather simple since all cables lengths were equal, and a delay of about 2 bunch crossings had to be corrected only in GEM detector channels (Fig. 4.63) to take into account for the transit time of electrons through the two transfer gaps of the GEM detectors.

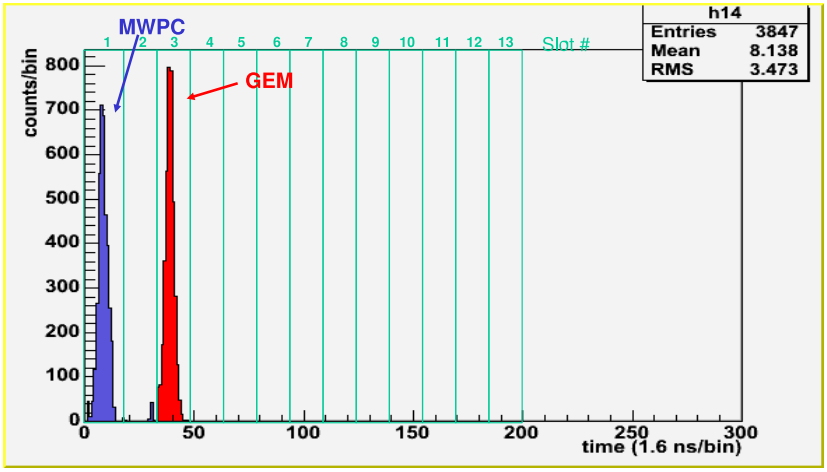

Figure 4.63: The GEM detector and MWPC signals after a first alignment step. In the next step both detectors signal will be shifted in the third bunch crossing of the sequence.

As explained in Sec. 4.4.1, the fine time alignment is performed by the CARDIAC FEE. The boards allow to delay signals up to 31 steps of 1.6 ns, corresponding to two bunch crossings. The delay acts on physical channels, so that in principle it could be applied to improve the alignment of the two physical channels before composing the *logical OR*, but the symmetry in the design of the two chambers composing the station gives itself a good time alignment. Indeed we found all channels of the station already well aligned each other, since the readout

PCB traces have all almost the same length.
On the other hand, as already observed in previous tests on beam, the hit time is shifted in advance for higher gains, or, equivalently, for lower electronics threshold, because the signal requires the contribution of fewer primary clusters to be over threshold.
To avoid to perform the fine alignment task analysing data on disk, the DAQ itself provides a histogramming functionality to monitor the hit arrival time inside the bunch crossing, as shown in Fig. 4.64.

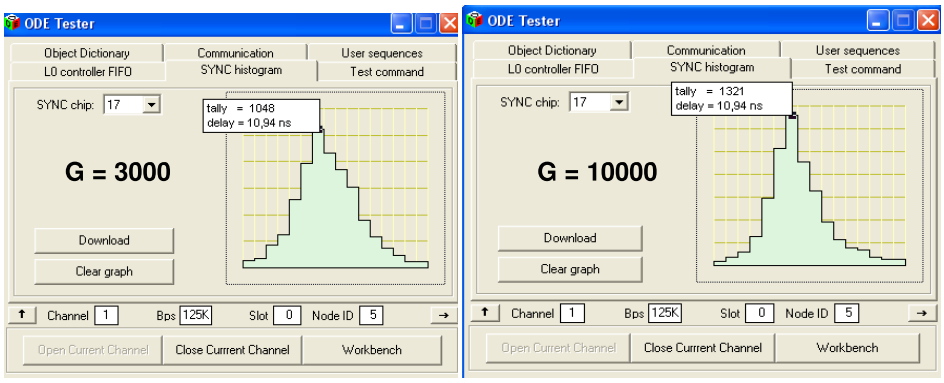

Figure 4.64: The hit time arrival inside the bunch crossing as monitored by the DAQ histogramming functionality, for two gain configurations. For each gain configuration, channels are delayed in order to have the peak of the distribution in the middle of the bunch crossing.

This functionality has been used to move the peak of the time distributions in the middle of the bunch crossing, for each gain and threshold configuration [2].

[2]For the experiment data-taking, all the possible configurations will be recorded in a *condition database*.

4.6.3 Test results

The performance of the detector has been measured in terms of efficiency *inside the bunch crossing time window*, and the pad cluster size inside the expected *field of interest* (FOI) of the M1R1 region (see Sec. 2.4), i.e. ± 2 pads.
The definition of 20 ns time window was a conservative constraint to take into account for difficulties in the time alignment procedure. In this case the detector efficiency as well as the effectiveness of the time alignment procedure were measured together.

A preliminary set of measurements for various FEE threshold settings was performed keeping the detector gain fixed at 6000 (Fig. 4.65).

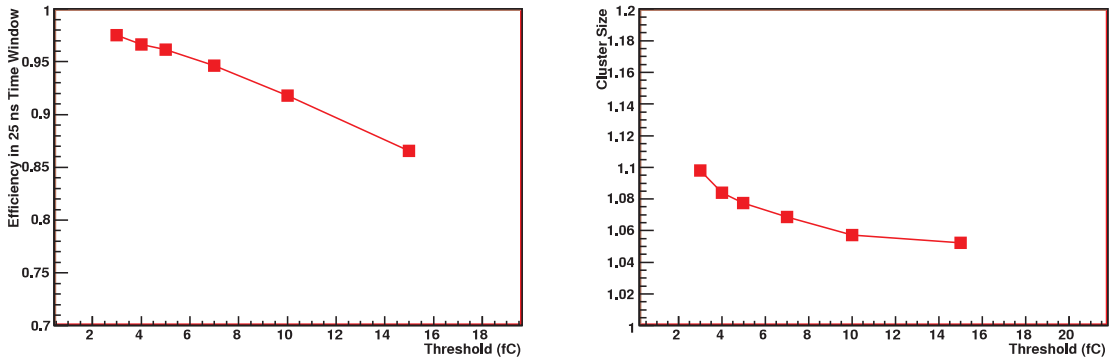

Figure 4.65: Efficiency inside the bunch time crossing (left) and pad cluster size (right) as a function of FEE threshold, at a fixed detector gain of 6000.

The FEE threshold set to 3 fC demonstrated to be a good working point that allowed also to have a negligible electronics noise (few Hz on almost all channels, with about 100 Hz on three noisy channels); in case of an increased noise environment in the experimental pit, such a setting can be increased as well up to 5 fC, still fulfilling the experiment requirements.
The initial gain of 6000 was chosen since it had been the beginning of the detector operational *plateau* in all the previous tests, but the detector gain and the FEE threshold are obviously correlated: in fact a higher gain allows to obtain the same performance even at higher thresholds, but on the other hand it increases the global noise and the pad cluster size parameter at too low thresholds.

For this reason the FEE threshold has been fixed at 3 fC, and the performance of the station, as well as the one of each single chamber, has been studied as a function of detector gain. In Fig. 4.66 and Fig. 4.67 the efficiency inside the bunch crossing and the cluster size inside the FOI are shown.

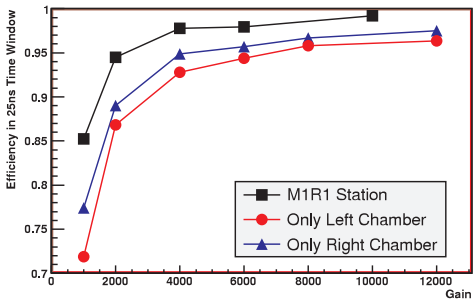

Figure 4.66: Efficiency inside the bunch crossing time width (25 ns), as a function of the detector gain.

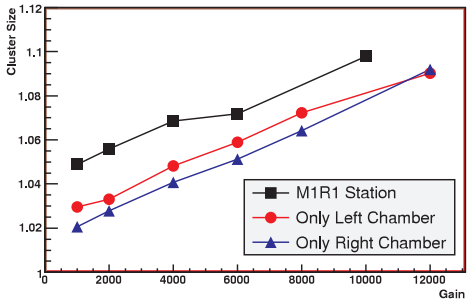

Figure 4.67: Pad cluster size in the field of interest of M1R1, i.e. ± 2 pads, as a function of the detector gain.

The results demonstrated the beginning of the operational plateau is at detector gain of 4000, to be compared with the value of 6000 as measured in previous tests. This improvement is due to the modifications applied to the new CARDIAC-GEM front-end electronics (see Sec. 4.4.1), as well as the effectiveness of the time alignment procedure.
This is an important result, because the operation with a lower gain allows safer working conditions and a longer detector lifetime.

4.7 Conclusions

The results presented in this chapter demonstrate that GEM detectors operated with the fast $Ar/CO_2/CF_4$ (45/14/40) gas mixture are the right choice for the instrumentation of the harsh environment of the M1R1 region of the LHCb experiment.

The full size detector, constituted by two coupled 20×24 cm^2 Triple-GEM chambers, has been designed taking into account the tight space constraints around the beam pipe of the region. The definition of detailed construction procedure, as well as the severe quality controls, allowed the production of 12 fully instrumented detectors for the experiment and 6 additional spare detectors.

The irradiation test at the ENEA-Casaccia validated the compatibility of the construction materials with the gas mixture under strong irradiation, and the radiation hardness of the detector ensures more than 10 years of operation at LHCb environment.

The performance of a fully integrated detector, equipped with the new CARDIAC-GEM front-end electronics, has been measured in a recent test at the SPS beam at CERN, where LHCb running conditions in terms of beam time structure and data-taking have been simulated. The results demonstrate that the LHCb requirements are fulfilled even at a lower gain with respect to previous measurements, leading to a safer running condition and a longer lifetime of the detector in the experiment.

The production and the quality controls have been completed in June 2007 and now detectors are at CERN waiting for the installation of M1 detectors, scheduled for the first months of 2008.

Chapter 5

A selection of the dimuon rare D^0 decay at LHCb

The remarkable success of the Standard Model (SM) in describing all experimental information currently available suggests that deviations from it can be found either in higher energy scales or in small effects in low energy observables.
The absence of flavor changing neutral currents (FCNC) at tree level in the SM implies that processes involving these currents are a primary test of the theory.
Most of the attention in this direction has been focused on processes involving K and B mesons, while the analogous FCNC processes in the charm sector have received considerably less scrutiny, due to the fact that the SM expectations are very small.
Nevertheless the contributions that some extensions of the SM can give to such processes, leading sometimes to orders of magnitude enhancements with respect to SM, has been reported in recent papers and a review of these studies can be found in [79].
In this chapter the possibilities of a selection of the rare $D^0 \to \mu^+\mu^-$ decay at LHCb experiment is investigated. The selection can exploit the very high rapidity coverage of the apparatus and the lower P_T trigger setting with respect to the other LHC experiments; even if the experiment is optimized for *b* physics, the expected charm production is about seven times more copious, thus compensating a lower efficiency.

5.1 $D^0 \to \mu^+\mu^-$ in Standard Model and beyond

The $D^0 \to \mu^+\mu^-$, as Flavour Changing Neutral Current (FCNC) process, is forbidden at tree level in the Standard Model (SM). Contributions to this decay comes from higher order processes, such as the box diagram in Fig. 5.1.

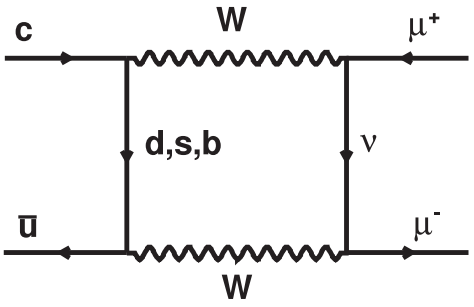

Figure 5.1: Box diagram allowing the $D^0 \to \mu^+\mu^-$ decay in SM.

In contrast with K and B processes, where the top quark is present in the loops, the D meson FCNC transitions involve the rather light down-quark sector which translates into an efficient GIM cancellation. In fact the O(α_s) corrected calculation [80] gives a poor branching ratio for this decay of the order of 10^{-18}.
A recent work [79] has calculated the contributions of intermediate state processes such as the ones shown in Fig. 5.2.

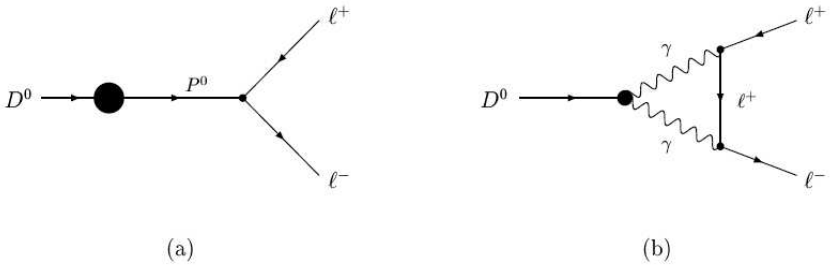

Figure 5.2: Contribution to the $D^0 \to \mu^+\mu^-$ decay in SM through intermediate states such as a resonance (a) or two photons (b).

In particular the main enhancement comes from the two photon diagram contribution, and the largest estimation in SM is a branching ratio of at least 3×10^{-13}. However such a value is still too small to be measured, and several experiment have only fixed an upper limit to the branching ratio.
Actually the best limit has been set by the BABAR collaboration [81] at:

$$\mathcal{BR}_{D^0 \to \mu^+\mu^-} \; < \; 1.3 \times 10^{-6} \;\; (\, 90\% \text{ C.L. })$$

On the other hand, in the same work is shown that several extension of the SM can further enhance the branching ratio, allowing generally an increase of two or three orders of magnitude. The expected branching ratio in several of such scenarios is shown in Tab. 5.1, in comparison with the expected branching ratio in SM and the current experimental limit.

Theoretical model	Expected $\mathcal{BR}$
Standard Model	3×10^{-13}
MSSM , $\mathcal{R}$-Parity violation	3.5×10^{-6}
Multiple Highs Doublets	8×10^{-10}
Horizontal Gauge Models	3×10^{-11}
Extra fermions	3×10^{-11}
Experimental limit	1.3×10^{-6}

Table 5.1: The expected branching ratio of the rare $D^0 \to \mu^+\mu^-$ decay in several scenarios [79] and the current experimental limit [81].

In many cases the value is still very small, but an improvement of the upper limit translates into constraints in the parameters of the theory. The most interesting case is a Minimal Supersimmetric Standard Model (MSSM) with the R-parity violation. In this scenario the expected branching ratio can arrive up to the order of 10^{-6}, i.e. the actual experimental limit is already constraining the parameters of the model.

Such that, the charm sector seems an interesting field able to give complementary information with respect to the one obtained in K or B mesons process.

5.2 Selection strategy at the LHCb experiment

The LHCb experiment is designed for the selection of B mesons, which are characterized by secondary decay vertices separated by the primary vertex. This is due to the lifetime of such particles ($\sim 10^{-12}$ s) that translates in a mean decay length of about 7 mm, for a momentum of 80 GeV/c. A D^0 meson with such a momentum has as well a mean decay length of about 5 mm, so the same strategy can be used in the selection.
A sketch of the decay kinematics is shown in Fig. 5.3.

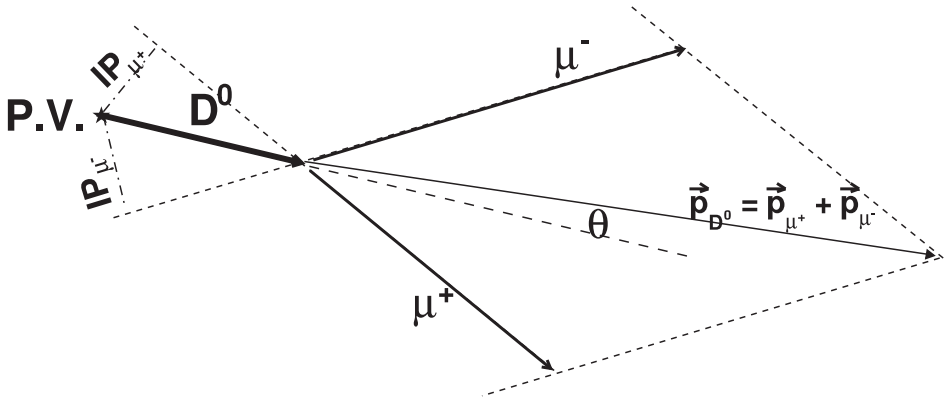

Figure 5.3: Kinematics of $D^0 \to \mu^+\mu^-$ decay.

Separated vertices are detected by requiring a high impact parameter of the daughter muons ($\text{IP}_{\mu^\pm}$), as well as measuring the distance of the D^0 decay vertex, reconstructed from the daughter muons, from the primary vertex assumed as the D^0 origin. Other quite common cuts on kinematics are: the angle θ between the D^0 momentum (as sum of the daughter muons momenta) and the D^0 flight direction (built connecting the origin and decay vertices); the D^0 invariant mass; the χ^2 of the D^0 decay vertex; the D^0 impact parameter with respect to the primary vertex.
The main disadvantage with respect to the corresponding B_s decay is the lower mass of the D^0, because the reconstruction of the invariant mass is more subject to be confused with the combinatorial background, and a too high cut on the transverse momentum of the candidates can more likely degrade also the signal. The muons misidentification is very low at LHCb

(*mis-id*$_{\mu-\pi} \sim 1\%$), and tighter cuts can also be used for the muon hypothesis; in any case the combinatorial background of the muons present in the event remains the main source of noise in this analysis.

It must be stressed that only D^0-*prompt*, i.e. D^0 mesons originated in the primary vertex (directly or through resonances), are selected in this manner. As a first approach to this study, this choice seems to us more profitable since it covers a large fraction of D^0 production: in fact the expected D (charged and neutral) mesons *prompt* production is about 1.5 mb, to be compared with the 3.5 mb $c\overline{c}$ total cross section.
As a future development, *"secondary"* D^0 can also be taken into account, and the same analysis approach can be used providing to substitute the primary vertex with the decay vertex of the mother particle.
The most suitable mother particle for such a development is the charged $D^*(2010)$, as it largely decays in $D^0\pi^{\pm}$ ($\sim$ 67.7% [82]). In addition it includes also a fraction of the D^0-*prompt*, because it is a resonance ($\tau \sim 10^{-21}$) and its decay vertex is practically coincident with the primary vertex or, if the case the decay vertex of its mother particle. For this reason it can be also a useful tool to reduce the combinatorial background, because an additional constraints is the D^* – D^0 mass difference. On the other hand the detection of the soft pion must be investigated.

5.3 The LHCb software framework

The LHCb software follows an architecture-centric approach based on Gaudi [83], which is a general Object Oriented framework. Typical phases of particle physics data processing have been encapsulated in four C++ based applications, which execute the following tasks:

1. Monte Carlo generation and simulation through the detector (Gauss);
2. digitalization of the detector response (Boole);
3. reconstruction of the event, track finding and particle identification (Brunel);
4. offline analysis (DaVinci).

Each application is producer and/or consumer of data for the other stages, communicating via the LHCb Event model and making use of the LHCb unique detector description, as shown in Fig. 5.4. External programs such as Pythia [84] and Geant [85] are used by the applications to perform specific purposes.

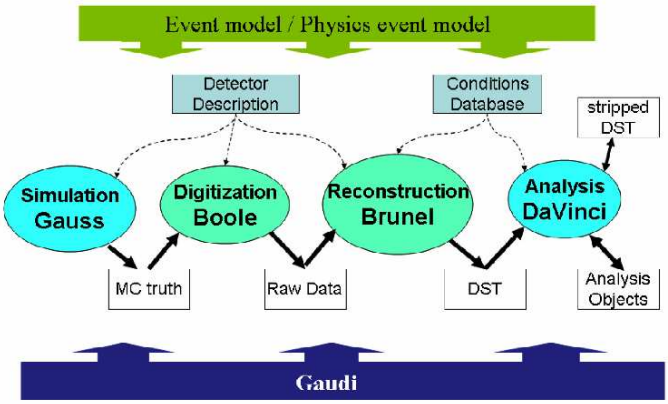

Figure 5.4: The LHCb data processing applications and data flow. Underlying all of the applications is the Gaudi framework and the event model describes the data expected. The arrows represent input/output data.

In the last two steps (Brunel and DaVinci), the simulated events are processed as if they were real data, i.e. without using any information from the so-called Monte Carlo truth. This information can only be used to assess the performances of the different reconstruction and selection algorithms. Fig. 5.5 shows the various stored informations during the processing of an event, from the generation to the analysis phases.

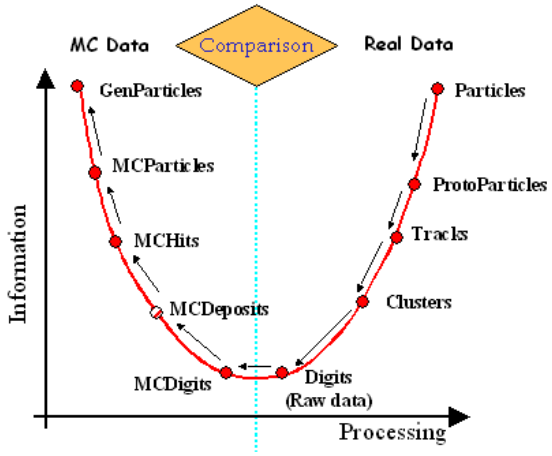

Figure 5.5: Sketch of the stored information during the processing of a event.

5.3.1 Event generation

The generation of the event is performed by the C++ program *Gauss*. It simulates the behavior of the spectrometer allowing to understand the experimental conditions and performances. It integrates two independent phases, *generation* and *simulation*, that can be run together or separately.

The first phase, provided by Pythia (the standard event generator in high energy physics), consists of the event generation of proton-proton collisions at $\sqrt{s}$ = 14 TeV.
For most of the Monte Carlo samples, Pythia generate a generic event (the so called *minimum bias*, corresponding to the total cross section of about 100 mb) from the proton-proton collision, taking into account the processes in Tab. 5.2. If the generated event satisfy the sample criteria, it is accepted and will be processed by the simulation phase. Taking into account the peculiar single-arm spectrometer layout of the LHCb experiment, practically all the Monte Carlo samples request the presence of the particles of interest inside the LHCb acceptance.

The second phase of Gauss consists of the tracking in the LHCb detector of the particles produced by the generator phase. The simulation of the physics processes, which the particles undergo when traveling through the apparatus materials, is delegated to the Geant4 tool [85]. The detector geometry and materials are described in detail, including the active

$f + f' \to f + f'$ (QCD)	Elastic scattering	$g + g \to J/\Psi + g$
$f + \overline{f} \to f' + \overline{f'}$	Single diffractive (AB -> XB)	$g + g \to \chi_{0c} + g$
$f + \overline{f} \to g + g$	Single diffractive (AB -> AX)	$g + g \to \chi_{1c} + g$
$f + g \to f + g$	Double diffractive	$g + g \to \chi_{2c} + g$
$g + g \to f + \overline{f}$	Low-pT scattering	$g + g \to J/\Psi + \gamma$
$g + g \to g + g$		

Table 5.2: Elementary processes used by PYTHIA in the standard LHCb settings.

detection components and their front-end electronics, passive materials such as the beam-pipe, frames, supports and shielding elements. In this phase, all the hits of each particle traversing a sensitive detection layer are registered, together with its energy loss in that layer and its time-of-flight with respect to the primary interaction time. Low-energy particles, mainly produced in secondary interactions, are also traced, down to an energy cut-off of 10 MeV for hadrons and 1 MeV for electrons and photons.
The output of Gauss is a file that contains C++ objects describing the products of the simulation, such as *MCParticles*, *MCVertices*, *MCHits* and *MCDeposits* (see Fig. 5.5).
Moreover the application produces several statistical information: the ratio of the accepted events and the total number of the generated event is the so called *generation efficiency*.

The experiment manages centrally the official Monte Carlo production and the samples for this analysis are part of the official LHCb production.
Two major centralized production has been performed in 2004 and in 2006, called *DC04* and *DC06*. The study on $D^0 \to \mu^+\mu^-$ selection has been performed in both cases: since the analysis approach as well as the results are very similar, I will present only the newest analysis on DC06, where the detector description is more accurate and the software tools are more refined.
The DC06 $D^0 \to \mu^+\mu^-$ signal sample has been generated forcing one of the D^0 of the event to decay in two muons, and the event is accepted and simulated through the detector if such muons are inside the 400 mrad official LHCb acceptance.
As explained in the previous section, the more problematic background comes from the muons combinatorial that could reconstruct the D^0 mass. For this reason an inclusive b sample with the presence of at least two muons has been take into account, not being available

Monte Carlo sample	equivalent cross section	events in sample
$D^0 \to \mu^+\mu^-$ (muons in 400 mrad)	634.3 μb $\times\mathcal{BR}$	62157
inclusive b (>2 muons in 400 mrad)	6.5 μb	13516015

Table 5.3: DC06 Monte Carlo samples for the analysis, with event statistics and generation efficiency.

a similar sample of inclusive c events. The two muons required in the event don't come necessarily from the b decays, but they must be in the above mentioned acceptance.
Table 5.3 summarize the number of accepted events in each sample, as well as the *equivalent generation cross section*, calculated from the total cross section taking into account the generation efficiency for that kind of sample.

5.3.2 Event digitization

The digitization of the event is performed by the C++ program Boole and represents the final stage of the LHCb simulation.
In this phase, the informations coming from Gauss are used to generate digitized hits, taking into account the details of the sensitivity and the response of each sub-detector, where detection efficiency, space and time resolution are adapted to the results from beam tests of prototypes. In addition, the read-out electronics performances, such as noise, cross-talk effects and dead channels, as well as the L0 trigger hardware have been considered.
The Boole output has the same format as the real data coming from the detector during the data taking.

5.3.3 Event reconstruction

The reconstruction of the event is performed by the C++ program Brunel that covers two aspects:

1. the track reconstruction;
2. the particle identification (PID);

In the track reconstruction phase, the registered hits of the VELO, the TT and T1-T3 detectors are combined to form particle trajectories from the VELO to the calorimeters. The program aims to find all tracks in the event which leave sufficient detector hits. After fitting the reconstructed trajectory a track is represented by state vectors (x, y, dx/dz, dy/dz, Q/p) which are specified at given z-positions in the experiment.

Depending on the generated trajectories inside the spectrometer the following classes of tracks are defined, illustrated in Fig. 5.6:

1. **Long tracks:** traverse the full tracking set-up from the VELO to the T1-T3 stations. They are the most important set of tracks for B-decay reconstruction.
2. **Upstream tracks:** traverse only the VELO and TT stations. They are in general lower momentum tracks that do not traverse the magnet. However, they pass through the RICH 1 detector and may generate Cherenkov photons. They are therefore used to understand backgrounds in the particle-identification algorithm of the RICH.
3. **Downstream tracks:** traverse only the TT and T1-T3 stations. The most relevant cases are the decay products of K^0_S and Λ that decay outside the VELO acceptance.
4. **VELO tracks:** are measured only in the VELO and are typically large angle or backward tracks, useful for the primary vertex reconstruction.
5. **T tracks:** are only measured in the T1-T3 stations. They are typically produced in secondary interactions, but are useful for the global pattern recognition in RICH 2.

The particle identification is provided by the two RICH detectors, the Calorimeter system and the Muon Detector. For the common charged particle types $(\mathrm{e}, \mu, \pi, \mathrm{K}, \mathrm{p})$, electrons are primarily identified using the electromagnetic calorimeter, muons with the muon detector, and the hadrons with the hadronic calorimeter and the RICH system, which provides a good

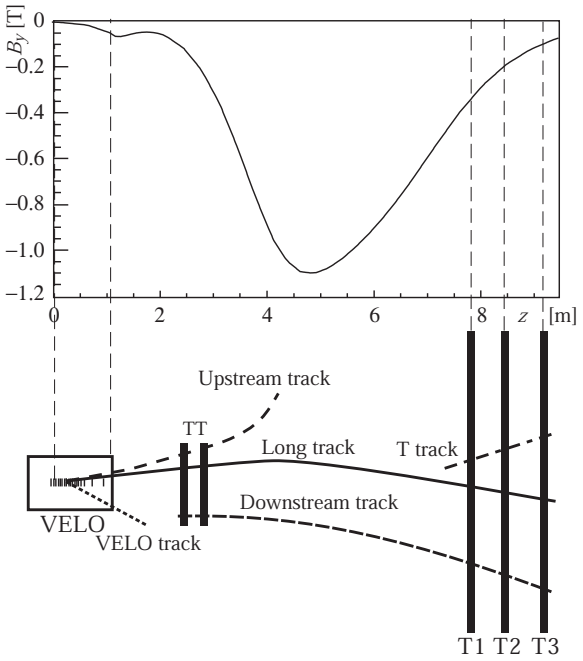

Figure 5.6: A schematic illustration of the various track types: long, upstream, downstream, VELO and T tracks. For reference the main B-field component (B_y) is plotted above as a function of the z coordinate.

separation between π, K ,p. However, the RICH detectors can also improve the lepton identification, so the informations from the various detectors are combined.
In general for decay muons, the most relevant source of misidentification is represented by the charged pions that succeed in traversing the muon filter, commonly called *punch-through*. To reject this background, a muon identification is performed cutting on the ratio of the likelihoods between the muon and pion hypotheses:

$$\begin{aligned} \Delta \ln \mathcal{L}_{\mu\pi} &= \ln \mathcal{L}(\mu) - \ln \mathcal{L}(\pi) \\ &= \ln \left[\mathcal{L}(\mu) / \mathcal{L}(\pi) \right] \end{aligned}$$

where the likelihoods from the various sub-detector are simply combined as follows:

$$\mathcal{L}(\mu) = \mathcal{L}^{\mathrm{RICH}}(\mu)\, \mathcal{L}^{\mathrm{CALO}}(\mathrm{non\,e})\, \mathcal{L}^{\mathrm{MUON}}(\mu)$$

5.3.4 Event Analysis

Finally the offline analysis is performed with the C++ program DaVinci.
This is the main tool used in this study to operate the selection on the signal and background samples.
Several algorithms has been collected during the utilization of such a program, and the LHCb collaboration encourages the use of the official algorithms, in order to avoid the proliferation of many algorithms performing the same task. In addition, common algorithms used by many people make easier the discovery of code bugs, as well as the communication and the comparison of the results inside the collaboration.
In my analysis, three of such common algorithms have been used:

- *StandardLooseMuons*. This and a group of similar algorithms are devoted to the selections of a subset of the reconstructed particles, according to several PID cuts common to all the collaboration. As suggested by the name, this one selects particles fulfilling the minimal requirements for the muon hypothesis, i.e. a long track and the presence of hits in the muon detector.

- *MakeResonance*. This is the main algorithm that generate composite particles, using the particles coming from the reconstruction as well as composite particle generated in a previous iteration.
  It combines the daughter particles to form several mother particle candidates, allowing, by means of other sub-algorithms, to restrict the acceptance criteria for daughters as well as mother particles.

- *PropertimeFitter*. Given a particle, with its momentum and decay vertex, and assuming another given vertex as origin of the particle, this tool iteratively recalculate such quantities in order to better fit the hypothesis of a particle of such a momentum, flying between the two given vertices. In addition to the χ^2 of the fit, the lifetime and its error, calculated from the distance of the two refitted vertices, are obtained as results.

A forth algorithm has been written starting from the code of *DecayChainNtuple*, to save the information of the selected candidates in a ROOT formatted file.
In fact, as explained in Sec. 5.4, the analysis has been split in a *preselection*, that rejects the

bulk of the events, performed with the LHCb software, and a *final selection* performed with the classic ROOT analysis package [86].

5.3.5 Trigger in offline analysis

A general overview of the Level-0 trigger (L0) and the High Level Trigger has been given in the first chapter.
In the current status of the LHCb software framework, L0 is fully implemented, while only the exclusive selections of the HLT are almost ready: they are similar, but with looser cuts, to the official LHCb offline selections.
In the offline analysis on Monte Carlo samples, the L0 decision marks but not rejects the events. This information is recored on data during the digitalization phase, since L0 is an hardware trigger. On the contrary the HLT exclusive selections are reproduced by equivalent algorithms in DaVinci, since they will be implemented during the experiment in a computer farm.

5.4 Analysis procedure and results

As mentioned in Sec. 5.3.1, a signal sample of 62k events and a background sample of more than 13.5M of *dimuonic inclusive b* events has been taken into account.
The analysis is divided in two steps: the first *preselection* is performed with DaVinci. The output is a *N-tuple* of the information of the accepted candidates, recorded in a ROOT [86] formatted file.
The effective analysis has been performed with the ROOT analysis package: in fact the interactive sessions of such a program allows a simpler and faster tuning of the selection cuts. On the contrary DaVinci is not an interactive program, and too many program runs would be required for a fine tuning of the cuts. The disadvantage of this approach is that there isn't the full event information in the *N-tuple*, so a particular care has been devoted to save the right candidates information required for the second analysis step.

Very loose cuts has been used for the preselection step. They are directly applied by the *MakeResonance* algorithm (Sec. 5.3.4):

1. *D^0 mass window < 200 MeV*. The invariant mass of the reconstructed D^0 must not differ more than 200 MeV from the mass of such a meson, that is 1864.84 MeV;

2. *D^0 vertex χ^2 < 10*. The D^0 decay vertex is reconstructed with a fit of the daughter tracks, and the normalized χ^2 of the fit must not exceed 10.

The results of the preselection can be found in the following table, where the accepted events has at least one candidate:

Monte Carlo sample	total events	ϵ_{presel}	accepted candidates
$D^0 \to \mu^+\mu^-$ (muons in 400 mrad)	62157	45.6%	28346
inclusive b (>2 muons in 400 mrad)	13516015	7.96%	1076177

Table 5.4: Efficiency and rejection factor of the preselection.

5.4.1 Selection cuts

This section reports the cuts in the order in which they have been applied for the selection. Such quantities are correlated, so the shape of the last distributions has been already *refined* by the cuts on first ones.
Signal and *dimuonic* inclusive b are shown in the same figure to compare the shape, but obviously they are not in the same scale.

After further reducing the mass window to $\pm$ 100 MeV, cuts have been applied on daughters by requiring:

1. *muons* p_T > *500 MeV.*
2. $\Delta \ln \mathcal{L}_{\mu\pi}$ > -5.

The distributions and the effects of the cuts can be seen in Fig. 5.7 and Fig. 5.8 respectively.

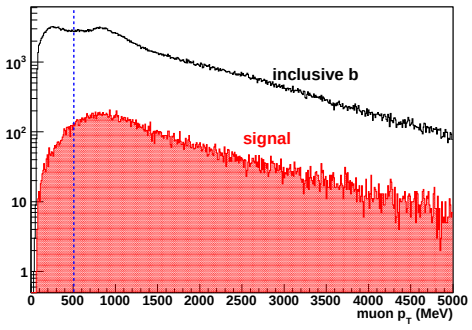

Figure 5.7: Muons transverse momentum distribution for signal and background. Only candidates whose both muons have p_T > 500 MeV are accepted.

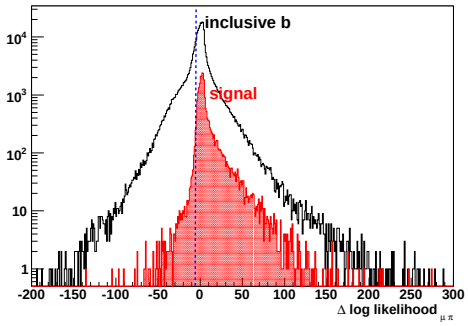

Figure 5.8: Muons logarithmic likelihoods: distribution of the difference between the muon and pion hypothesis. Only candidates whose both muons have $\Delta \ln \mathcal{L}_{\mu\pi}$ > -5 are accepted.

To ensure that a D^0 comes from a PV, and to distinguish between more visible PVs, the following cuts are applied (see Fig. 5.3 in Sec. 5.2 for labeling):

3. D^0 *IP < 0.1 mm and its significance < 3* (Fig. 5.10 and Fig. 5.9).
4. θ *< 50 mrad* (Fig. 5.11).
5. χ^2 *of the ProperTimeFitter algorithm < 6* (Fig. 5.12).

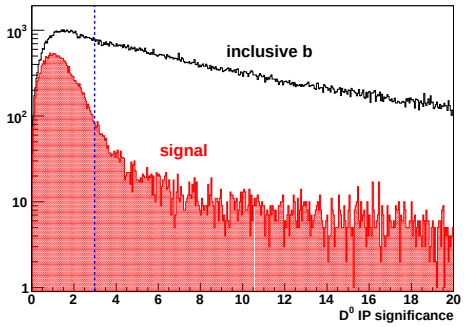

Figure 5.9: Distribution of impact parameter significance of D^0 w.r.t. the origin PV, for signal and background.

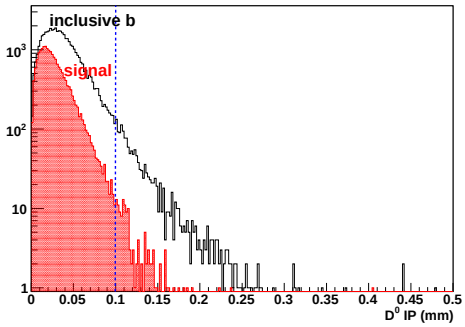

Figure 5.10: Distribution of the impact parameter of D^0 w.r.t. the origin PV, for signal and background.

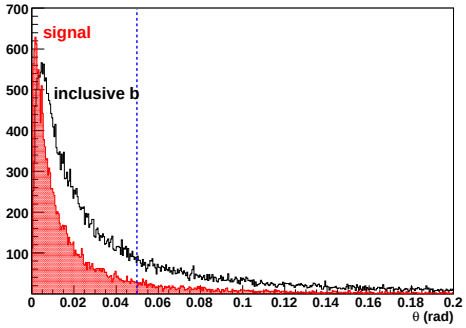

Figure 5.11: Distribution of the angle between the D^0 momentum, as sum of the daughter muons momenta, and the flight direction, built connecting the reconstructed decay vertex and the PV assumed as origin.

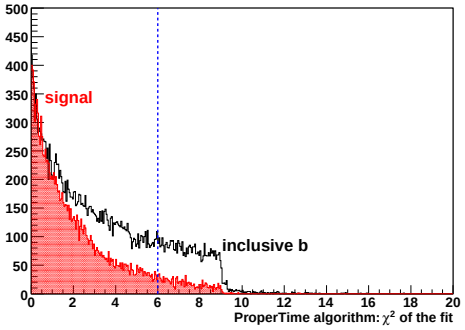

Figure 5.12: χ^2 of the ProperTimeFitter algorithm. This algorithm performs a new fit of the D^0 origin and decay vertices and momentum, estimating the general goodness of the reconstruction hypothesis.

The request of a minimum flight path has been introduced with:

6. *Muons IP significance > 1* (Fig. 5.13).

7. *Lifetime significance > 2* (Fig. 5.14).

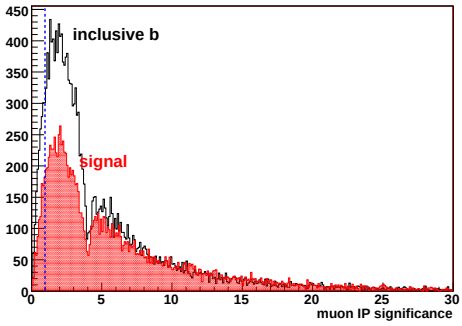

Figure 5.13: Distribution of impact parameter significance of daughter muons w.r.t. the D^0 origin PV, for signal and background.

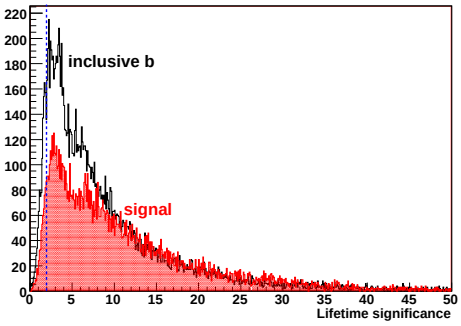

Figure 5.14: Distribution of D^0 lifetime significance as obtained from the *ProperTimeFitter* algorithm, for signal and background.

Finally, a tighter cut, with respect to the preselection one, has been applied on the D^0 vertex χ^2 (less than 5, see Fig. 5.15), obtaining the invariant mass distributions shown in Fig. 5.16.

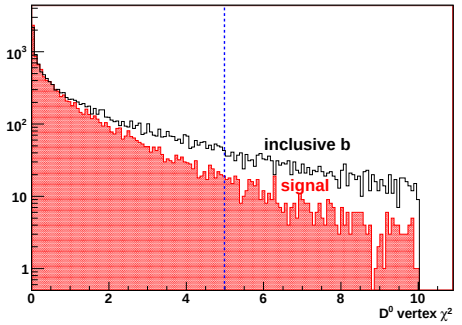

Figure 5.15: χ^2 distribution of the D^0 reconstructed decay vertex, for signal and background.

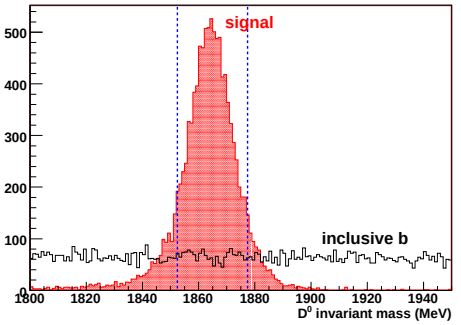

Figure 5.16: D^0 invariant mass distribution of the surviving events, for signal and background.

With a tight mass window of ± 12.5 MeV, the candidates at the end of the selection are 8776 for the signal and 1666 the *dimuonic* inclusive b background.

5.4.2 The effect of the L0 trigger

It is very likely that $D^0 \to \mu^+\mu^-$ events pass L0 trigger for the two muons present in the event. In fact, in addition to the single muon stream, where the foreseen p_T threshold is 1.1 GeV and a veto is generated by too many primary interactions (Sec. 1.3.1) or too large charged particle multiplicity in SPD (Sec. 1.3.5), the L0 trigger implements a dimuonic stream that has a foreseen threshold of the p_T sum of 1.3 GeV and ignores such a veto. The selection already implicitly introduces a cut of 1 GeV on the p_T sum, so many of the selected events trigger the dimuonic stream.
In Fig. 5.17 and Fig. 5.18 the effect of the L0 trigger is shown as a function of the candidates muon, respectively for the signal and background events that survives selection.

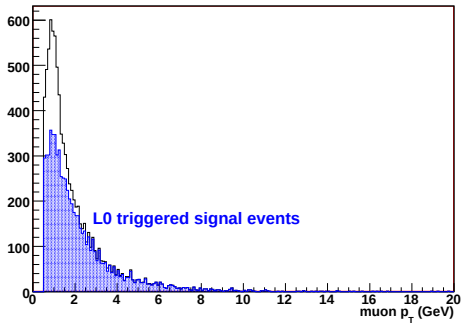

Figure 5.17: Muon p_t distribution of the selected events passing also L0 trigger (blue histogram) compared with distribution of selected events, for the signal.

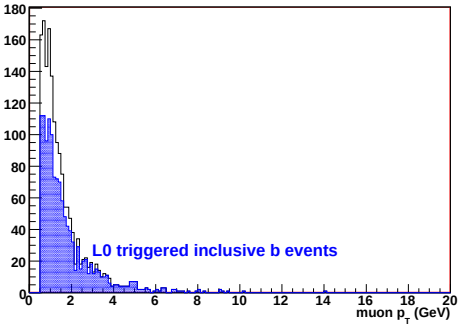

Figure 5.18: Muon p_t distribution of the selected events passing also L0 trigger (blue histogram) compared with distribution of selected events, for the *dimuonic* inclusive b background.

Almost the same fraction of events pass the trigger: 6703 (76.4%) signal events and 1250 (75.9%).

As mentioned in Sec. 5.3.5, the High Level Trigger software is still under way, and the ready or planned selections can be not suitable for this channel. Instead a exclusive selection for this channel can be written as a result of this work, for example using the preselection with slightly tighter cuts. Depending on the available bandwidth and the experiment priorities, such an algorithm can become part of the High Level Trigger.

5.4.3 Selection summary and results

The following table summarizes the steps of the selection and the relative efficiency for signal and background.

	$D^0 \to \mu^+\mu^-$ $\sigma_{\rm gen}$ = 634.3 $\mu b \times BR$		***dimuonic* inclusive b** $\sigma_{\rm gen}$ = 6.5 μb	
events in sample		62157		13516015
preselection	45.6%	28346	7.96%	1076177
$M_{D^0} \pm 100$ MeV, $\mu\ p_T$ > 500 MeV, $\Delta \ln \mathcal{L}_{\mu\pi}$ > -5	77.1%	21862	16.0%	171773
IPS$_{D^0}$ < 3, IP$_{D^0}$ < 0.1 mm, θ < 50 mrad, $\chi^2_{\tau\text{fit}}$ < 6	63.0%	13767	11.3%	19443
IPS$_\mu$ > 1, τ *significance* > 2	83.0%	11425	74.5%	14477
$\chi^2_{D^0 vtx}$ < 5, $M_{D^0} \pm 12.5$ MeV	76.8%	8776	11.5%	1666
preselection & selection	14.1%	8776	1.23×10^{-4}	1666
L0 trigger	76.4%	6703	75.9%	1260
preselection & selection & L0 trigger	10.8%	6703	9.32×10^{-5}	1260

Table 5.5: Efficiencies of the various steps of the selection, as well as L0 trigger efficiencies, for signal and background.

The expected integrated luminosity at LHCb during one year (10^7 s) is 2 fb^{-1}. The expected annual event yield for the signal and this kind of background can be calculate starting from the effective *generation* cross sections:

$$N = \sigma_{\rm gen} \times \mathcal{L}_{int} \times \epsilon_{\rm presel} \times \epsilon_{\rm sel} \times \epsilon_{\rm trig}$$

For the efficiencies in Tab. 5.5, after an integrated luminosity of 2 fb^{-1}, the following annual yield are expected for signal and *dimuonic* inclusive b background:

$$N_{D^0\to\mu^+\mu^-} \simeq 1.37 \times 10^{11} \times BR \quad ; \qquad N_{\rm incl.b,2\mu} \simeq 1.21 \times 10^6$$

Such numbers means that no events are expected in the Stardard Model (BR $\sim 10^{-13}$), and, with the exception of the MSSM with $\mathcal{R}$-Parity violation, also in the other scenarios presented in Sec. 5.1 the few events that can occur are not discernible from the background (Tab. 5.6).

In fact, a number of signal events at least five times the fluctuation of the expected background yield is usually required for the observation of the signal.
The fluctuation of the background yield can be estimated with a simple Poisson distribution assumption: in this approach, the standard deviation is the square root of the expected value, i.e. $\sim$ 1100 events, and the number of events required for signal are at least 5500.

Theoretical model	Expected $\mathcal{BR}$	Events at 2 fb^{-1}
Standard Model	3×10^{-13}	0
MSSM , $\mathcal{R}$-Parity violation	3.5×10^{-6}	5×10^{5}
Multiple Highs Doublets	8×10^{-10}	110
Horizontal Gauge Models	3×10^{-11}	4
Extra fermions	3×10^{-11}	4

Table 5.6: Expected annual yield in the scenarios presented in Sec. 5.1.

The absence of signal can as well lead to the definition of an *upper limit* for the BR, usually as the branching ratio generating a number of signal events smaller than three times the background fluctuation, i.e. with the previous numbers:

$$N_{D^0\to\mu^+\mu^-} < 3 \times \sqrt{N_{\text{incl.b},2\mu}}$$
$$1.37 \times 10^{11} \times BR < 3300$$
$$BR < 2.4 \times 10^{-8}$$

Such a limit is about two order of magnitude better than the current one (1.3×10^{-6}, [81]), and its measurement can introduce constraints in the above mentioned models.
With an higher integrated luminosity, obtained during the years of LHCb operation, the limit improve as a function of the square root of the integrated luminosity. In Tab. 5.7, the same calculations are performed also after five and ten years of LHCb operation.

	2 fb^{-1} (1 LHCb year)	10 fb^{-1} (5 LHCb years)	20 fb^{-1} (10 LHCb years)
$N_{\mathrm{incl.b},2\mu}$	1.21×10^{6}	6.06×10^{6}	12.1×10^{6}
$\sqrt{N_{\mathrm{incl.b},2\mu}}$	1100	2461	3481
$N_{D^0\to\mu^+\mu^-}$	$1.37\times10^{11}\times$ BR	$6.85\times10^{11}\times$ BR	$13.7\times10^{11}\times$ BR
BR upper limit	2.4×10^{-8}	1.1×10^{-8}	7.6×10^{-9}

Table 5.7: Upper limit on branching ratio after one, five and ten years of LHCb operation.

5.5 Final considerations

This study demonstrates that LHCb can improve, in one year of operation, the current upper limit on the branching ratio of the rare $D^0 \to \mu^+\mu^-$ decay up to two order of magnitude, thanks to its high charm production and very high rapidity coverage.
The main limitation is the estimation of the background rejection with the *dimuonic inclusive b* Monte Carlo sample, instead of a similar charmed sample, more suitable for its larger cross section and similar kinematics but not available.
It must be stressed that the two muons in that kind of sample don't necessarily come from the B hadrons, but just the presence of them somewhere in the event is required. For this reason, with a good level of approximation, only a constant factor, to take into account for the higher charm production, should enter in the calculation of the annual yield of the *dimuonic inclusive c* events passing the selection.
A rough estimation can be obtained from the the ratio of the *generic inclusive b* and *c* production, i.e. without the requirement of two muons present in LHCb acceptance, that is about 32 according the corresponding Monte Carlo samples. The corresponding upper limit becomes about six times worse, as the number enters with the square root in the calculation, but an improvement of one order of magnitude with respect to the current limit is still obtained after one year of LHCb operation.
With the beginning of the experiment so near, the background effects will be clarified directly with the real data.

On the other hand there is space for an improvement of the analysis. An interesting approach can be the selection of D^0 coming from the charged $D^*(2010)$, as it largely decays in $D^0\pi^\pm$ ($\sim$ 67.7% [82]).

The D^* – D^0 mass difference is a strong constraint for the reduction of the combinatorial background. Moreover, as D^* is a short resonance and do not fly before the decay, this approach takes into account for the D^0 coming from the primary vertex as well as the ones coming from (typically B hadron) chain of decays, that are discarded in the previous approach. Practically, the same selection can be exploited providing to substitute the primary vertex with the D^* vertex.

Conclusions

This thesis reports the work performed on two aspects of the LHCb experiments: the development of a Gas Electron Multiplier (GEM) detector for the high irradiated region of the muon system, and the study of a selection for the rare $D^0 \rightarrow \mu^+\mu^-$ decay at the LHCb experiment.

The triple-GEM detectors will equip the innermost and forward region (M1R1, $\sim$ 1 m^2 area) of the Muon system, where the harsh environment around the beam pipe does not allow the use of the Multi Wire Proportional Chambers, and will contribute to the muon p_T measurement for the LHCb Level-0 trigger.
The requirements for detectors in M1R1 are:

- a particle rate capability up to $\sim$ 500 kHz/cm^2;
- each station, made up of two independent detectors logically OR-ed pad by pad, must have an efficiency in the bunch crossing time window higher than 96%;
- a pad cluster size, i.e. the number of adjacent detectors pads fired when a track crosses the detector, should not be larger than 1.2 for 10×25 cm^2 pad size;
- the detector must tolerate, without damages or large performance losses, the charge integrated in 10 years of operation at an average particle flux of 184 kHz/cm^2 for an average machine luminosity of 2×10^{32} cm^{-2}s^{-1}.

An intense R&D activity, performed with a triple-GEM prototype of 10×10 cm^2 active area, was required to optimize the GEM detectors especially in terms of the time performance.
Very interesting and unique results have been obtained with this kind of detector, so far typically used only for tracking purpose: time resolutions better than 5 ns (for the single detector) are achieved with fast and high yield CF_4 and iso-C_4H_{10} based gas mixtures, considerably

improving the results obtained in the past with the standard Ar/CO_2 (70/30) gas mixture ($\sim$ 10 ns). With such fast gas mixtures, an efficiency above the 96% in a 20 ns time window is achieved by a detector composed by two logically OR-ed Triple-GEM chambers, as required in the experiment.
The design of the detector, that must take into account the tight space constraints around the beam, has been finalized, and detailed construction procedures as well as severe quality controls have been defined for the production of 12 fully instrumented detectors and 6 additional spare detectors.
Severe tests have been performed on the final detector:

- the compatibility of the construction materials with the gas mixture has been qualified in a global irradiation test at the ENEA-Casaccia with ^{60}Co source, demonstrating that the detector can tolerate the radiation dose foreseen in 10 years of operation in the region M1R1 of the LHCb experiment.
- a final test of the detector, fully integrated with the front-end electronics and all the other service components, has been recently done at the SPS beam at CERN, where the LHCb running condition has been simulated by means of a similar bunch crossing time structure and the adoption of the official LHCb DAQ chain. The results largely fulfilled the experiment requirements and useful information on the time alignment procedure for the commissioning phase has been obtained.

All the produced detector are now at CERN, ready for the installation on the apparatus, foreseen for the first months of 2008.

Recent works demonstrated some interest for rare decays in the charm sector, that can gives complementary information with respect to the K or B–mesons physics, since the parameters of several extension of the Standard Model can be constrained as well by such processes.
In the second part of the thesis the possibility at the LHCb experiment of the search of the rare $D^0 \to \mu^+\mu^-$ decay has been investigated.
In fact the LHCb experiment can take advantage from the very high rapidity coverage of the apparatus and the low p_T threshold setting; they are optimized for the *beauty* physics, but the *charm* cross section ($\sim$ 3.5 mb) is about seven times higher with respect to the *beauty* cross section (0.5 mb).
Using the simulation and the analysis software framework realized for the experiment, a se-

lection algorithm has been written.

The efficiency and the background rejection power of such an algorithm has been estimated using official LHCb Monte Carlo samples. Since the most dangerous background comes from the combinatorial of muons present in the events, being the muon-pion misidentification at LHCb very low ($\sim$ 1%), a sample composed by *inclusive b* events with at least two muons (not necessarily coming from *b* hadrons) has been taken into account.

A first estimation of the upper limit on the branching ratio measurable at LHCb is of the order of 10^{-8}, about two order of magnitude lower than the current one.

Bibliography

[1] LHCb collaboration, ”LHCb Technical Proposal”, CERN/LHCC 04 (1998).

[2] The LHC Study Group., ”The Large Hadron Collider, Conceptual Design”, CERN/AC/95-05 (LHC).

[3] P. Nason *et al.*, Bottom production. In Proceedings of the 1999 Workshop on Standard Model Physics at the LHC, volume CERN 2000-04. CERN, 1999, hep-ph/0003142.

[4] LHCb collaboration, ”LHCb Reoptimized Detector Design Report”, CERN/LHCC 030 (2003).

[5] LHCb collaboration, ”LHCb VELO Technical Design Report”, CERN/LHCC 011 (2001).

[6] LHCb collaboration, ”LHCb RICH Technical Design Report”, CERN/LHCC 037 (2000).

[7] LHCb collaboration, ”LHCb Magnet Technical Design Report”, CERN/LHCC 007 (2000).

[8] LHCb collaboration, ”LHCb Inner Tracker Technical Design Report”, CERN/LHCC 029 (2002).

[9] LHCb collaboration, ”LHCb Outer Tracker Technical Design Report”, CERN/LHCC 026 (2001).

[10] LHCb collaboration, ”LHCb Calorimiters Technical Design Report”, CERN/LHCC 036 (2000).

[11] LHCb collaboration, ”LHCb Muon System Technical Design Report”, CERN/LHCC 010 (2001).

[12] LHCb collaboration, ”LHCb Trigger System Technical Design Report”, CERN/LHCC 010 (2003).

[13] A. Barczyk *et al.*, ”1 MHz Readout”, LHCb note 062 (2005).

[14] J. A. Hernando Morata, ”The LHCb Trigger”, Acta Physica Polonica B, volume B38, 2007, 941-945.

[15] M. Battaglia *et al.*, ”The CKM matrix and the Unitary Triangle”, hep-hp/0304132.

[16] C. H. Cheng *for the BABAR and BELLE collaborations*, hep-ex/0707.1192.

[17] UTFIT Home page, www.utfit.org.

[18] ATLAS muon collaboration, “ATLAS muon spectrometer, Technical Design Report”, CERN/LHCC 97–22.

[19] CMS muon collaboration, ”CMS The muon project, Technical Design Report”, CERN/LHCC 97–32.

[20] CDF Note 8957 (August 2007).

[21] A. Ali, Nucl. Instr. and Meth. **A 384** (1996) 8.

[22] N. Harnew, ”B Physics at the LHC”, Frascati Physics Series Vol. XXXI 289 (2003).

[23] C. Zeitnitz and T.A. Gabriel, The Geant-Calor interface User’s Guide (1999), `http://www.physik.uni-mainz.de/zeitnitz/gcalor/gcalor.html`

[24] I. Azhgirey, I. Kurochkin and V. Talanov, “Development of MARS Code Package for Radiation Problems Solution of Electro-Nuclear Installation Design”, in: Proc. of XV Conference on Charged Particles Accelerators, Protvino, October 22–24 (1996)

[25] N. Saguidova *et al.*, “GCALOR Studies of Backgrond in the LHCb Muon chambers”, LHCb 1998-059 Expt;
A. Tsaregorodtsev, “Muon System parameterised background – algorithm and implementation”, LHCb 2000–011 Muon.

[26] P. Colrain, “Upgrade of the Muon System background parameterisation”, LHCb 2001–029 Muon.

[27] LHCb collaboration, ”Addendum to the LHCb Muon System Techical Design Report”, CERN/LHCC 002 (2003).

[28] LHCb collaboration, ”Second Addendum to Muon System Technical Design Report”, CERN/LHCC 012 (2005).

[29] M. Anelli *et al.*, ”Test of MWPC prototypes for Region 3 of Station 3 of the LHCb Muon System”, LHCb 2004-74 Muon.

[30] M. Anelli *et al.*, ”Aging test of a prototype for the region 3 of the LHCb muon system”, LHCb 2003–040 Muon.

[31] J. Christiansen, ”Requirements for the L0 front-end electronics”, LHCb 1999-029 Trigger.

[32] W. Bonivento *et al.*, Nucl. Instr. and Meth. **A 491** (2002) 233.
The main characteristic of the CARIOCA chip can be found in: http://www.cern.ch/riegler/.

[33] G. Charpak *et al.*, Nucl. Instr. and Meth. **A 62** (1968) 262.

[34] F. Sauli, ”Principle of operation of multiwire proportional and drift chamber”, Yellow Report, CERN 77-09, 1977.

[35] A. Oed *et al.*, Nucl. Instr. and Meth. **A 263** (1988) 351.

[36] F. Angelini *et al.*, Nucl. Instr. and Meth. **A 283** (1989) 755.

[37] F. Angelini *et al.*, Nucl. Instr. and Meth. **A 382** (1996) 461.

[38] R. Bouclier *et al.*, Nucl. Instr. and Meth. **A 369** (1996) 328.

[39] R. Bouclier *et al.*, Nucl. Instr. and Meth. **A 381** (1996) 289.

[40] R. Bellazzini *et al.*, Nucl. Instr. and Meth. **A 457** (2001) 22.

[41] F. Angelini *et al.*, Nucl. Instr. and Meth. **A 335** (1993) 69.

[42] S. Biagi et al., Nucl. Instr. and Meth. **A 361** (1995) 72.

[43] F. Bartol *et al.*, J. Phys. III France 6 (1996) 337.

[44] I. Giomataris *et al.*, Nucl. Instr. and Meth. **A 376** (1996) 29.

[45] R. Bellazzini *et al.*, Nucl. Instr. and Meth. **A 424** (1999) 444.

[46] R. Bellazzini *et al.*, Nucl. Instr. and Meth. **A 423** (1999) 125.

[47] F. Sauli, Nucl. Instr. and Meth. **A 386** (1987) 531.

[48] B. Ketzer et al. “Triple GEM tracking detectors for COMPASS”. IEEE Trans. Nucl. Sc. **49** (2002) 2403

[49] TOTEM Collaboration, Technical Proposal, CERN/LHCC/99-7.

[50] A. Breessan *et al.*, Nucl. Instr. and Meth. **A 425** (1999) 262.

[51] J. Benlloch *et al.*, Nucl. Instr. and Meth. **A 419** (1998) 410.

[52] A. Gandi,*Laboratory of Photomechanical Technique and Printed Circuites*, EST-SM-CI Section, CERN, Geneva, Switzerland.

[53] M. Inuzuka *et al.*, Nucl. Instr. and Meth. **A 525** (2004) 529.

[54] J. Benlloch *et al.*, *"Development of the Gas Electron Multiplier (GEM)”*, CERN-PPE/97-146.

[55] S. Bachmann *et al.*, Nucl. Instr. and Meth. **A 438** (1999) 376.

[56] Maxwell 3D Field Smulator. User’s refence. Ansoft Corporation.

[57] R. Veenhof, Nucl. Instr. and Meth. **A 419** (1998) 726.

[58] C. Richter *et al.*, Nucl. Instrum.Meth. **A 461** (2001) 38.

[59] J. Townsend, *”Electron in gases”*, Hutchinson, Londra 1947.

[60] G. Bencivenni *et al.*, Nucl. Instrum.Meth. **A 488** (2002) 493.

[61] M. Poli Lener Degree Thesis, ”Studio e sviluppo di un rivelatore a GEM per la zona centrale delle camere a muoni di LHCb”, (2002).
www.lnf.infn.it/esperimenti/thes/tesipoli.pdf

[62] G. Bencivenni *et al.*, Nucl.Instrum.Meth. **A 494** (2002) 156.

[63] D. Pinci PhD. Thesis, ”A triple-GEM detector for the muon system of the LHCb experiment”, (2002).

[64] R.J. Yarema *et al.*, IEEE Trans. Nucl. Sci. **NS-39** (1992) 742.

[65] S. Ramo, "Currents induced in electron motion", Proc. IRE 27 (1934) 584.

[66] G. F. Knoll, "Radiation detection and measuremt", John Wiley and Sons (1989).

[67] M. Alfonsi *et al.*, Nucl.Instrum.Meth. **A 518** (2004) 106.

[68] S. Backmann *et al.*, Nucl.Instrum.Meth. **A 479** (2002) 294.

[69] H. Raether, "Electron Avalanches and Breakdown in Gases", Butterworth, London (1964).

[70] F.E. Taylor, Nucl. Instrum. Meth. **A289** (1989) 283.

[71] F. Sauli, Nucl. Instrum. Meth. **A 515** (2003) 249.

[72] M. Hohlmann *et al.*, Nucl. Instrum. Meth. **A 494** (2002) 179.

[73] C. Altunbas *et al.*, Nucl. Instrum. Meth. **A 490** (2002) 177.

[74] E. Amaldi, R. Bizzari, G. Pizzella, "Fisica Generale", Zanichelli editore (1995).

[75] R.O. Ritchie, "Mechanical Behavior of Materilas Lecture Notes ", University of California, Berkeley, Fall 1993.

[76] W. Bonivento *et al.*, "Design and performance of the front-end electronics of the LHCb muon detector.", published in "Heidelberg 2005, Electronics for LHC and future experiments", 66.

[77] G. Corradi *et al.*, Nucl. Instrum. Meth. **A 572** (2007) 96.

[78] A. Alfonsi *et al.*, presented at Puerto Rico 2005 IEEE conference (Oct. 23-29) and submitted to Transaction on Nuclear Science.

[79] G. Burdman *et al.*, Phys.Rev. D66 (2002) 014009.

[80] G. Buchalla *et al.*, Rev. Mod. Phys. 68 (1996) 1125.

[81] BABAR Collaboration, Phys. Rev. Lett. 93 (2004) 191801

[82] Particle Data Group, Review of Particle Physics 2006

[83] G.Barrand *et al.*, "Gaudi - a software architecture and framework for building HEP data processing applications", Comp. Phys. Comm. 140 (2001).

[84] T. Sjostrand *et al.*, "High Energy physics event generation with Pythia", Comp. Phys. Comm., 135 (2001) 238.

[85] S. Agostinelli *et al.*, Nucl. Inst. Meth. **A 506** (2003) 250.

[86] R. Brun and F. Rademakers, "ROOT - An Object Oriented Data Analysis Framework", Proceedings AIHENP'96 Workshop, Lausanne, Sep. 1996, Nucl. Inst. Meth. **A 389** (1997) 81-86.

Ringraziamenti

Devo innanzitutto ringraziare il Dott. Giovanni Bencivenni, il mio relatore. Non solo perché si è accollato di nuovo la correzione della mia tesi (e stavolta devo ammettere che è stato veramente pesante), ma anche perché ha creduto in me e mi ha sempre sostenuto durante questi anni.
Di conseguenza devo ringraziare anche il Dott. Fabrizio Murtas, anche per le (spesso concitate) discussioni sui temi di attualità al di fuori della fisica!
Lo ribadisco come sulla tesi di laurea: non c'è dubbio che tutto quello che ho imparato in questi anni ai Laboratori Nazionali di Frascati lo devo soprattutto a loro due.
Terzo (ma giusto perché se non li metto prima i capi poi chi li sente..) ci sta Marco 1, seguendo la nomenclatura del gruppo (più originale rispetto al classico Dott. Marco Poli Lener). Gli devo molto per l'aiuto durante la scrittura della tesi.
Lavorare con persone in gamba come lui e Marco 2 (sempre seguendo la nomenclatura del gruppo) è stato veramente gratificante e per molti aspetti divertente.
A questo punto voglio ringraziare il "gruppetto pausetta": Silvia, Flavia, Chiara, Danilo, Alessio, Marco 1, Marco 2 (quando riusciva a fuggire dalla camera pulita.. povero!), Fabrizio, Gianni, Patrizia (si vero, alcuni sono gli stessi di prima, ma stavolta è un altro ambito no?).. e chi ce l'avrebbe fatta senza il caffettino o il tèino delle 5? Nonché tutte le memorabili uscite organizzate dal gruppo (una volta bollato il metodo dell'istogrammone per passare al più pratico "chi c'è c'è" l'attività è andata a regime).
Vorrei anche ringraziare tutte le persone con cui sono entrato in contatto durante questi anni: i "gemmisti" di Cagliari, quali Davide, Edoardo, Alessandro e Walter; Alessio "asarti", Barbara e gli altri coinvolti nelle attività di divulgazione per i bimbi; tutti "quelli delle camere a fili".
In particolare vorrei ringraziare Davide Pinci per avermi coinvolto in quest'impresa (sicuramente impresa per degli hardwaristi!) del $D^0 \to \mu^+\mu^-$. È stata una grande opportunità per

imparare qualcosa di nuovo e di diverso dal lavoro svolto finora, e di grande utilità visto che, con l'acceleratore in partenza, sarà necessario preoccupparsi di analizzare i dati.

Arrivo finalmente a ringraziare la mia famiglia, senza il loro contributo e incoraggiamento non ce l'avrei fatta. Spero di poter ripagare tutti i sacrifici che hanno fatto finora per me (credo che una cena non basterà!).
Ringrazio infine i miei amici che non si sono dimenticati di me neanche negli ultimi mesi di scrittura tesi, in cui ho staccato tutti i contatti con il mondo, e anzi mi hanno tirato fuori dal mio buco per una partita a SPQRisiko!
Concludo ringraziando coloro i quali mi fossi dimenticato di ringraziare (per avere la coscienza a posto): perdonatemi in tal caso, non è ingratitutide, è arteriosclerosi precoce galoppante!